BAYESIAN DATA ANALYSIS FOR LISA PATHFINDER

NIKOLAOS KARNESIS

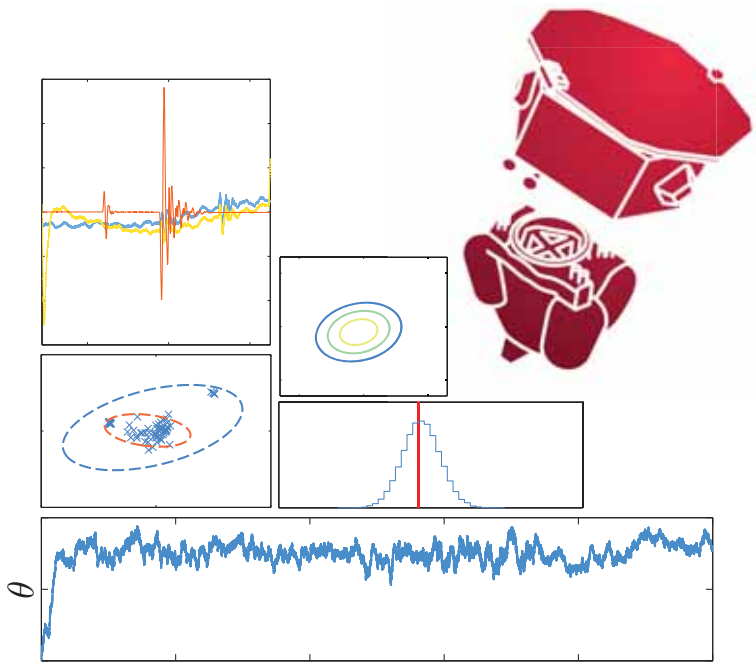

Techniques applied to system identification experiments

Departament de Física
Universitat Autònoma de Barcelona

Advisors: Dr. Miquel Nofrarias Serra & Dr. Carlos Fernández Sopuerta

October, 2014

IEEC CSIC UAB

4 PARAMETER ESTIMATION ON THE SENSITIVE AXIS

Up to this point, we have made an introduction the the LPF mission, and its ultimate goal, which is no other than to pave the way for GW detection in space. Also, we have overviewed the main statistical tools that we will use to perform parameter estimation for the planned system identification experiments of the LTP. In this chapter, we will first go through a more detailed description of the dynamics of the LTP and the modelling of the system over the sensitive axis. While in this chapter we will approximate the dynamics of the LTP from the more simplified one-dimensional point of view, the modelling of the system can be extended to all DOF. Inside the LTPDA framework, the system is modelled via three main approaches; via the SSM format, the analytical x-domain, and finally in the analytical again, acceleration domain.

We will also overview the experiments design together with their goals, the estimation of the parameters crucial for the characterisation of the LPF dynamics. The strategy of these investigations, is basically to "excite" the system, by applying sinusoidal commanding displacements, forces and torques and then examining the motion of the TMs and SC. The experiments are categorised into two major groups. The first one aims to characterise the dynamics over the sensitive axis of the experiment, which is an essential part of the mission. The second is designed to excite the system into different DOF and investigate various cross-talk terms that may pollute the sensitive interferometer read-out, and it will be described in the following chapter 5.

Finally, we will go through the modelling of the PSD of the noise, and how these parameters can be handled in the bayesian framework. A comparison of different techniques and approaches, is going to be presented.

4.1 THE SYSTEM IDENTIFICATION EXPERIMENTS DESIGN

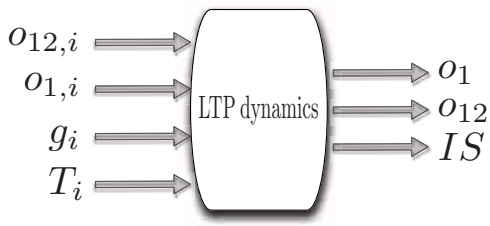

Figure 4.1: The input-output scheme for measuring the LTP parameters. There can be applied "fake" interferometer readings $o_{1,i}$ and $o_{12,i}$ that will generate a response of the system, direct forces g_i and torques T_i, where $i = TM1, TM2, SC$.

Contrary to the detection schemes, the system identification of the LPF is based on the fact that the injection signals are known. These known input signals will induce a large in amplitude response of the system, that will be used to calibrate the close-loops

transfer functions. This scheme, allows to design injections that would generate a zero output to a perfect system. "Perfect" means that there are no mechanical, alignment or any other kind of imperfections while assuming that all system parameters are known. But since this cannot be true for any given system, the last type of injections will reveal any possible "disfigurement", and furthermore, will allow us to quantitatively assess it. Here, we will go through the design of the experiments on the sensitive axis, following [1].

In general, the sinusoidal injection signals have the form of

$$i(t) = \sum_{k=1}^{N_{freqs}} A_k \sin\left[2\pi f_k (t - T_k)\right] \left[H(t - T_k) - H\left(t - T_k + \frac{n_k}{f_k}\right)\right], \tag{4.1}$$

where N_{freq} the number of injection frequencies f_k, with the corresponding amplitude A_k and period T_k, and $H(t)$ the Heaviside step function, and $T_{k+1} = T_k + \frac{n_k}{f_k} + \Delta T$. We define $T_1 = 0$ and ΔT a delay between adjoining sinusoids. Also, the number of cycles n_k must be an integer to avoid signal truncation. The different LTP modules allow to inject signals in various elements of the system, as depicted in figure 4.1. The LTP during the system identification experiments operates in M3 mode (see Section 2.3), so the type of injections can be listed as

1. Fake interferometer readouts. As their name suggests, the idea is to command movement via "fake" readings injected to the controllers. Then, the controllers, respond to the hypothetical movement of the TMs or the SC and calculate a series of commands to bring the system back nominal operation. Any interferometer or IS channel can be used for this type of investigations.

2. Out-of-Loop (OOL) direct forces (through the electrodes for the TMs, or the thrusters for the case of the SC). This is a special category of signals, because they are commanded right after the controllers (DFACS). They can be used to produce identical motion on the TMs and SC, and later calibrate the controllers for possible imperfections.

The constrains on the design of the injection signals is listed over table 4.1.

Parameter	Value	Resolution
A_k (for $o_{1,i}$ and $o_{12,i}$)	$0 < A_k < 10$ μm	10^{-3} μm
A_k (for g_1 and g_2)	$0 < A_k < 5 \times 10^{-10}$ ms^{-2}	5×10^{-14} ms^{-2}
A_k (for G)	$0 < A_k < 5 \times 10^{-8}$ ms^{-2}	5×10^{-12} ms^{-2}
f_k	$10^{-4} < f_k < 1$ Hz	3 digits
N_{freq}	$1 < N_{freq} < 20$	-
ΔT	$0 < \Delta T < 10^3$ s	0.1 s
Duration $D = T_{N_{freq}} + \frac{n_k}{f_k}$	$5 \times 10^4 < D < 3 \times 10^5$ s	-

Table 4.1: Injection signals characteristics and requirements. Taken from [1].

Since the interest is shifted to the main scientific measurement, which is the sensitive differential interferometer channel, the primary outputs to take into account in

the analysis are the o_1 and o_{12}. The IS readings are also included for the sake of completeness.

The first investigation of the group of x-axis system identification experiments is to inject fake interferometer readings (see the top panel of figure 4.2) to the o_1 channel and sequentially in o_{12}, and monitor the positions of SC and TMs. For this investigation the AC bias for actuation on TM1 is set to zero, with a direct result of $\omega_1 < \omega_2$. The ω_i parameter denotes the electrostatic[1] stiffness on the TMs.

The second investigation is applying the same signals, but now setting the AC bias of TM1 to the same nominal value of TM2, so as $\omega_1 \simeq \omega_2$. This configuration of the system is often called as *matched stiffness*. While at the same operation, the third investigation is performed, where the OOL forces are applied. As shown in the bottom panel of figure 4.2, the third investigation is comprised by a set of identical[2] sinusoidal forces on TM1 and SC that produce a zero output on the first interferometer o_1. Then the same force per unit-mass is applied to both TMs and SC with the intention to produce a zero output to all channels. The last two groups of injections are designed to highlight any given imperfections of the system.

This set of experiments have a total duration of $\simeq$ 45100 s. They are expected to be run during the first days of the LPFs' scheduled operations in order to get a first estimate of the dynamical parameters. They will be repeated during the mission timeline to consolidate and improve accuracies of the parameters, and also t o identify possible changes of the system.

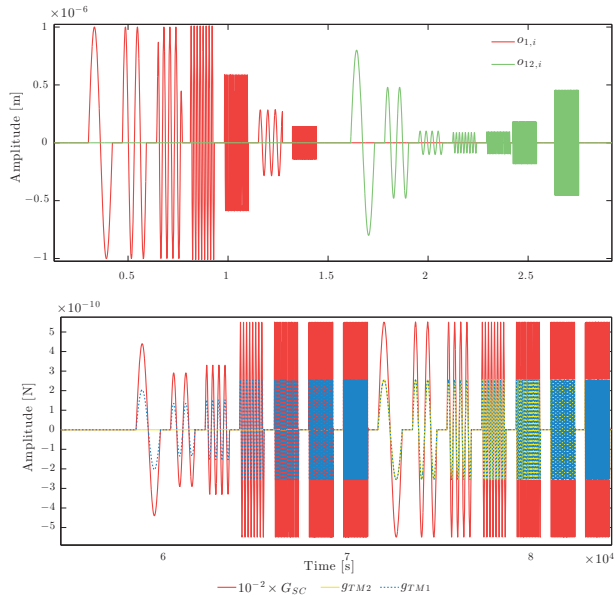

Figure 4.2: *Top:* The x-axis system ID experiments injection signals. *Bottom:* The x-axis system ID OOL forces injection signals.

1 In reality ω_i includes all the possible effects that cause the stiffnesses of the TMs.
2 Identical per unit-mass.

4.2 MODELLING THE LTP SYSTEM

The LPF must monitor constantly the position of the three main bodies of the system, the two TMs, and the SC. The position readings are performed by the two main interferometers, the IS mounted electrodes, and the attitude is controlled by the DFACS, via commands of the capacitance actuators and the trusters of the SC. The closed-loop nature of the system allows different approximations to its modelling. The LPF Data-Analysis (DA) group has developed three different almost equivalent techniques to model the LTP; the displacement domain[3] transfer function format, the SSM, and the analytical equations in the acceleration domain.

The first approach to model the system is through detailed transfer functions of the LTP sub-systems. The advantage of this method is that any information from the laboratories can be incorporated into the model. The transfer functions can be updated to the latests experiment results to calculate a realistic response of the system. But this can be a disadvantage at the same time, because a great amount of information is required just to calculate the transfer function of each submodule of the LTP. Another drawback is that the expressions can get extremely long and complicated, leaving no room for straightforward adjustments and modifications.

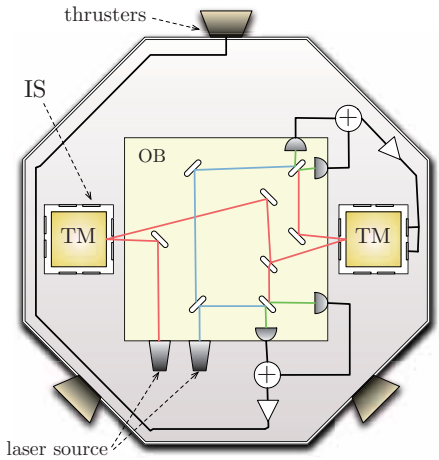

Figure 4.3: Simple 1D scheme of the LTP operating in mode M3. The position of TM1 with respect to the SC is monitored by the o_1 interferometer, and the differential position between the two TMs by the o_{12}. The second TM and the SC attitude are controlled to follow the first TM via the electrostatic actuators and thrusters respectively.

We shall take as an example the case where we inject the fake displacements in the interferometer channels. This type of injection will be henceforth called *guidance*

3 The displacement domain has an equivalent naming, the x-domain.

signals, and a depiction of such a system structure can be seen in figure 4.3. The guidance $\vec{i}$, outputs $\vec{o}$, noise $\vec{n}$, and applied forces $\vec{g}$, from eq. (3.21) are then

$$\begin{aligned} \vec{o} &= \begin{pmatrix} o_1(t) \\ o_{12}(t) \end{pmatrix}, \quad \vec{i} = \begin{pmatrix} i_1(t) \\ i_{12}(t) \end{pmatrix}, \\ \vec{n} &= \begin{pmatrix} n_1(t) \\ n_2(t) \end{pmatrix}, \quad \vec{g} = \begin{pmatrix} g_1(t) - g_{SC}(t) \\ g_2(t) - g_1(t) \end{pmatrix}. \end{aligned} \tag{4.2}$$

The closed-loop LTP system (see figure 4.4), is then described by the following set of

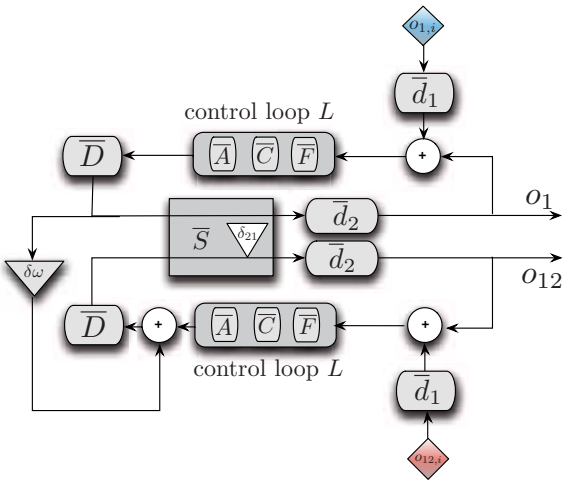

Figure 4.4: The model of the simple closed-loop system in the displacement domain of the x-axis system identification [2], for figure 4.3. See text for details.

equations [2]

$$\begin{aligned} \bar{D}\vec{q} &= \vec{g} \\ \vec{g} &= -\bar{L}(\vec{o} + \vec{i}) - \vec{g}_n \\ \vec{o} &= \bar{S}\vec{q} + \vec{o}_n, \end{aligned} \tag{4.3}$$

where here the $\bar{(\ )}$ denotes a matrix. The $\bar{D}$ is the matrix containing the dynamics, $\bar{S}$ is the sensor (or sensing) matrix (e.g. the interferometer), $\vec{q}$ are the generalised coordinates of the TMs and SC, and $\bar{L}$ is the controllers. The index n denotes noise time series of the corresponding channel. If we combine eq. (4.3), the overall transfer function of this model can be written as [3]

$$\bar{H} = \left(\bar{D} \times \left(\bar{d}_2 \times \bar{S}\right)^{-1} + \bar{L}\right)^{-1} \times \bar{L} \times \bar{d}_1, \tag{4.4}$$

The controllers box, is split in three sub-modules, the inertia decoupling matrix $\bar{C}$, the DFACS transfer functions $\bar{F}$, and a matrix expressing the actuator gains and delays $\bar{A}$. The $\bar{d}_1$ and $\bar{d}_2$ are additional delays. Since we work in a high SNR regime, we can assume

that the systems' noise does not depend on the parameter set $\vec{\theta}$, and $\vec{o} = \overline{H}(\vec{\theta}) \times \vec{i} + \vec{n}$ like in eq. (3.22). The dynamics of the system are expressed as

$$\overline{D} = \begin{pmatrix} s^2 + \omega_1^2 \left(1 + \frac{m_1}{M} + \frac{m_2}{M}\right) + \frac{m_2}{M}\delta\omega^2 & \frac{m_2}{M}(\omega_1^2 + \delta\omega^2) + \Gamma_x \\ \delta\omega^2 & s^2 + \omega_1^2 + \delta\omega^2 - 2\Gamma_x \end{pmatrix}. \tag{4.5}$$

The terms of (4.5) are the TMs $m_{TM1} \equiv m_1$, $m_{TM2} \equiv m_2$ and the SC mass $m_{SC} \equiv M$, the stiffness of TM1 ω_1^2, the differential stiffness $\delta\omega^2 \equiv \omega_2^2 - \omega_1^2$, the Γ_x the gravitational cross-coupling between the TMs, and s is the Laplace domain variable. The control loop $\overline{L}$ is written

$$\overline{L} = \overline{A} \times \overline{C} \times \overline{F}, \tag{4.6}$$

with the rest of the matrices reading as

$$\overline{A} = \begin{pmatrix} A_1 e^{-s\tau_1} & 0 \\ 0 & A_2 e^{-s\tau_2} \end{pmatrix}, \quad \overline{C} = \begin{pmatrix} -\frac{1}{M} & \frac{1}{M} \\ 0 & \frac{1}{m_2} \end{pmatrix}, \quad \overline{F} = \begin{pmatrix} H_{df} & 0 \\ 0 & H_{sus} \end{pmatrix}, \tag{4.7}$$

where A_1 and A_2 are the gains of the drag-free and suspension loop respectively, and τ_1 and τ_2 delays in the application of the commanded forces. In reality the two gains calibrate the amplitude of the applied forces by the thrusters and the electrodes. The remaining H_{df} and H_{sus} are the two known transfer functions of the two control loops. Finally, the sensing matrix is

$$\overline{S} = \begin{pmatrix} \delta_{11} & \delta_{12} \\ \delta_{21} & \delta_{22} \end{pmatrix}, \tag{4.8}$$

and it expresses the interferometer calibration constants, where the off-diagonal terms represent the possible cross-talk couplings between the two read-out channels. Nominally, we can assume that $\delta_{11} = \delta_{22} = 1$ and $\delta_{12} = 0$, while there might be a small non-zero value for the δ_{12} term, a parameter to be estimated during operations. The δ_{21}, that can be located in figure 4.4 inside the $\overline{S}$ box, can cause signal leakage from the first to the second channel as

$$\begin{aligned} o_1(t) &= x_1(t) + o_{1,n}(t), \\ o_{12}(t) &= x_{12}(t) + o_{12,n}(t) + \delta_{21} x_1(t), \end{aligned} \tag{4.9}$$

with x_1 and x_{12} the true distances and the $o_{1,n}$ and $o_{12,n}$ the readout noise. The overall response of (4.4) can calculated with the default parameter values as in figure 4.5.

The second approach to LTP modelling is the SSM. The state-space format for the LPF analysis was designed to meet certain requirements. In particular the LTP models must be [4]

1. Modular. The closed-loop nature of the LTP, together with the various operation modes and different sub-systems require a flexible model that allows smoother updates during the mission. The knowledge of the noise shapes is increasing over the duration of the operations and this should be integrated in the analysis.

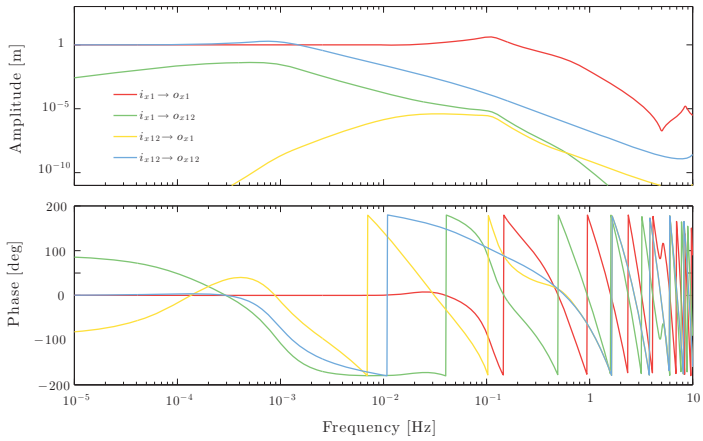

Figure 4.5: The response of the LTP analytic model. The different transfer functions of the 2×2 system are showed.

2. Scalable. A simplified one-dimensional[4] model should be a "nested" option of a more complex 3D representation of the system. This allows better maintenance and avoids code duplication.

3. Parametrised. This means that the built-in models can be used as a simulator, as well as, for parameter estimation purposes. This adds another prerequisite, where the models must be computationally cheap for fast MC simulations.

4. Documented. Each version and sub-module must be documented sufficiently for the convenience of the end-user.

5. Require a low number of manipulations. Again for the convenience of the end-user, he/she must use a high level language to assemble the different modules to build a complete LTP model. Ready-made build-in versions of LTP should be present.

After consideration of various approaches, the state-space one was chosen. The LTPDA SSMs [4, 5, 6, 7, 8] follows the standard implementation of the state-space representation for continuous time invariant models

$$\begin{aligned} \dot{\vec{x}}(t) &= A \times \vec{x}(t) + B \times \vec{u}(t), \\ \vec{y}(t) &= C \times \vec{x}(t) + D \times \vec{u}(t), \end{aligned} \tag{4.10}$$

where $\vec{x}$ are the states, $\vec{u}$ represent the input vector, and $\vec{y}$ are the outputs of the system. In turn, the A is the state matrix, B the input matrix, C the output matrix, and D the feedthrough matrix, all of them containing constant coefficients. A full 3-D SSM of the LTP considers all 15 DOFs. The state vector is composed of the spacecraft attitude and rotation rate, followed by the position, velocity, attitude and rotation rate for both TMs. The equations of motion are derived by the Euler-Lagrange and d'Alembert equations [5], and once they are written down, the variables corresponding to the spacecraft inertial motion are vanishing as they are not observable, yielding 30

4 One-dimensional representation of the LTP, not a single-parameter model.

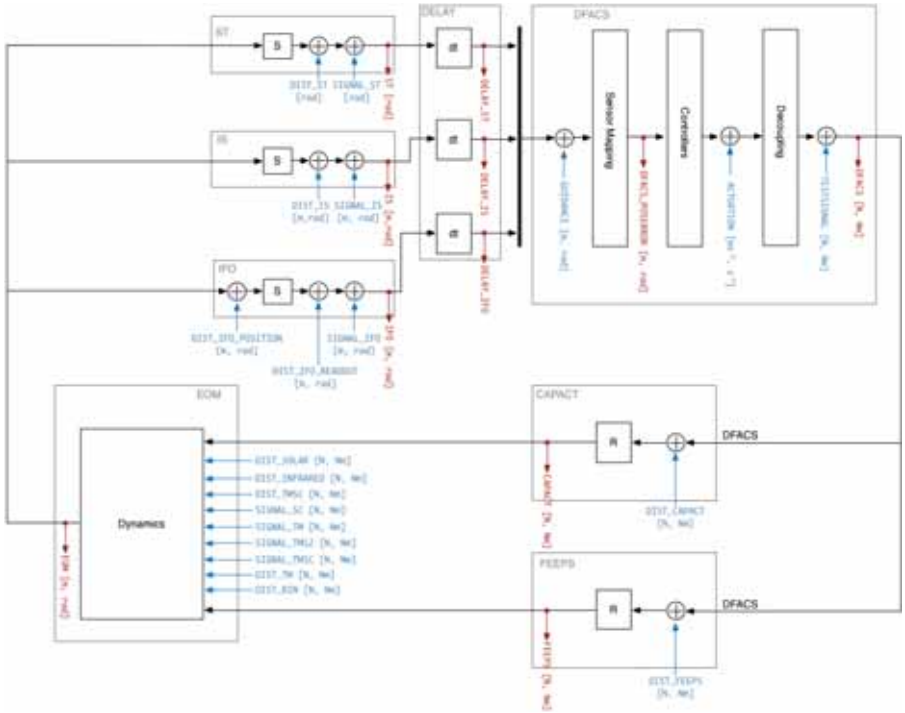

Figure 4.6: Block diagram of the SSM structure. In this diagram, the different sub-module/blocks can be seen; the DFACS, the actuators (thrusters[5] and the capacitive electrodes), the dynamics block, the sensors (IS, interferometer and the star-tracker) and the delay blocks. Each block can be built from different pre-defined version of the particular sub-system. Also, the various injection and noise ports are denoted with blue colour. The noise ports are indicated with the prefix `DIST_` for disturbance. Credit: LTPDA `HTML` help page, [7, 9].

states. A basis change is then operated to express the state coordinates of TM2 relatively to TM1 [4]. The schematics of the `ssm` architecture can be seen in figure 4.6.

The SSM also operates as a simulator, since the instrumental noise shapes studied in the laboratory are incorporated in the model. These models characterise the noise filters that shape the white noise entering the simulator. The noise shaping filters are assembled together with the entire system automatically, and reside in the model library with different options and parameters, allowing the user to customise the noise model during mission science activities. A breakdown of the various sources of the noise is displayed in figure 4.7.

In overall, the LTPDA `ssm` class meets the aforementioned requirements and can be proven to be a very useful tool during the mission. But when it comes to parameter estimation, it shares the same drawback with the analytical method in x-domain, where the controllers must be known and always taken into account in log-likelihood calculations. This, together with the sizeable state-space matrices make the computations heavier.

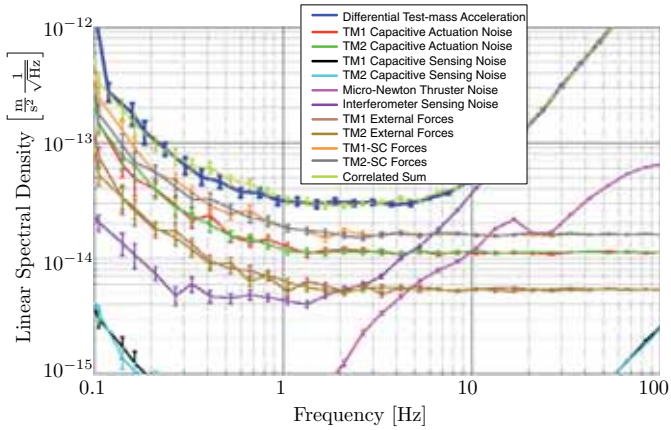

Figure 4.7: The LTPDA SSM simulator noise breakdown. Credit: [8]

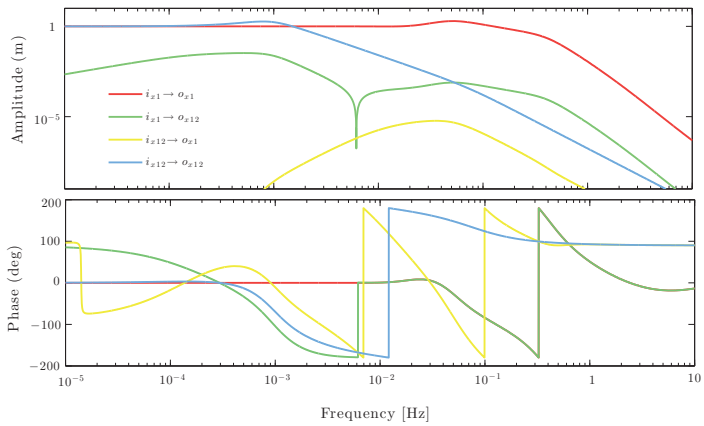

Figure 4.8: The response of the LTP SSM. The different transfer functions of the 2×2 system are showed, for the equivalent example of figure 4.5.

The final approach to the LTP modelling, is to directly express the dynamics in the acceleration domain [10, 11]. This strategy has a series of advantages concerning computational speed and the physics of the system can be more digestible. To begin with, the model is formed by combining the telemetry time-series as

$$\alpha_{model}[n] = \sum_{i=1}^{N} \triangle d_i[n, \{\vec{\theta}\}] + \triangle d_{noise}[n], \tag{4.11}$$

where n is the data samples, the $\triangle d_i[n, \{\vec{\theta}\}]$ are the measured signals processed by some algorithm and depend on the parameter set $\vec{\theta}$, and the $\triangle d_{noise}[n]$ is the residual acceleration noise level. Again, we shall consider the example of the simple one-dimensional

LTP case along the sensitive axis of measurement. Then, the acceleration of the SC, and the differential acceleration between the two TMs is [12]

$$\begin{aligned} \alpha_1 &= \left[\frac{d^2}{dt^2} + (1+\frac{m_1}{M})\omega_1^2 + \frac{m_2}{M}\omega_2^2\right] x_1 + \\ &\quad +(\Gamma_x + \frac{m_2}{M}\omega_2^2)x_{12} + A_{SC}g_{SC} - \frac{m_2}{M}A_2 g_2, \\ \alpha_{12} &= \left[\frac{d^2}{dt^2} + \omega_2^2 - 2\Gamma_x\right] x_{12} + (\omega_1^2 - \omega_2^2)x_1 - A_2\frac{g_2}{m_2} + A_1\frac{g_1}{m_1} \end{aligned} \tag{4.12}$$

where g_i the applied forces on the TMs and SC, A_i are the actuator gains, ω_1^2 and ω_2^2 are the parasitic stiffnesses on TM1 and TM2 respectively[6], and Γ_x the gravity gradient between the TMs. Here, we assume the same interferometer imperfection as in (4.9)

$$\begin{aligned} x_1 &= o_1(t-\tau), \\ x_{12} &= o_{12}(t-\tau) + \delta_{21}o_1(t-\tau), \end{aligned} \tag{4.13}$$

with an additional delay on the interferometer readout τ. In fact, this delay could be applied on the commanded forces g_i, since it doesn't really matter whether we delay the forces or *advance* the interferometer readings. Even if there is time delay effects on both procedures (g_i or o_i), the one measured is the total delayed time from all the processes. Another solution is to consider only one delay parameter on a interferometer channel, which can be interpreted as the relevant delay between the channels. The A_1 and A_2 are often written as $A_{sus,1}$ and $A_{sus,2}$, since they represent the gain of the suspension loop for TM1 and TM2 respectively. The A_{SC} expresses the drag-free loop gain and is also often expressed as A_{df}. But we will drop this notation for the sake of intelligibility and we will keep the more readable index that dictates the body that the force is acting.

The obvious benefit in this analytical representation of the dynamics, is that the controllers' transfer functions are not present, and the overall expressions becomes much smaller and intuitive. The actuation forces are available as telemetry, and they can be directly subtracted following the Newtons' law in eq. (4.12), instead of computing them through transfer functions when working with SSM or analytical models in the displacement domain. The absence of the controllers in the mathematical expressions allows us also to model any given system identification experiment (like the cross-talk in Chapter 5), but also any other investigation performed under different control modes of operation.

But the major gain of this approach is the following. We consider that the LTP is a closed loop system where the interferometer displacement readings $\vec{o}(t)$ are used to calculate the forces to be applied as compensation forces, to counter-balance the external disturbances. From (4.3) and (4.12), and if we follow the notation from [13], we can derive, that in general the dynamics can be described by a linear differential equation with constant coefficients as [14]

$$\triangle\vec{o}(t) = \vec{\alpha}(t), \tag{4.14}$$

6 We can also use the differential stiffness $\delta\omega^2 \equiv \omega_2^2 - \omega_1^2$ in the formula.

where $\triangle$ is the Laplacian operator. Then, there is a steady-state solution $\vec{o}_s(t)$ that depends on the driving inputs $\vec{\alpha}(t)$, and a transient solution $\vec{o}_0(t)$ that depends on the initial conditions $\vec{o}(t_0)$ and $d\vec{o}(t_0)/dt$. The $\vec{o}_0$ is the solution of

$$\triangle\vec{o}(t) = 0, \tag{4.15}$$

and the set of the solutions of eq. (4.15), is called the *kernel* of the operator. Then, if there exists a set of coefficients c_k, and combined with a basis functions ϕ_k as

$$\triangle\vec{o}_0(t) = \sum_k c_k \phi_k, \tag{4.16}$$

then the produced state is still a solution of (4.15). Now, if we apply the $\triangle$ operator to both steady and transient state

$$\begin{aligned} \triangle\vec{o} &= \triangle(\vec{o}_s(t) + \vec{o}_0(t)) \\ &= \triangle\vec{o}_s(t) + \textstyle\sum_k c_k \triangle\phi_k(t) \\ &= \vec{\alpha}(t), \end{aligned} \tag{4.17}$$

since $\triangle\phi_k = 0$ for any ϕ_k lying in the kernel. Therefore the operator automatically suppresses any system transients that are present in the displacement domain. This is of great importance for the LPF due to the slow nature of the systems' dynamics. The response, or relaxation times for the LTP are in the order of tens of thousand of seconds, and in contrast to laboratories on ground, it is not feasible to simply wait for the transients to decay for useful data acquisition [13].

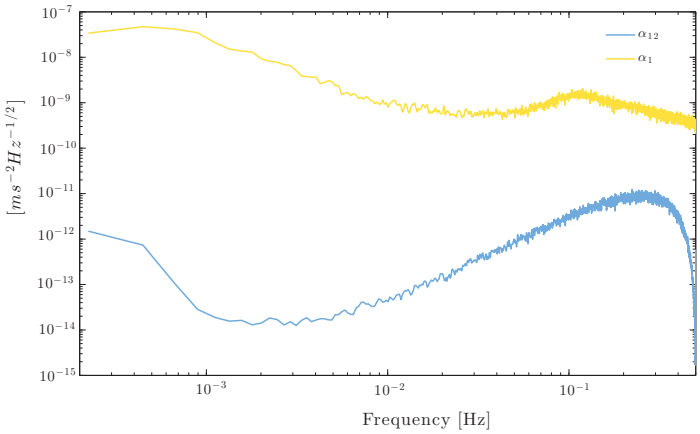

Figure 4.9: The acceleration noise level on the sensitive axis, as generated by the OSE simulator. This is the characteristic acceleration measurement of the LTP when no injection signals are present.

4.3 SYSTEM IDENTIFICATION OVER SIMULATED DATA-SETS

In this section, we will present the results obtained from different simulations and training exercises that happened in the context of LPF data analysis preparation. In addition, each modelling approach requires the equivalent set of assumptions and/or a more suitable method of fitting. The challenges, results and different approaches are going to be summarised. For the training simulations, we have mainly performed the fit on the data, using the analytical acceleration domain representation of the dynamics. This approach was preferred after the unsuccessful attempts on the displacement domain. The non-matching transfer functions between the simulator and the models resulted into unsatisfactory acceleration residual levels.

Concerning data generation, the most widely used LPF simulators are the already mentioned LTPDA SSM, and the OSE. The OSE is an ESA 3D simulator that handles and process the data stream in similar format as in future operations [15, 16, 17, 18]. The data-sets available and analysed here, are generated from the LTPDA SSM simulator, and from the four so-called STOC operational exercises[7]. During the STOC exercises, experiments like TM charge investigations, TM magnetic characterisation, thermal experiments, system identification, etc, that span several days are simulated from the OSE. The STOC simulations aim to

- test and improve the developed algorithms into real-like simulated circumstances.
- improve the pipeline analysis for each planned experiment.
- train the scientific personnel in different special scenarios and various posts during the mission[8].

4.3.1 *In the displacement domain*

The parameter estimation experiments are analysed with the developed MCMC algorithm for the LTPDA toolbox. The algorithm allows the analysis with any desired model format, and is completely tuneable to solve any particular problem. At a first approach we assume a system of the form

$$\vec{y} = \vec{h}(\vec{\theta}) + \vec{n}, \tag{3.22}$$

already discussed in the previous section, that yields a likelihood

$$\pi(y|\vec{\theta}) = C \times e^{-\frac{1}{2}\left(\vec{y} - \vec{h}(\vec{\theta})|\vec{y} - \vec{h}(\vec{\theta})\right)} = C \times e^{-\chi^2/2}. \tag{3.9}$$

The noise appearing in the inner product $(\cdot|\cdot)$ (see again eq. (3.2)) is considered known, and its PSD is estimated from a previously "quiet" run of the instrument. Those so-called quiet *acceleration runs* are going to be performed regularly during the mission, to update the noise levels and shapes.

The first test was to simulate with the SSM simulator the first experiment of guidance injections as in figure 4.10. The model to fit the data was the same as the one

7 More commonly referred to as STOC simulations.
8 The personnel is divided into the technicians, scribes, scientists on duty, and data analysts.

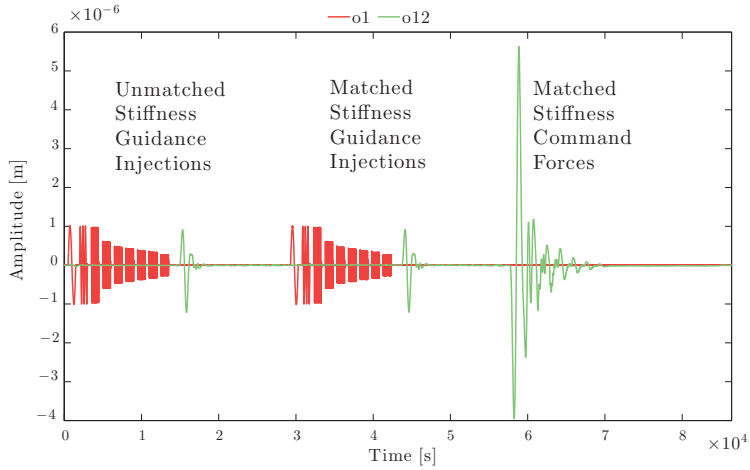

Figure 4.10: Interferometer readouts (o_1 and o_{12}) during the x-axis system identification experiments. The first two experiments are of the same design, that is guidance injections alternately commanded into the two interferometer channels, but with different value of electrostatic stiffness on TM1 ($\omega_1^2 \simeq \omega_2^2$). In the third experiment, OOL forces are commanded on the three bodies of the system. This data-set was generated with the OSE simulator for the STOC exercise 3 [17]. In general, this is the designed and scheduled scheme for the system identification experiments.

that generated them[9], so we expected to get parameter values very close to the true ones. We let a search phase of $T_h = 5 \times 10^3$ samples, a cooling down phase of $T_c = 10^4$ samples, to a total $N_{sample} = 3 \times 10^4$. The proposal was a symmetric normal PDF based on the covariance matrix calculated as the inverse of the FIM as explained in section 3.3. We also considered no prior information available, so all prior densities were set to uniform PDFs. The results for such a toy run can be seen in table 4.2, and as expected, are quite satisfying. The estimated parameter values are in total agreement, within their error margins, with the ones used to simulate the data-set.

Table 4.2: MCMC parameter estimation results from simulated experiments with the SSM simulator. The investigation being analysed here, is the first guidance injection signals, where the system is configured to yield $\omega_1^2 < \omega_2^2$ [1].

Parameter	Real value	Estimated $\pm\sigma$
ω_1	1.3×10^{-6}	$(-1.2999 \pm 0.0002) \times 10^{-6}$
ω_2	1.9×10^{-6}	$(-1.8999 \pm 0.0002) \times 10^{-6}$
A_{df}	0.82	0.8201 ± 0.0002
A_{sus}	1.08	$1.080004 \pm 3 \times 10^{-6}$
τ_1	0.2	$0.2002 \pm 5 \times 10^{-4}$
τ_2	0.2	$0.2003 \pm 2 \times 10^{-4}$
δ_{21}	0.0004	$0.0004001 \pm 1 \times 10^{-7}$

9 Namely, the version of the SSM model was the `LTP version Fitting`.

The next step, is to use the OSE simulator and an analytical model. From the DA team point of view, the OSE is treated as a black box, since the true parameter values are considered to be unknown. The particular simulated data-set was generated for the STOC exercise 6 [3], where its purpose was to test the developed parameter estimation algorithms on a more realistic situation. The experiments were again the unmatched stiffness guidance injection, as in the previous run with the SSM. The model used is the analytical in the displacement domain of eq. (4.4), and the results in this case is shown in table 4.3. The results of the exercise, which in essence is a comparison of the estimated parameters obtained with three different methods, can be found in [9, 3].

Table 4.3: MCMC parameter estimation results the 6^{th} STOC exercise, using different algorithms; the MCMC [2], a linear [8], and a non-linear [19] fitter. The investigation being analysed here, is the first guidance injection signals, where the system is configured to yield $\omega_1^2 < \omega_2^2$. Credit: [9, 3].

	MCMC	Linear	Non-linear
Parameter	Estimated $\pm\sigma$	Estimated $\pm\sigma$	Estimated $\pm\sigma$
$\omega_1 \times 10^{-6}$	-1.31 ± 0.02	-1.31 ± 0.02	-1.31 ± 0.02
$\delta\omega \times 10^{-7}$	-7.150 ± 0.005	-7.160 ± 0.006	-7.160 ± 0.006
A_{df}	1.0694 ± 0.0003	1.0699 ± 0.0005	1.0705 ± 0.0006
A_{sus}	0.99996 ± 0.00002	0.99998 ± 0.00003	0.99996 ± 0.00002
τ_1	-0.1998 ± 0.0002	-0.1982 ± 0.0005	-0.1985 ± 0.0005
τ_2	-0.199 ± 0.001	-0.199 ± 0.001	-0.199 ± 0.001
$\delta_{21} \times 10^{-6}$	1.9 ± 0.3	1.2 ± 0.4	1.2 ± 0.4

For the case of LPF, the knowledge of the system is going to be updated constantly. During operations, system identification experiments are going to be performed in various stages of the LPF schedule. Although the estimated parameters might proven to be time dependent[10], and re-estimating them is necessary, a previous knowledge can be very relevant information for the analysis in line. We can then build normal prior PDFs centered around the values of the previous estimates. The MCMC chains are then shorter, since convergence is achieved easily, and the search phase can be reduced. An example of this can be seen in figure 4.11.

4.3.2 *In the acceleration domain - Iterative* χ^2

The fitting in the acceleration domain procedure was firstly considered during the second STOC operational exercise, and because of it's efficiency, the focus of the team was shifted towards it. Among the advantages of this strategy is computational speed, the absence of slow transients in the data-stream, and no need for the transfer functions of the controllers. But although fitting in the acceleration domain introduces a series of advantages, one should be extra careful when constructing the posterior distribution to be explored.

In the previous case of displacement domain, we consider the PSD of the noise as a fixed quantity, calculated numerically and fed into the parameter estimation machinery.

10 For example, the stiffnesses of the TMs might change after a solar event.

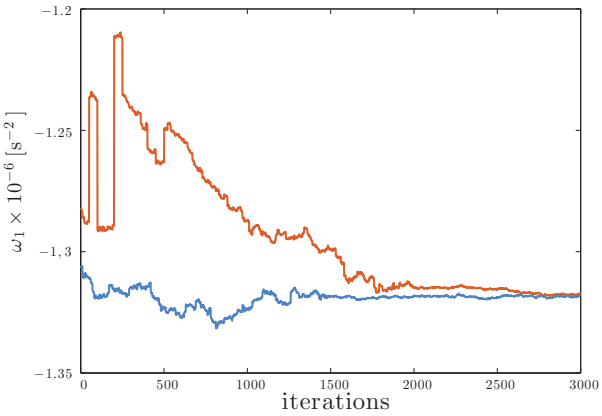

Figure 4.11: An example of the effect of prior PDFs on the LPF analysis. The red curve represents an MCMC chain for ω_1^2, when considering flat prior densities. The blue curve is a chain for the same analysis, but with a wide Gaussian prior defined and centered around the true value [20].

Now, we use the acceleration noise as the noise level, which in general may depend on the parameters of the dynamics to be estimated, so that the $\tilde{S}_n(f)$ of

$$(a|b) = 2\int_0^\infty df\left[\tilde{a}^*(f)\tilde{b}(f) + \tilde{a}(f)\tilde{b}^*(f)\right]/\tilde{S}_n(f), \tag{3.2}$$

now becomes $\tilde{S}_n(f,\vec{\theta})$, since

$$\begin{aligned} \alpha_s(t,\vec{\theta}) &= \triangle_{\vec{\theta}}\vec{o}_s(t) \\ \alpha_n(t,\vec{\theta}) &= \triangle_{\vec{\theta}}\vec{o}_n(t), \end{aligned} \tag{4.18}$$

where α_s the acceleration estimation when the injection signals are present, and α_n the estimation of acceleration during a quiet noise (or acceleration) run, like (see figure 4.9). The first approach to tackle this problem is by *iterative* χ^2 fits on the data. The iterative χ^2 methodology follows the steps below.

1. We first define the initial parameter set, $\vec{\theta}_0$, and estimate numerically the $\tilde{S}_n(f,\vec{\theta}_0)$.
2. Build a log-likelihood function of the form of eq. (3.9), as

   $$\pi(y|\vec{\theta}) = C \times e^{-\chi^2/2}, \tag{3.9}$$

   but with a

   $$\chi^2 = \left(\alpha_s(t,\vec{\theta})\middle|\alpha_s(t,\vec{\theta})\right), \tag{4.19}$$

   including the $\tilde{S}_n(f,\vec{\theta})$ into the inner product (3.2).
3. Then we proceed maximising the $\pi(y|\vec{\theta})$ following, or assign prior densities and sample the posterior $\pi(\vec{\theta}|y)$, to obtain a first estimate $\vec{\theta}_{new}$ of the parameters.

4. Update $\vec{\theta}_0 = \vec{\theta}_{new}$ and iterate from (1) until a convergence criterion is satisfied and get the final $\vec{\theta}_{N_{iter}}$ after N_{iter} iterations.

In reality, for the LPF analysis case, the dependance of the $\tilde{S}_n(f, \vec{\theta})$ on the parameter set is expected to be quite small, and at each χ^2 iteration we apply second order corrections. So, for the iterative χ^2 we use fast non-linear minimisation algorithms like the Nelder-Mead Simplex Method [21], and we sample with MCMC the final posterior distribution with $\tilde{S}_n(f, \vec{\theta}_{N_{iter}})$ at the starting point of $\vec{\theta}_{N_{iter}}$. This is done for purely practical issues, as an MCMC simulation at each outer iteration step would be inefficient. An example of the progress of such an iterative χ^2 scheme, can be seen in figure 4.12.

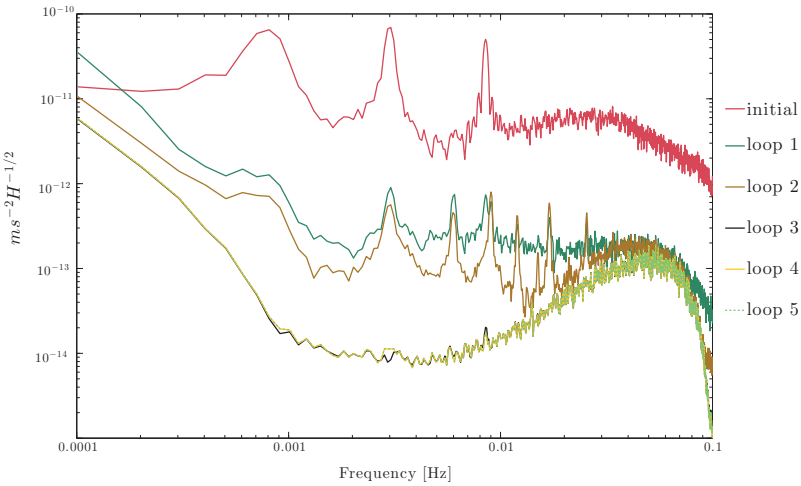

Figure 4.12: Example of the iterative χ^2 scheme fitting the differential acceleration α_{12}. Normally, the first iteration gets values that produce residual acceleration very close to the noise level. But these curves correspond to a high-dimensional model of the cross-talk experiment (see Chapter 5), where the Nelder-Mead Simplex algorithm gets stuck to localities of the likelihood function. This plot is produced during the parameter estimation pipeline analysis developed for operations, see Appendix D.

The iterative χ^2 methodology in the acceleration domain, was first applied to the second STOC simulation [17], that was focused mainly on system identification. It was tested the same time when the usage of the SSM approach to modelling had limited success. This was later proven to be because of the different controllers incorporated in the SSM than the ones developed for the OSE simulator.

Here we present the analysis of two of the simulated days with the OSE, during the 2nd STOC simulation. The first day begins with the de-caging of the TMs, then the system changes operation to science mode (M3), and finally a noise quiet run is being performed. The following day begins with a double experiment. While in unmatched stiffness mode, the first two pre-defined system identification experiments are performed. They are comprised by alternate guidance injection signals to the first and differential interferometer channel, as in figure 4.10. Then, the same experiment is performed, but with modified injection signals, in order to investigate higher harmonics

that are normally visible in the residuals spectra, way over the highest injection frequency. This last design of injections aims to reduce the harmonic overlap, and avoid truncation errors in the parameter modelling the same signals [22].

A first version of the model that was used is very similar to eq. (4.12), but with

$$\begin{aligned} x_1 &= o_1(t-\tau_1), \\ x_{12} &= o_{12}(t-\tau_2)+\delta_{21}o_1(t-\tau_1), \end{aligned} \tag{4.20}$$

with the difference that the interferometer delay was modelled to be different at each channel. The numerical results of the parameters of such a fit on the simulated data, can be found in table 4.4, and the calculated residuals in figure 4.14. In addition, the covariance of the parameters can be estimated (and visualised) from the MCMC chains (see figure 4.13).

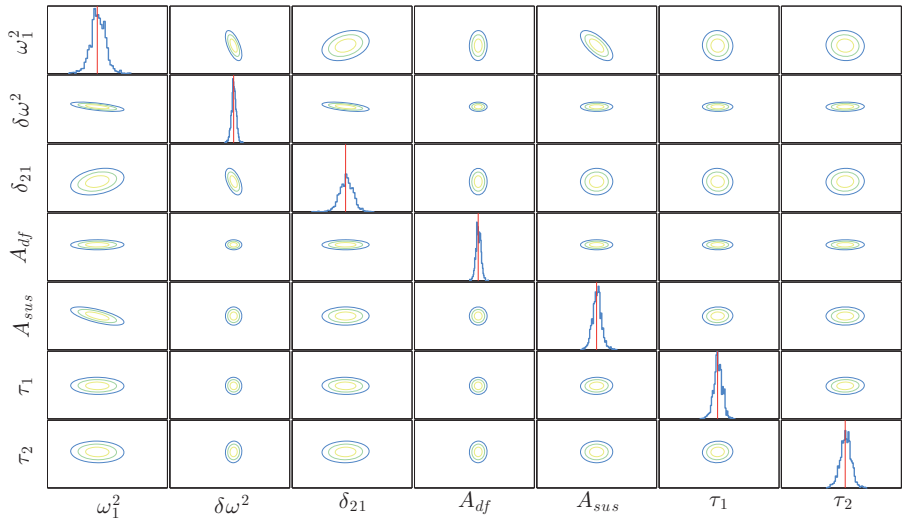

Figure 4.13: The covariance matrix of the parameters from STOC simulation 2. Each one of the lines of the ellipsoids on the off-diagonal elements represent the 1, 2 and 3 σ of the distribution respectively.

In early June 2013, the third STOC operational exercise took place in European Space Astronomy Centre (ESAC) [15]. The philosophy of the simulation was the same as the previous one, only this time there was more variation in the simulated experiments. It lasted five days in total, simulating the *DC potentials*, the *drift mode*, and finally the system identification experiments. The DC potentials experiments focus on calculating the voltage to be applied on the TMs to compensate for the stray potentials on the surface of the TMs. The drift mode experiment is performed under the Drift Mode 2 (DM2) operation mode of the DFACS, and is designed to get a better estimate of the low frequency acceleration noise, by getting rid of the electrostatic actuation noise. This is done by switching off periodically the electrostatic actuation on the TMs. More of the drift mode experiment can be found in [23, 24].

The third simulation presented the opportunity to analyse the complete set of the planned x-axis system identification experiments. For the first time the TMs and SC

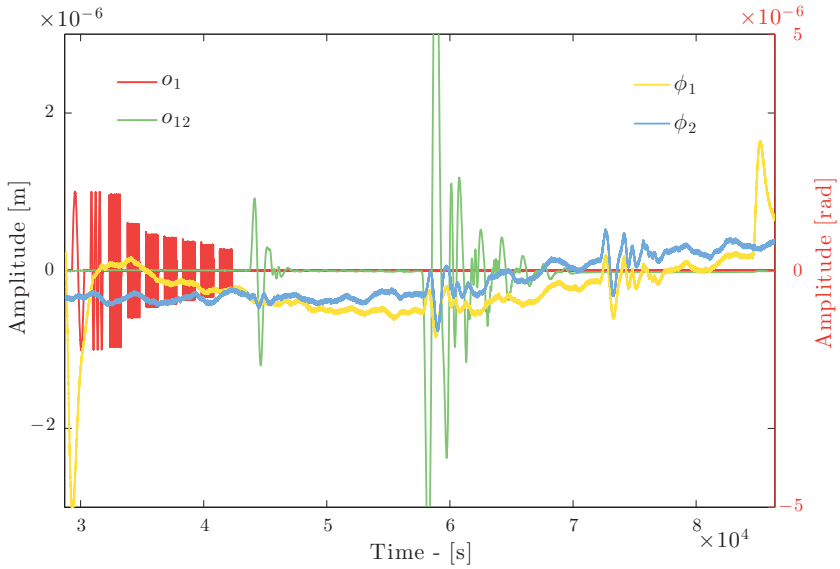

Figure 4.14: Time-series of the matched stiffness experiments of STOC simulation 3. The ϕ_1 time series reveal that the first TM is rotating along the z-axis when the electrostatic stiffness is matched to the second TM. This induces unwanted motion on the first TM, and suggests that there should be a minimum rest time between changes of operation modes.

were directly set in motion via out-of-loop forces. in principle, the same analysis applied to the guidance injections investigations should be applicable directly here, using the same set of equations, as in (4.12). But in practice, the results showed that either a more complicated model was required, either there is another process to be taken into account, either both.

As figure 4.14 suggests, the first thing to consider, is the change of mode from unmatched to matched stiffness. The induced undesirable motion of the first TM, forced us to exclude the guidance injection to the first interferometric channel from the analysis. The same applies to the data segment in the end of the identification experiments, where the system returns to the unmatched stiffness mode. The second consideration came after the unsatisfactory residual curves resulted from a fit with the model of eq. (4.12). While this particular model is proven to provide with adequate estimations for the case of the guidance injections, it showed poor results for the open loop experiments (see figure 4.15). In addition, the estimated parameters were far from the expected values, in comparison with the previous guidance injection investigations.

With this at hand, it was suggested that maybe the issue was relevant to the way the commanded out-of-loop and the DFACS calculated forces were added together. A new model was then formed as

$$\begin{aligned} \alpha_1 &= \left[\frac{d^2}{dt^2} + (1+\frac{m_1}{M})\omega_1^2 + \frac{m_2}{M}\omega_2^2\right] x_1 + \\ &\quad + (\Gamma_x + \frac{m_2}{M}\omega_2^2)x_{12} + A_{SC} g_{SC} - \frac{m_2}{M} A_2 g_2, \end{aligned} \tag{??}$$

$$\alpha_{12} = \left[\frac{d^2}{dt^2} + \omega_2^2 - 2\Gamma_x\right] x_{12} + (\omega_1^2 - \omega_2^2)x_1 - A_2 \frac{g_2}{m_2} + A_1 \frac{g_1}{m_1},$$

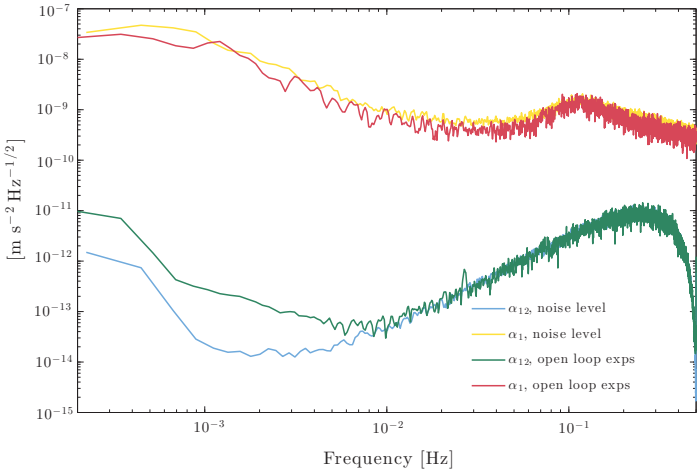

Figure 4.15: First calculation of the residuals for the matched stiffness experiments of STOC simulation 3. It is evident, that the model used is not capable of removing the induced signal and let the residuals reach the noise level.

but with the applied forces calculated as

$$\begin{aligned} g_1 &= g_{1,dfacs} + A_{ool} g_{1,ool}(t - \tau_{ool}), \\ g_2 &= g_{2,dfacs} + A_{ool} g_{2,ool}(t - \tau_{ool}), \\ g_{SC} &= g_{SC,dfacs} + A_{ool} g_{SC,ool}(t - \tau_{ool}). \end{aligned} \tag{4.21}$$

The new expression with the addition of two extra parameters, a gain on the out-of-loop forces A_{ool} and a delay τ_{ool}, was proven to be successful and give better residual acceleration, as seen in figure 4.16. The delay applied on the OOL forces is estimated to be in the order of 0.9 s, something that was verified after the end of the simulation. This time shift was explained to the different pre-processing sequences of the $g_{i,ool}$ and g_i time-series before uploading them to the repositories. The parameter values of the total system identification experiments are gathered in table 4.16. Since the first guidance injection was missing from the last analysis, the parameters sensitive to this experiment were estimated with larger errors, like for example the ω_1 stiffness.

The parameters $pole_{Cap}$ and $pole_{thr}$, are the real poles from a pole-zero model, that filters the applied forces. The general transfer function representation can be written as

$$H(s) = \frac{\prod_{i=1}^{m}(s - z_i)}{\prod_{i=1}^{n}(s - p_i)}, \tag{4.22}$$

where z_i the zeros, and p_i the poles of the system. It was found that the the applied forces differ from the telemetry received, and this difference was successfully modelled with this simple pole-zero filter. This will be discussed in more detail in Chapter 6.

The same analysis was followed for the next simulation [18, 16], the STOC simulation 4. Besides the well established system identification experiments, new investigations were added to the schedule. For the first time, the cross-talk investigations

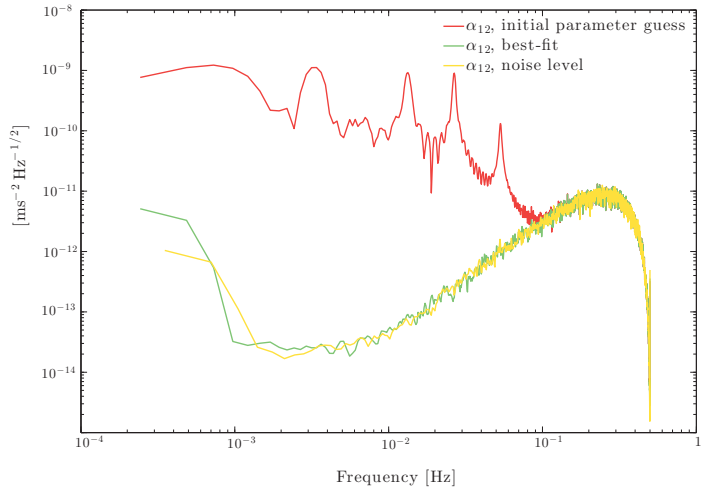

Figure 4.16: Residuals acceleration for the matched stiffness experiments of STOC simulation 3. The red curve is the total acceleration calculated at the initial guess of the parameter values, while the green one is the calculated residuals. The yellow curve is the acceleration noise level estimated from an acceleration quiet run from the first day of the simulation.

were performed (see Chapter 5), but also experiments focusing on thermal and magnetic excitations of the system. This time, the necessary resting time after the switch from unmatched to matched stiffness mode was added in the sequence of commands, eradicating the undesired movement of the first TM. For the unmatched and matched stiffness case, the results are gathered in the summary table 4.4. In addition, an unexpected event was simulated during this training exercise, mimicking a solar radiation event. Then, the team on-duty had to react according to the protocol, in the view of such unforeseen incidents. The acceleration noise levels were then compared to the estimates of previous days, and the magnetic and thermal sensors were checked for unusual readings. A first estimate of the extra stiffnesses of the TMs was at the order of $3 \times 10^{-8}\ s^{-2}$, two orders of magnitude less than the expected value. After an extensive search on the diagnostics items, it was decided to continue with the schedule without entering into a "safe" mode of operation of the satellite (see fig. 4.18).

Table 4.4 gathers all the estimated parameters of the x-axis system identification experiments, for the training simulations conducted over the last three years. Although the analysis was focused on modelling the dynamics of the LTP in the acceleration domain, the differences in models from simulation to simulation are evident. For example, during the second STOC simulation, parameter $\delta\omega^2$ was preferred to the ω_2^2, even if those two quantities are directly connected through the relation of $\delta\omega^2 = \omega_2^2 - \omega_1^2$. In the end, this is a matter of personal preference, since the results are equivalent. For STOC Sim. 2 and 3, the values of the stiffnesses were estimated to the same value within their error margins. On the other hand, the default stiffnesses values were changed for the 4^{th} simulation, and the solar event did not cause any detectable increase on their values.

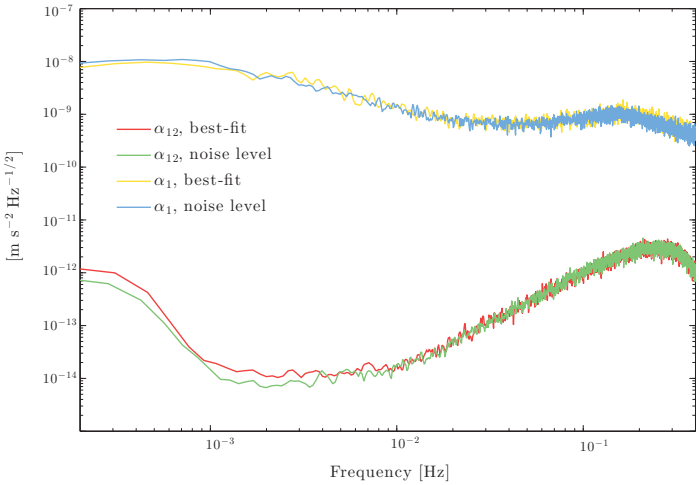

Figure 4.17: Residuals acceleration for the unmatched stiffness experiments of STOC simulation 4.

Also, we assumed different delay parameters for the two interferometer channels, the $\tau_{IFO,o1}$, and $\tau_{IFO,o12}$. Although the analysis showed significant difference of the delays, it later became known, that the delay is in fact the same for both channels in the simulator. The difference found in the particular simulation was later explained due to the difference of the real applied forces and the telemetry forces downloaded for the analysis. We discovered that there is another filtering process applied to the forces time-series. This process was modelled by single real pole filter, and was adapted for the later simulations. The efficiency of this updated model is proven quantitatively in chapter 6. When first modelling in the acceleration domain, we assumed that there is signal leakage from the first to the differential interferometer channel, as in eq. (4.13). The MCMC search over the posterior distribution showed that the parameter δ_{21} is equivalent to zero, confirming that this physical effect is not implemented in the simulator.

Table 4.4: Parameter estimation results for the sys. ID on the x-axis, for all experiments (defined in [1]), for all the STOC Simulations.

Parameter	**STOC Sim. 2** Inv. 1 & 2	**STOC Sim. 3** Inv. 1 & 2	Inv. 3 & 4	Inv. 4, 5 & 6	**STOC Sim. 4** Inv. 1 & 2	Inv. 3, 4, 5 & 6
$\omega_1^2 \times 10^{-6}$	-1.380 ± 0.005	-1.38 ± 0.01	-2.05 ± 0.01	-1.325 ± 0.8	-1.354 ± 0.005	–
$\delta\omega^2 \times 10^{-7}$	-7.07 ± 0.02	–	–	–	–	-2.55 ± 0.03
$\omega_2^2 \times 10^{-6}$	–	-2.133 ± 0.005	-2.12 ± 0.01	-2.130 ± 0.001	-2.2583 ± 0.001	-2.2879 ± 0.0004
τ_{Cap}	–	0.01 ± 0.02	-0.02 ± 0.09	set to zero	–	–
τ_{IFO}	–	0.34 ± 0.02	0.27 ± 0.09	0.301 ± 0.002	–	0.411 ± 0.001
τ_{thr}	–	0.18 ± 0.02	0.10 ± 0.09	0.2576 ± 0.00007	0.0033 ± 0.0002	0.0318 ± 0.0002
$A_{sus,1}$	–	–	–	–	–	$1.00010 \pm 2 \times 10^{-5}$
$A_{sus,2}$	$1.04999 \pm 3 \times 10^{-5}$	1.04995 ± 0.00003	1.0499 ± 0.0002	$1.05000 \pm 3 \times 10^{-5}$	1.04999 ± 0.00003	$1.0500 \pm 3 \times 10^{-6}$
A_{df}	1.021 ± 10^{-3}	1.065 ± 0.002	1.071 ± 0.002	1.009 ± 0.005	0.997 ± 0.001	0.920190 ± 10^{-6}
$pole_{Cap}$	–	0.19 ± 0.01	0.19 ± 0.01	0.1851 ± 0.00006	0.1967 ± 0.0001	0.19584 ± 0.0003
$pole_{thr}$	–	0.17 ± 0.01	0.165 ± 0.02	0.171 ± 0.002	–	–
τ_{OOL}	–	–	–	-0.91328 ± 0.001	–	0.12424 ± 0.0004
A_{OOL}	–	–	–	0.999 ± 0.001	–	$0.99989 \pm 2 \times 10^{-5}$
δ_{21}	$-(7.07 \pm 8) \times 10^{-7}$	–	–	–	–	$-4 \times 10^{-8} \pm 10^{-6}$
$\tau_{IFO,o1}$	$-0.751 \pm 5 \times 10^{-3}$	–	–	–	0.4207 ± 0.0002	–
$\tau_{IFO,o12}$	$-0.498 \pm 2 \times 10^{-3}$	–	–	–	0.40987 ± 0.00003	–
$pole_{OOL}$	–	–	–	3.44 ± 0.01	–	1.29217 ± 10^{-5}

Concerning the gain parameters of the applied forces acting on the TMs, we assumed that the actuators for both TMs were identical, and therefore $A_{sus,1} = A_{sus,2}$. While for the case of the second simulation, there was no experiment performed that we could confirm any differences between the actuators, this changed in STOC simulation 3, where the out-of-loop experiments were performed. We recall, that the last injection signals of the x-axis system identification experiments were designed to excite the system in a way that will reveal the possible "asymmetries" of the system. The TMs and SC are commanded via the same force per unit mass, that nominally should produce a null output for both interferometer channels. This was proven to be the case for STOC simulations 2 and 3 (see figure 4.14), and $A_{sus,1} = A_{sus,2} = 1.05$ within the error. In the following STOC simulation 4, the adapted model was not able to remove all the induced acceleration down to the noise level, because, as it was proven $A_{sus,1} \neq A_{sus,2}$. In fact, it was estimated that the gain of the actuators commanding forces on TM1 was $A_{sus,1} = 1.00010 \pm 2 \times 10^{-5}$, almost 5% smaller than $A_{sus,2}$. This case will be discussed in more details in chapter 6.

Figure 4.18: The signed document/agreement that operations during STOC simulation 4, should be uninterrupted, after the recorded solar event at 16-11-2013, three days before the on-line analysis of the team on duty.

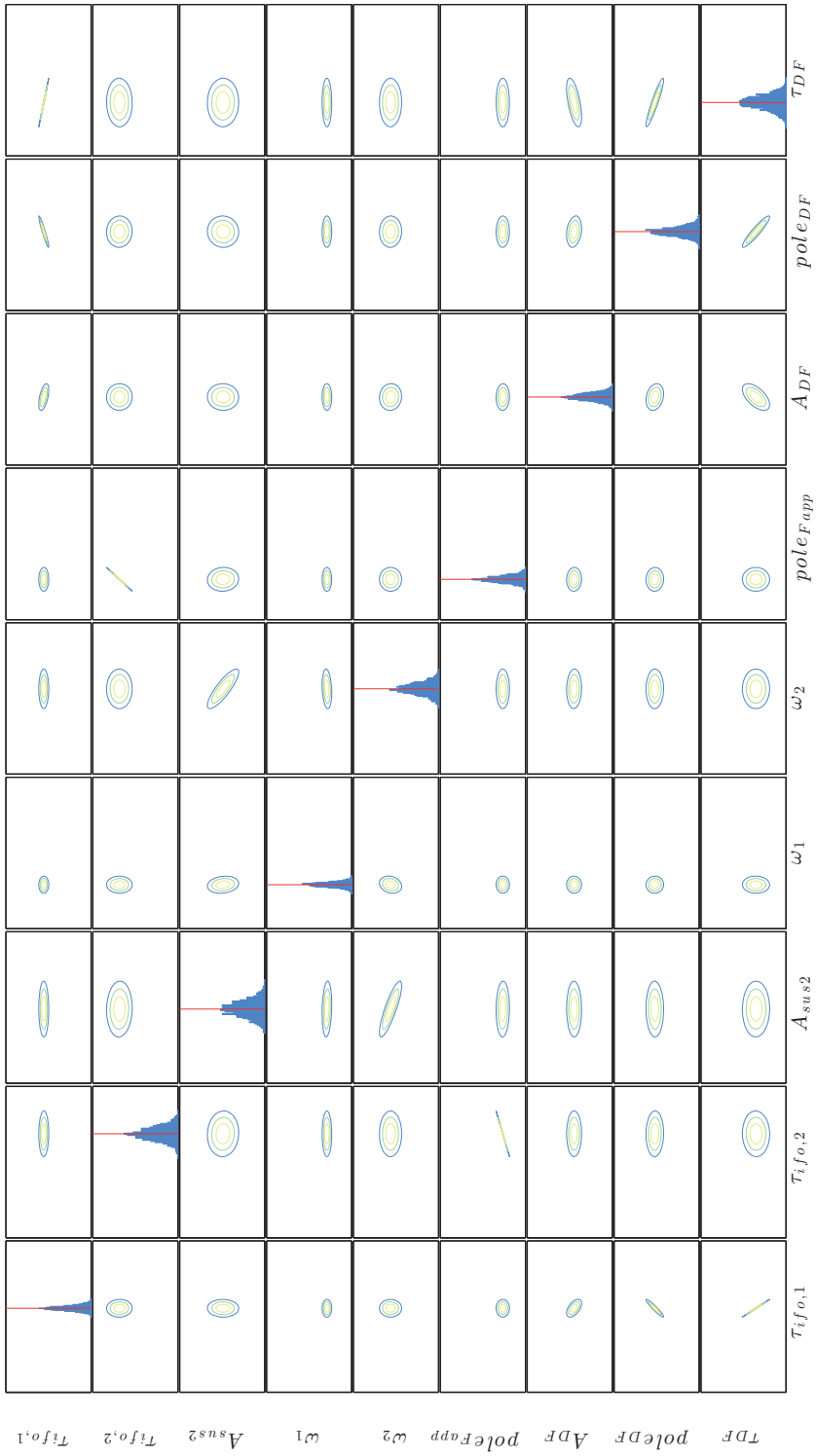

Figure 4.19: The covariance matrix as sampled with MCMC for STOC simulation 4, for the unmatched stiffness experiments.

4.4 NOISE MODELLING

One of the challenges in LTP data analysis, in a similar is that the noise level during system identification might not be available. This may happen due to a various of reasons, like for example data loss, or unknown pollution of the time-series. So, at the beginning of the analysis of each experiment, one has to make a set of assumptions. In particular:

- the noise shape might be unknown during the experiment, and
- the level of knowledge of the noise level will define the best strategy to follow in the analysis.

Up to this point, we have assumed a frequency domain analysis where the noise shape has not changed from the first day of the quiet acceleration measurement, and therefore its PSD is considered known. With this assumption, the $\tilde{S}_n(f)$ term in the inner product

$$(a|b) = 2\int_0^\infty df\left[\tilde{a}^*(f)\tilde{b}(f) + \tilde{a}(f)\tilde{b}^*(f)\right]/\tilde{S}_n(f), \tag{3.2}$$

in the log-likelihood equation 3.25

$$\log\left(\pi(\vec{\theta}|\vec{y})\right) \propto \log\left(p(\vec{\theta})\right) - \tfrac{1}{2}(y - h(\vec{\theta})|y - h(\vec{\theta})) + C, \tag{3.24}$$

is known. But for the case where the noise shape has changed, but it is still comparable to a previous acceleration measurement, one can try to model it in the frequency domain. For example, one may follow [25], where the noise Discrete Fourier Transform (DFT) coefficients are associated with some η amplitudes, to be estimated together with the dynamical parameters of the system. The coefficients i of the $\tilde{S}_n(f)$ term is multiplied by a set j of η amplitudes as

$$\tilde{S}_{n,i} \to \eta_j \tilde{S}_{n,i}, \quad i_j < i \leqslant i_{j+1}. \tag{4.23}$$

An example of such a model can be seen in figure 4.20. The likelihood function can then be calculated as

$$\pi(\vec{\theta}|\vec{y}) = C' \exp\left[-\tfrac{1}{2}\left(\chi^2 + N_{j,bins}\textstyle\sum_j \ln(\eta_j)\right)\right], \tag{4.24}$$

where the $N_{j,bins}$ is the number of Fourier bins of each segment, and the sum is performed over the j segments. A test for this likelihood formation can be performed on data generated for previous simulations. We shall take the unmatched stiffness guidance investigations, and compare the iterative χ^2 scheme of sub-section 4.3.2, with the noise weighting procedure we just introduced. The proposal distribution for this extended set of parameters, is the combination of the multivariate Gaussian with $\Sigma \equiv F^{-1}$ and a multivariate Gaussian for the η noise scale parameters. The second PDF to draw samples from, is formed by taking into account the width of the normal prior densities for each η [26]. Each sample is drawn from a normal distribution of

$$\pi(\eta) \propto \exp\left[\frac{-(1-\eta_j)^2}{2\sigma_j^2}\right], \quad \text{with} \quad \sigma_j = \beta \times 1/\sqrt{N_{j,bins}} \tag{4.25}$$

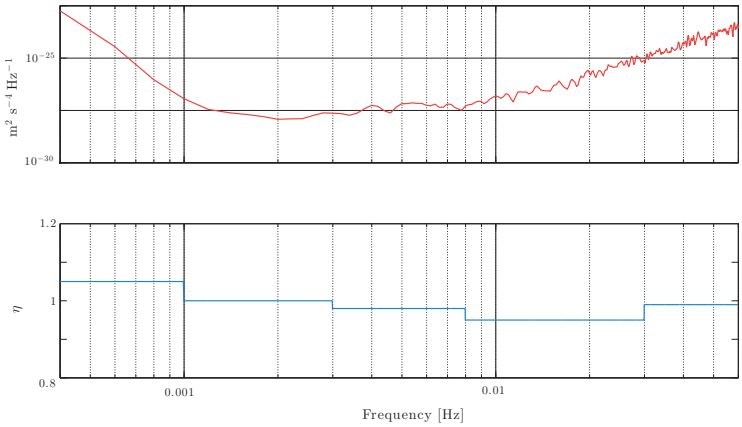

Figure 4.20: Example of modelling the noise with η amplitude coefficients. The coefficients are multiplied with the spectrum of the top panel, their value to be estimated together with the parameters of the system.

with a variance that is the scaled –by a factor β– width of the prior distributions. The β factor embodies our level of knowledge on the current noise level. If we expect that there is insignificant variation of the noise level, then a reasonable choice is to set $\beta = 1$, whereas if not, we can increase it to an arbitrary amount.

The results can be seen in figure 4.21, where the PDFs of the parameters for both techniques are superimposed. The difference is almost indistinguishable, and this because of the nature of the particular experiment. The SNR is very large for the two approximations to present any bias.

Another approximation is to model the underlying noise model with a student' t distribution, like in [27]. This treatment is suitable for data showing non-Gaussian properties, due to the tails of the distribution of the noise. In contrast to the grouping treatment of level coefficients of eq. (4.24), now each frequency bin is assumed to follow a bivariate student-t distribution. If one assumes Inverse-χ^2 prior densities for the variance of the noise coefficients, the marginal likelihood[11] takes the form of

$$\log\left(\pi(\vec{\theta}|\vec{y})\right) = -\sum_i \frac{\nu_i + 1}{2}\log\left(1 + \frac{\chi_i^2}{\nu_i}\right) + C(\nu_i), \tag{4.26}$$

where $C(\nu_i)$ is a normalisation constant based on Gamma functions in ν. In [27], it was proven that the likelihood function of (4.26), works exceptionally for real and simulated data sets [28].

The final road to noise treatment implemented, is the one in [29], where the noise coefficients are marginalised out from the posterior distribution. One begins from the assumption that all the noise sources are zero-mean and Gaussian, so as, the residuals time-series

$$r(n, \vec{\theta}) = \alpha(n) - h(n, \vec{\theta}), \tag{4.27}$$

11 For $\nu \to \infty$, the standard Gaussian likelihood is recovered.

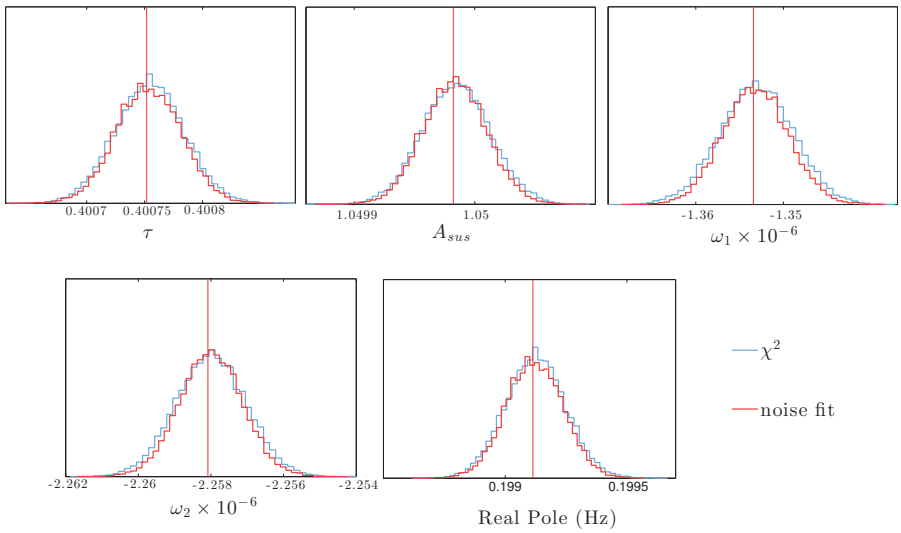

Figure 4.21: Comparison of the resulting histograms following two different techniques to noise modelling. The iterative χ^2 resulting PDFs of the parameters are denoted with blue colour, while the PDFs from a realisation of the (4.24) likelihood with red. For this particular run, the β factor was set to 5, and for the likelihood the calculations a set of 9 η coefficients were considered.

present the same statistical properties[12]. The α term here is the total differential acceleration measured, and the model $h(\vec{\theta})$ can be a linear combination of measured time series, similar to eq. (4.12). In [29], it is shown that for k integers[13] that depend on the adopted spectral window, the variances of $\mathrm{Re}\left\{\tilde{r}(k,\vec{\theta})\right\}$ and $\mathrm{Im}\left\{\tilde{r}(k,\vec{\theta})\right\}$ follow

$$\sigma^2_{\mathrm{Re}\left\{\tilde{r}(k,\vec{\theta})\right\}} = \sigma^2_{\mathrm{Im}\left\{\tilde{r}(k,\vec{\theta})\right\}} = \frac{S_k}{2}. \tag{4.28}$$

The S_k is the frequency averaged discrete time PSD of $r(n)$, at the frequency $f_k = k/NT$. The logarithm of the joint conditional probability density is then given by

$$\log\left(\pi(\tilde{r}|\vec{\theta},\vec{S})\right) = \sum_k \log\left(\frac{1}{(\pi S_k)^{N_s}}\right) - N_s \times \frac{\overline{\left|\tilde{r}(k,\vec{\theta})\right|^2}}{S_k}, \tag{4.29}$$

where we have assumed N_s averages over data stretches. The averages are performed by using Welford's algorithm [30] to improve efficiency and numerical stability. Then, if we assign a uniform priors for the logarithm of the S_k coefficients, we can form a marginal log-likelihood of the form

$$\Lambda(\vec{\theta}) = -N_s \sum_k \log\left(\overline{\left|\tilde{r}(k,\vec{\theta})\right|^2}\right) + C, \tag{4.30}$$

12 Here, n are the time domain samples. In frequency domain it becomes $\tilde{r}(k,\vec{\theta})$.

13 The k integers here refer to the frequency bins. For them to be independent, there should be $|k| \geqslant k_0$ and $|k-k'| > k_1$, where k' and k_1 depend on the spectral window that is chosen. Then the imaginary and real part $\mathrm{Re}\left\{\tilde{r}(k,\vec{\theta})\right\}$ and $\mathrm{Im}\left\{\tilde{r}(k,\vec{\theta})\right\}$, can be also assumed zero-mean and independent Gaussian variables.

which can be proven [29], that is equivalent to the iterative χ^2 scheme explained earlier in this chapter. The likelihood of the last eq. (4.30), will be henceforth called *logarithmic* likelihood.

All the above techniques on the treatment of the noise of the instrument, are already implemented in the LTPDA toolbox framework, but also incorporated in the designed pipeline for the mission on-line analysis. Depending on the experiment requirements, and basically the level of knowledge of the differential acceleration noise curve, the three approaches are to be used accordingly. Work is in progress in creating the fitting protocols for on-line analysis of any given system identification experiment of the LTP, where for each particular experiment the preferred technique is going to be defined and quantitavely justified.

TOY MODEL EXAMPLES

In this small section we will apply the implemented techniques of treating the likelihood functions on a three-parameter toy model. Since we are focusing primarily on the acceleration domain fitting, where the model is a linear combination of time-series, like in

$$\alpha_{model}[n] = \sum_{i=1}^{N} \triangle d_i[n, \{\vec{\theta}\}] + \triangle d_{noise}[n], \tag{4.11}$$

we can assume a toy model like

$$\beta(t) = p_1 x_1(t-\tau) + p_2 x_2(t), \tag{4.31}$$

where x_1 and x_2 are some time-series, and the parameter set to be estimated is $\vec{\theta} = \{p_1, p_2, \tau\}$. The time-series of this simple case model are generated as $x_1 \sim 2 \times \mathcal{N}(0,1)$, and the x_2 is the cumulative sum of $3 \times \mathcal{N}(0,1)$ multiplied by a constant. They are displayed in figure 4.22, where the measurement data-set (red curve) is produced with $\vec{\theta}_{gen} = \{2, -3, 0.2\}$. Then, we can perform system identification analysis using the likelihood functions of eq. (3.9), (4.24), and (4.30). The sampled PDFs of the parameters can be seen in figure 4.23 and 4.25, while figure 4.24 shows the 2-D slices of the likelihood surfaces of all techniques for comparison. In table 4.5, the numerical results are listed. For the case of the χ^2 and the logarithmic likelihoods, we estimated the PSD of the noise and signals respectively, using a Blackman-Harris window and a number of averages of $N_s = 5$ stretches. For the case of (4.24), we assumed three η noise amplitude coefficients spanning over the analysis frequencies $[10^{-4}, 1]$ Hz.

To make a more robust comparison, we performed a Monte Carlo simulation with this toy investigation. After $N_{sim} = 300$ realisations of the data-set, the results can be seen in figure 4.25, and table 4.6. The mean values of the estimated parameters are in total agreement for all approaches to the likelihood function. They also were able to recover the true parameter values of the simulation very well within the error of $\sigma_s/\sqrt{N_{sim}}$.

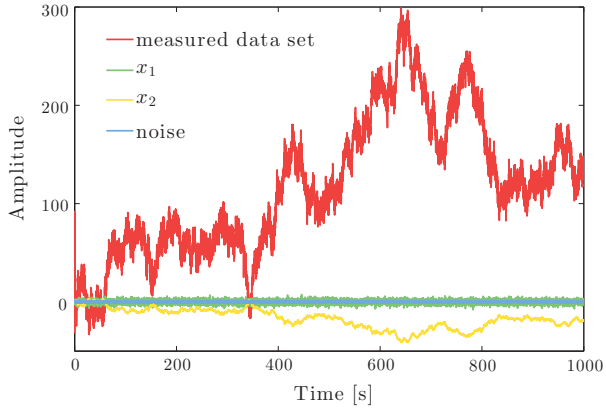

Figure 4.22: The generation time-series of a toy example. The green, and yellow time-series are combined to the resulting red curve (with $\vec{\theta}_{gen} = \{2, -3, 0.2\}$), which is considered the measurement of the experiment.

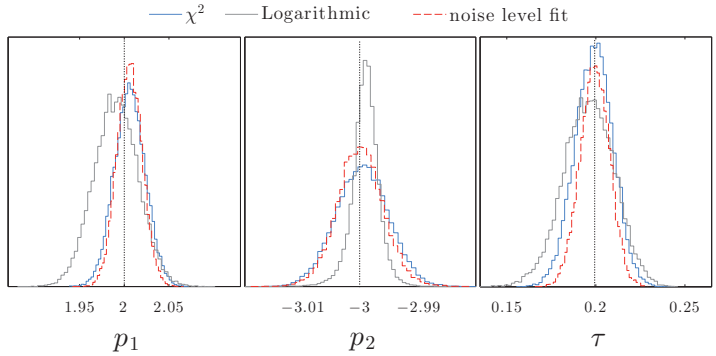

Figure 4.23: The sampled PDFs of the parameters using the three different techniques discussed in this chapter. The black dotted line represents the true values of the simulated data. Figure 4.24 represents the likelihood shapes for each case.

Discussion

In this chapter, we presented an overview of the different approximations to the dynamics of the LTP. The approximations are divided into two categories depending on the chosen domain of analysis; the displacement and acceleration domain. For the first case, analytical and state-space models have been used, both of them used also as internal LTPDA simulators. Then, the system identification experiments were defined as a series of sinusoidal signals injected as forces or displacement readings in various channels of the instrument. Based on the planned experiments, the first mock data challenges were declared successful, since the parameter estimation algorithms developed, were able to remove all the signal induced on the first and differential interferometer channels.

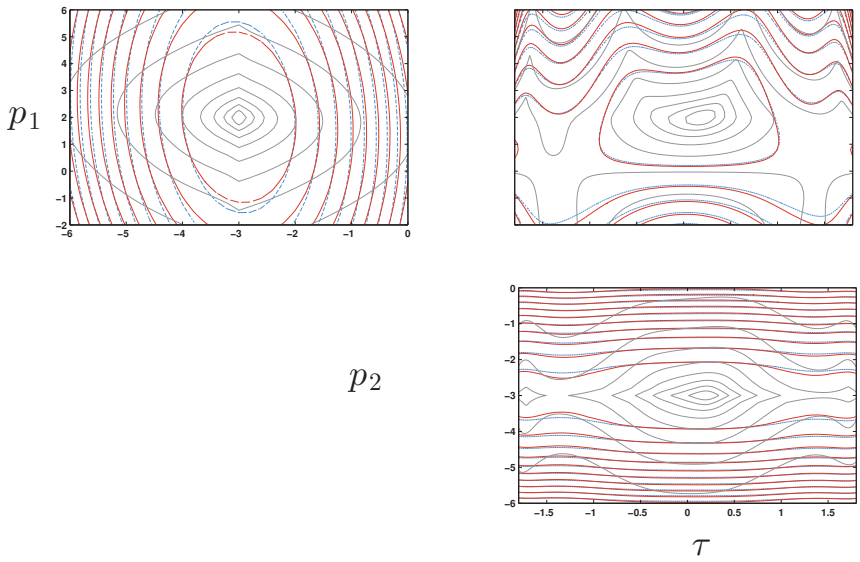

Figure 4.24: The likelihood shape (2D slices with respect to the estimated parameters) for the case of the toy model investigation. The blue dashed line represents the standard χ^2 likelihood surface, the red dashed line one of eq. (4.24) where we model the noise with amplitude parameters, and the light grey solid line refers to the logarithmic likelihood function. Note that this plot does not compare the values of the likelihoods, but only their shape.

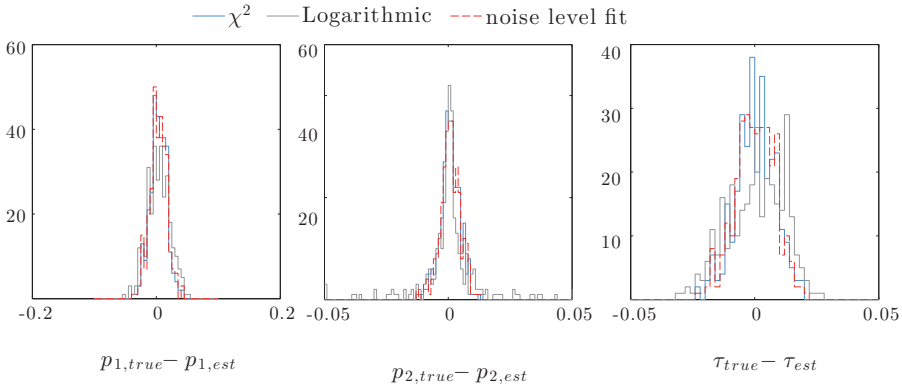

Figure 4.25: The Monte Carlo estimated PDFs on the toy model, after 300 realisations of the noise time-series. Here, θ_{true} is the true values of the simulated data-set, and θ_{est} the estimated one via the MCMC method.

Table 4.5: The estimated parameters for the toy model using different techniques. The corresponding PDFs are displayed in figure 4.23.

Parameter	true value	χ^2	Logarithmic	Noise modelling
p_1	2	2.00 ± 0.01	1.98 ± 0.02	2.00 ± 0.01
p_2	-3	-3.000 ± 0.005	-2.999 ± 0.002	-3.000 ± 0.004
τ	0.2	0.19 ± 0.01	0.19 ± 0.01	0.198 ± 0.008

Table 4.6: A Monte Carlo estimation for the parameters of the toy model, over 300 realisations of the data-set. The "true" column shows the parameter values of the simulations, where $\hat{\mu}$ is the average of the mean values of the MCMC calculations of the parameters PDFs. The σ_{est} is the standard deviation of the 300 mean values, and σ_s is the RMS of the standard deviations of the 300 estimations.

		χ^2			Logarithmic			Noise modelling		
Param.	true	$\hat{\mu}$	σ_s	σ_{est}	$\hat{\mu}$	σ_s	σ_{est}	$\hat{\mu}$	σ_s	σ_{est}
p_1	2	2.000	0.013	0.016	2.000	0.018	0.025	2.000	0.013	0.012
p_2	-3	-2.999	0.004	0.004	-3.000	0.013	0.025	-2.999	0.004	0.003
τ	0.2	0.199	0.008	0.009	0.199	0.011	0.014	0.199	0.008	0.007

The first complication was when the DA team was challenged with simulated data-sets from the OSE simulator. It exposed the only weakness of modelling the dynamics in the displacement domain, which is not other than the presence of the controllers in the equations. The controllers calculate and command the response forces acting on the three bodies of the system. Any given mismatch of the model and the real controller will result to a bias estimate of the parameters, and remaining peaks in the acceleration residuals spectra. The solution came when modelling the system in the acceleration domain, where the controller transfer functions disappear from the equations.

But this induced another degree of freedom in the problem: The noise now becomes parameter dependent, and this has to be taken into account in the minimisation of the log-likelihood. The first way to address this issue, was to develop an iterative χ^2 scheme, where the log-likelihood is minimised sequentially after the acceleration noise is estimated with the new round of estimated parameters. With this technique, the various training simulations were analysed, yielding good results, were the residuals matched the acceleration noise level within the errors. During the simulations, the experiment design was put into stress and then improved, for example as in figure 4.14, were the increase of the first TM stiffness causes unwanted motion, and "pollutes" the experiment with cross-talk elements (see next chapter).

Then, various approximations on the modelling of the noise were considered. Before the analysis of the system identification experiments, assumptions about the knowledge of the noise have to be made. Normally, acceleration runs are performed frequently dur-

ing the lifetime of the LPF, updating the information of the noise level. Then if the assumption that the noise is nearly unchanged, one can model its DFT coefficients with η amplitude parameters. These parameters are then considered in the likelihood function, thus increasing the dimensionality of the problem. Another treatment, is to marginalise the DFT coefficients of the noise out of the posterior distribution and minimise the log-likelihood of eq. (4.30). These techniques were tested and compared with toy investigations, showing similar resulting parameters.

It is worth to mention, that all the analysis performed in this chapter is integrated in the analysis pipelines, to be used during flight operations. A LTPDA pipeline, handles the analysis from the starting point of downloading the telemetry, to submitting the results to sharing repositories. A simplified scheme of this step-by-step analysis can be seen in the appendix D.

[1] S Vitale. Measurement of LTP dynamical coefficients by system identification. Technical Report S2-UTN-TN-3045, 2007. 70, 81, 90

[2] M. Nofrarias, C. Röver, M. Hewitson, et al. Bayesian parameter estimation in the second LISA Pathfinder mock data challenge. *Physical Review D*, 82(12):1–14, December 2010. URL: http://link.aps.org/doi/10.1103/PhysRevD.82.122002, doi:10.1103/PhysRevD.82.122002. 73, 82

[3] M Nofrarias, L Ferraioli, and G Congedo. Comparison of parameter estimates results in STOC Exercise 6. Technical Report S2-AEI-TN-3070, 2011. 73, 82

[4] Marc Diaz-Aguiló. *Magnetic Diagnostics Algorithms for LISA Pathfinder: System Identification and Data Analysis*. PhD thesis, Universitat Politecnica de Catalunya, 2011. 74, 75, 76

[5] A. Grynagier and M. Weyrich. The SSM class: Modelling and Anlysis of the LISA Pathfinder Technology Experiment. Technical report. 75

[6] Martin Hewitson, M. Armano, M. Benedetti, et al. Data analysis for the LISA Technology Package. *Class.Quant.Grav.*, 26:094003, 2009. doi:10.1088/0264-9381/26/9/094003. 75

[7] M. Nofrarias, F. Antonucci, M. Armano, et al. State space modelling and data analysis exercises in lisa pathfinder. In G. Auger, P. Binétruy, and E. Plagnol, editors, *Astronomical Society of the Pacific Conference Series*, volume 467 of *Astronomical Society of the Pacific Conference Series*, page 161, jan 2013. 75, 76

[8] F Antonucci, M Armano, H Audley, et al. LISA Pathfinder data analysis. *Classical and Quantum Gravity*, 28(9):094006, May 2011. URL: http://stacks.iop.org/0264-9381/28/i=9/a=094006?key=crossref.41fc94b94ce025596175f5fe463e5a86, doi:10.1088/0264-9381/28/9/094006. 75, 77, 82

[9] M. Nofrarias, L. Ferraioli, G. Congedo, et al. Parameter estimation in LISA Pathfinder operational exercises. *J.Phys.Conf.Ser.*, 363:012053, 2012. arXiv:1111.4916, doi:10.1088/1742-6596/363/1/012053. 76, 82

[10] Nikolaos Karnesis, Miquel Nofrarias, Carlos F. Sopuerta, et al. Bayesian model selection for LISA pathfinder. *Phys. Rev. D*, 89:062001, Mar 2014. URL: http://link.aps.org/doi/10.1103/PhysRevD.89.062001, doi:10.1103/PhysRevD.89.062001. 77

[11] Giuseppe Congedo, Rita Dolesi, Mauro Hueller, Stefano Vitale, and William J. Weber. Space-borne gravitational wave detectors as time-delayed differential dynamometers. *Phys.Rev.*, D88:082003, 2013. arXiv:1306.1422, doi:10.1103/PhysRevD.88.082003. 77

[12] M Armano, M Benedetti, J Bogenstahl, et al. Lisa pathfinder: the experiment and the route to lisa. *Classical and Quantum Gravity*, 26(9):094001, 2009. URL: http://stacks.iop.org/0264-9381/26/i=9/a=094001. 78

[13] F Antonucci, M Armano, H Audley, et al. From laboratory experiments to lisa pathfinder: achieving lisa geodesic motion. *Classical and Quantum Gravity*, 28(9):094002, 2011. URL: http://stacks.iop.org/0264-9381/28/i=9/a=094002. 78, 79

[14] Giuseppe Congedo. Spacetime Metrology with LISA Pathfinder. 2012. arXiv:1204.4299. 78

[15] M Armano. Plan for the STOC-LTP Simulation 3. Technical Report S2-ESAC-PL-5025, 2012. 80, 85

[16] M Armano. Report on the STOC-LTP Simulation 4. Technical Report S2-ESAC-RP-5020, 2012. 80, 87

[17] M Armano. Plan for the STOC-LTP Simulation 2. Technical Report S2-ESAC-PL-5025, 2012. 80, 81, 84

[18] M Armano. Plan for the STOC-LTP Simulation 4. Technical Report S2-ESAC-PL-5024, 2012. 80, 87

[19] G. Congedo, L. Ferraioli, M. Hueller, et al. Time domain maximum likelihood parameter estimation in LISA Pathfinder Data Analysis. *Phys.Rev.*, D85:122004, 2012. arXiv:1108.0862, doi:10.1103/PhysRevD.85.122004. 82

[20] N. Karnesis, M. Nofrarias, C.F. Sopuerta, and A. Lobo. Improving Markov Chain Monte Carlo algorithms in LISA Pathfinder data analysis. *J.Phys.Conf.Ser.*, 363:012048, 2012. doi:10.1088/1742-6596/363/1/012048. 83

[21] Jeffrey C. Lagarias, James A. Reeds, Margaret H. Wright, and Paul E. Wright. Convergence properties of the nelder-mead simplex method in low dimensions. *SIAM Journal of Optimization*, 9:112–147, 1998. 84

[22] G Congedo. Analysis of STOC Simulation 2. Non-linear parameter estimation with accelerations. Technical Report S2-UTN-TN-3098, 2012. 85

[23] F. Antonucci, M. Armano, H. Audley, et al. The lisa pathfinder mission. *Classical and Quantum Gravity*, 29(12):124014, 2012. URL: http://stacks.iop.org/0264-9381/29/i=12/a=124014. 85

[24] A Grynagier, W Fichter, and S Vitale. The lisa pathfinder drift mode: implementation solutions for a robust algorithm. *Classical and Quantum Gravity*, 26(9):094007, 2009. URL: http://stacks.iop.org/0264-9381/26/i=9/a=094007. 85

[25] Tyson B. Littenberg and Neil J. Cornish. Bayesian approach to the detection problem in gravitational wave astronomy. *Phys. Rev. D*, 80:063007, Sep 2009. URL: http://link.aps.org/doi/10.1103/PhysRevD.80.063007, doi:10.1103/PhysRevD.80.063007. 93

[26] Tyson B. Littenberg, Michael Coughlin, Benjamin Farr, and Will M. Farr. Fortifying the characterization of binary mergers in ligo data. *Phys. Rev. D*, 88:084044, Oct 2013. URL: http://link.aps.org/doi/10.1103/PhysRevD.88.084044, doi:10.1103/PhysRevD.88.084044. 93

[27] Christian Röver, Renate Meyer, and Nelson Christensen. Modelling coloured residual noise in gravitational-wave signal processing. *Classical and Quantum Gravity*, 28(1):015010, 2011. URL: http://stacks.iop.org/0264-9381/28/i=1/a=015010. 94

[28] Christian Röver. Student-t based filter for robust signal detection. *Phys. Rev. D*, 84:122004, Dec 2011. URL: http://link.aps.org/doi/10.1103/PhysRevD.84.122004, doi:10.1103/PhysRevD.84.122004. 94

[29] Stefano Vitale, Giuseppe Congedo, Rita Dolesi, et al. Data series subtraction with unknown and unmodeled background noise. *Phys. Rev. D*, 90:042003, Aug 2014. URL: http://link.aps.org/doi/10.1103/PhysRevD.90.042003, doi:10.1103/PhysRevD.90.042003. 94, 95, 96

[30] Tony F. Chan, Gene H. Golub, and Randall J. Leveque. Algorithms for Computing the Sample Variance: Analysis and Recommendations. *The American Statistician*, 37(3):242–247, 1983. URL: http://dx.doi.org/10.2307/2683386, doi:10.2307/2683386. 95

5 CROSS-TALK

Until now, we have seen the main contributions on the sensitive axis, where we have estimated parameter sets based on the assumption that there is no cross-couplings[1] between different DOF. But commanding movement on the TMs in a DOF other than the x-axis, will result into a detectable signal leakage measured with the differential interferometer channel. This signal excess originates on the so-called cross-talk mechanisms, that are related, for instance, to geometrical imperfections, misalignments of the TMs, or distortion of the field lines of the electrodes.

The possible cross-couplings are of great importance for future space-borne GW antennas, like the eLISA mission. One of the main differences between LPF and the current design of eLISA, is that the GW observatory does not employ actuation along the x-axis, or in other words, the axis joining two TMs in a distance of 10^6 km separating the two SCs. The TMs are actuated along the rest of the DOF, since the x-axis is to remain undisturbed to record oscillations caused by passing GWs. Therefore, the cross-coupling terms of other DOF into the sensitive measurement axis must be known and subtracted from the data stream leaving only the induced GW signal.

For that reason, and with the same logic as in the x-axis experiments, the cross-talk system identification experiments have been designed for LPF. Their objective is to reveal any possible coupling that needs to be understood and disentangled from the main interferometer readout to reach the experimental goal of the mission. Moreover, the knowledge of coupling effects allows us to apply corrections to the system attitude during operations (see for example the piston effect later in this chapter). In the end, the main goal of these investigations is to directly transfer any knowledge gained from the LPF mission to a GW observatory following the concept of eLISA.

In this chapter, we will first introduce the possible cross-coupling mechanisms, and also formulate their contribution in the total differential acceleration. Then, we will analyse the simulated data-set generated for the 4^{th} STOC simulation, where the cross-talk experiments where analysed for the first time. We will focus mostly on the ϕ_1 injection, which is the rotation of the first TM around its z-axis, and gradually build an analytical model that fits the data in a satisfactory way. Then, we will attempt to perform the fit over the complete data-stretch that includes all the performed cross-talk experiments by writing a high dimensional model that includes all the possible cross-coupling coefficients. This is where we enter into analysis areas that fall into the model selection category of problems. The derived high-dimensional model is then re-

1 Either there is no cross-couplings, or it is safe to assume that their effects are negligible during the excitation over the sensitive axis.

visited in chapter 6, where we attempt to improve it by adding[2] physical effects that may contribute to the total acceleration signal respectively.

5.1 THE MAIN CROSS-TALK MECHANISMS

The possible cross-talk mechanisms, can be classified in three main categories [1]

1. *Pick up*: the motion of a DOF is captured by the differential displacement along x;
2. *Actuation*: deviations in the application of forces and torques produce acceleration along x;
3. *Cross-stiffness*: a displacement along a DOF is transformed in a contribution to the differential acceleration along x, through a stiffness coefficient.

The cross-talk signal leakage may originate from a plethora of different mechanisms, the main of them are

- Geometrical: the motion of the TM along a DOF other than x, is projected into the differential channel due to reasons of pure geometry. The *piston effect* falls in this category, where the differential interferometer picks up the rotation of the TM around z and y, and translates it into differential motion. The same output may be generated through misalignments of the TMs. An off-centre position of the TM with respect the IS, will cause cross-talk effects when commanding torques.
- of electrostatic origin: the distortion of the electrical field lines between the electrodes of the different faces of the housing and the TM, can project an electrostatic force along x. Also, geometrical electrode imperfections must be taken into account. In addition, signal leakage into the sensitive channel is expected, since the electrodes that apply torques on the TMs are the same that command forces along the x, y, and z axis. For example, the electrodes used to command rotation along the ϕ angle, are the same that command forces along the sensitive axis.
- Gravitational: a self-gravity imbalance of the SC could affect the TMs motion along x (gravitational cross-stiffness).
- External effects: all environmental causes are falling into this category. Effects like non-uniform thermal gradients, or magnetic forces induce movement along x.

Moreover, the aforementioned leakage mechanisms can also interplay. For example, a change in the relative position of the TMs (a geometric effect) with respect to the EH may induce electrostatic effects. These effects depend also on the charge distribution on the TMs and the EH, that in turn depends on internal factors (for example, the equipotential surfaces on the TMs and the asymmetries in the application of the voltages) and external factors[3].

2 Removing physical effects that do not contribute to the overall acceleration is also a possibility that improves the given model.

3 Like for example, possible solar flares and cosmic rays that charge the TMs and the SC.

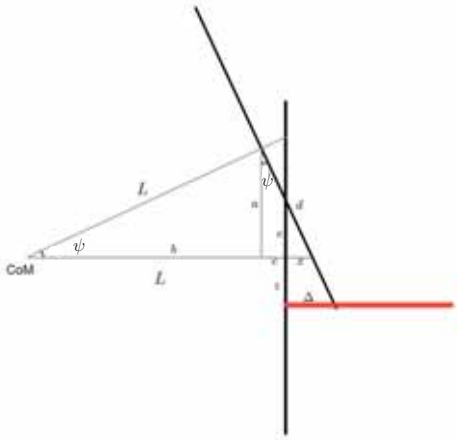

Figure 5.1: Graphical representation of the piston effect. Credit [1].

The piston effect

The piston effect is a way in which the angular movement of a TM around one of its axis (y or z) leaks into the x-axis displacement, through a leverage arm. With the help of figure 5.1, which shows a graphical representation of the piston effect, the cross-coupling coefficients associated to this effect can be calculated. Through geometry, it can be shown that the perturbation to the displacement measurement when the TM rotates, and also leaving room to some possible offset, should be given by [1]

$$\delta_{piston} = (e + y)\tan\psi \tag{5.1}$$

where y is the given offset displacement of the TM with respect to the axis of the satellite. Then, the unknown parameter to be estimated is of e, as

$$e = \frac{x}{\tan\psi} \tag{5.2}$$

and

$$x = d\sin\psi - c = d\sin\psi - \frac{\ell}{2}(1-\cos\psi). \tag{5.3}$$

Then, from eq. (5.2) and (5.3), we can derive that

$$e = \frac{x}{\tan\psi} = \frac{d\sin\psi}{\tan\psi} - \frac{\frac{\ell}{2}(1-\cos\psi)}{\tan\psi} \tag{5.4}$$

and finally, from (5.1)

$$\delta_{piston} = (e + y)\tan\psi = \frac{\ell}{2}\sin\psi\tan\psi - \frac{\ell}{2}(1-\cos\psi) + y\tan\psi. \tag{5.5}$$

If we assume a very small ψ, we get

$$\delta_{piston} = \frac{\ell}{2}\psi^2 + y\psi. \tag{5.6}$$

In terms of differential acceleration, the contribution of the piston effect to the differential readout will be

$$\alpha_{12} = \frac{\ell}{2}(\ddot{\psi}^2) + y\ddot{\psi} \tag{5.7}$$

where $\ell/2 = 23$ mm is half the size of the TM and y is the offset of the TM along the longitudinal DOF we are considering. According to [2], the offset should be equal to $y = 50 \times 10^{-6}$ m. In the following analysis, we will consider the crosstalk from $\phi_1, \phi_2 \rightarrow x$ and consequently we will define the linear and non-linear crosstalk term in the $\alpha = \ddot{o}_\Delta$ time-series as $\delta_{\ddot{\phi}^2{}_{1/2}} \ddot{\phi}^2{}_{1/2} + \delta_{\ddot{\phi}_{1/2}} \ddot{\phi}_{1/2}$. From the above, the non-linear piston coefficient is expected to be equal to the half of the edge of the TM. However, also when the TM faces are not perpendicular[4] with respect to the walls of the IS can produce the same effect.

The cross-stiffness

The TMs are actuated along y and z axis by applying electrostatic forces. This produces a stiffness, or a force gradient, since the induced motion modifies the gaps between electrodes and the TMs, and therefore a mismatch between the commanded and the actual applied force. Moreover, the displacements and rotations could be coupled with the x-axis motion, through the so called cross-stiffness. The cross-stiffness takes into account the total of the possible forces that are acting on the TM: electrostatic, magnetic and gravitational forces, although the electrostatic is the dominant contribution. For example, when the TM rotates around the y-axis, a cross-stiffness is produced which converts the angular displacement ϕ in a force-per-unit-mass along x. We can write it as

$$\alpha_{12} = \ddot{o}_{12} = \frac{1}{m}\frac{\partial F_x}{\partial \phi}\phi = \delta_\phi \tag{5.8}$$

where $\frac{\partial F_x}{\partial \phi} = F_{act,y}$. This term is due to the rotation of the TM while a force along y is applied. Numerical expectation for this crosstalk value can be obtained by computing the RMS of the commanded force along y per unit mass[5]. The physical interpretation of this can be attributed to the distortion of the electrostatic field lines due to the rotation of the TM. This distortion causes a force projection along x.

The cross-stiffness from y to x has not an electrostatic component. The dominant term is the gravitational contribution estimated in [2] equal to 4.912×10^{-8} s^{-2}.

The torque coefficient

The torque coefficient represents the imperfection of the applied torques on the TM. For example, to command a torque around z, the same electrodes that apply a force along x are used (see figure 5.2). Also, a possible displacement of the TMs from the geometrical centre of the EH, results to distorted forces on the TM faces. Given

4 Or even a deformation of the TMs with respct surface close to the spot hit by the laser beam.
5 The commanded forces, as we have seen in previous chapters, are available as telemetry for the analysis.

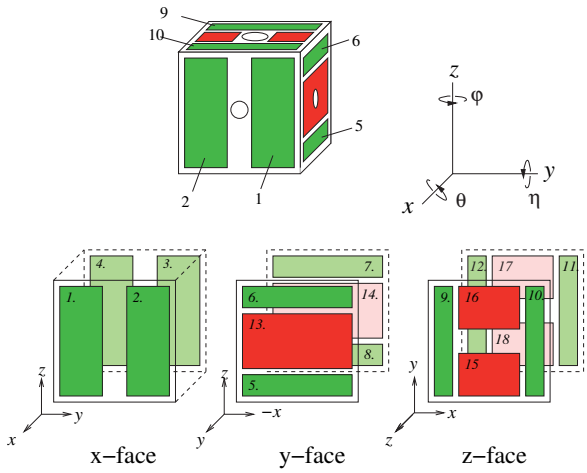

Figure 5.2: Graphical representation of the EH for one TM. As it is clear from the image, the same electrodes used to actuate a torque around z (the angle ϕ) are used to actuate a force along x.

$\Delta r = 21.5$ mm, the mean distance between these electrodes and $\vec{F}_1$ and $\vec{F}_2$ the applied opposite forces to the TM, the applied torque is given by

$$\vec{T} = \frac{\vec{\Delta r}}{2} \times (\vec{F_1} + \vec{F_2}). \tag{5.9}$$

The torque per unit of moment of inertia is given by

$$N = \frac{\frac{\vec{\Delta r}}{2} \times (\vec{F_1} + \vec{F_2})}{\frac{1}{6} m \ell^2} \tag{5.10}$$

where $\vec{\Delta r}/2$ is the arm of the forces, m is the mass of the TM and ℓ il the length of the TM edge. If $\vec{F}_1 = \vec{F}_2 = \vec{F}_0$ the desired "perfect" torque around z is applied, where $\vec{F}_0$ is the nominal applied force in each electrode. But if $\vec{F}_1 \neq \vec{F}_2$ we get also a net force along x. Without the loss of generality, we can assume that $\vec{F}_2 = \vec{F}_0$, and $F_1 - F_2 = \delta F$ is the small imperfection that perturbs the applied torque. Then we can write the net torque per unit of momentum of inertia as

$$N = \frac{\frac{\Delta r}{2}(F_1 + F_2)}{\frac{1}{6} m \ell^2} = \frac{\Delta r (2F_0 + \delta F)}{\frac{1}{6} m \ell^2} \tag{5.11}$$

while the net acceleration induced is

$$a_x = \frac{\delta F}{m}. \tag{5.12}$$

Dividing eq. (5.12) by eq. (5.11) we get that

$$a_x = \frac{\delta F}{(2F_0 + \delta F)} \frac{1}{3} \frac{\ell^2}{\Delta r} N. \tag{5.13}$$

With this in mind, we can predict the value for the cross-coupling coefficient to be

$$\delta_{N_{cmd,\phi 1}} = \frac{\delta F}{(2F_0 + \delta F)} \frac{1}{3} \frac{\ell^2}{\Delta r} \simeq \frac{\delta F}{(2F_0 + \delta F)} \frac{1}{3} \frac{(46\text{mm})^2}{21.5\text{mm}} \simeq 32.8\text{mm} \frac{\delta F}{(2F_0 + \delta F)}. \quad (5.14)$$

From [2] we found that the error in the application of voltage is $\delta V/V = 0.005$. This means that, because $F \propto V^2$, then $\delta F/(2F_0 + \delta F) \simeq \delta F/(2F) = (\delta V/V) = 0.01$. So, if we consider a rotation along the z-axis, we get a first crude value for the corresponding crosstalk coefficient as $\delta_{N_{cmd,\phi 1}} = 32.8 \times 10^{-6}$ m.

The readout equations

Since the equations of motion for the DOF of interest are quite lengthy and do not serve immediate purpose here, they are gathered in the Appendix B. As already discussed, different effects can cause a pick up of the signal. We shall start by considering the most important first, like the piston effect (which if we recall has a linear and non-linear term). Because this contribution is considered a sensing type of signal leaking, the associated crosstalk coefficients δ's have the subscripts $S1$ or $S\Delta$, depending on the channel of interest. Then, the general set of equation considering only this effect, can be written as follows:

$$o_{12} = \Delta x + o_{y1}\delta_{S\Delta y1} + o_{y2}\delta_{S\Delta y2} + \frac{1}{2}\ell\delta_{S\Delta\phi 1}o_{\phi 1} + \frac{1}{2}\ell\delta_{S\Delta\phi 2}o_{\phi 2}, \quad (5.15)$$

while focusing only on the differential interferometer readout. Here Δx is the displacement, and ℓ the TM length. However, in general, we should allow for a leakage of the o_1 readout into o_{12}. If we recall eq. (4.12), then eq. 5.15 becomes

$$o_{12} = \Delta x + o_1\delta_{12} + o_{y1}\delta_{S\Delta y1} + o_{y2}\delta_{S\Delta y2} + \frac{1}{2}\ell\delta_{S\Delta\phi 1}o_{\phi 1} + \frac{1}{2}\ell\delta_{S\Delta\phi 2}o_{\phi 2}. \quad (5.16)$$

In this particular data-set, we have estimated that $\delta_{12} = -(0.04 \pm 1) \times 10^{-6}$ (see again table 4.4), which is essentially a value very close to zero. Hence, on that account, we safely assume that $\delta_{12} = 0$, for the rest of the cross-talk analysis.

5.2 THE EXPERIMENT DESIGN AND THE SIMULATED DATA-SET

To study the cross-talk disturbances, we analyse data-sets taken from the aforementioned 4^{th} STOC operational exercise, that are generated with the OSE simulator. The OSE provides a detailed 3-D environment of the LTP, that allows us to study the dynamics of the system in all DOF. As figure 5.3 suggests, to study the system on the $x - y$ plane, we can inject forces along the x, and y-axis, and rotate the test bodies via torque application around the z-axis[6]. Then, the observed time-series are the *(1)* differential interferometer o_{12}, *(2)* the first interferometer o_1, *(3)* the IS readings, and *(4)* the ϕ angles, via for example the DWS measurements for the TMs.

The system is stimulated by injecting sinusoidal signals, in the same philosophy as in the x-axis system identification experiments [3]. They are defined as sequential

6 Or along the ϕ_j, and Φ angles, where j here refers to the TM, and Φ to the SC.

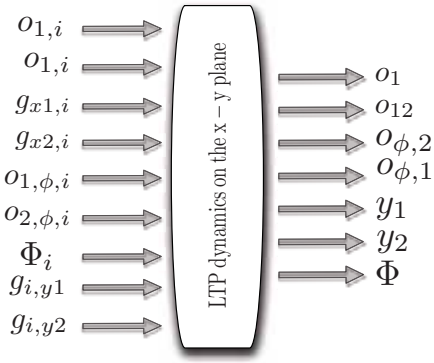

Figure 5.3: The inputs and outputs of the system, when investigating the $x - y$ plane of the dynamics. This figure is, in essence a more detailed version of 4.1.

sinusoidals, with three different frequencies per investigation as shown in figure 5.4. In the following analysis, we will divide the data-set in terms of investigations. Each time, we will analyse the given injection (ϕ_1, ϕ_2, y_1, y_2, and Φ) and attempt to model and fit the cross-coupling effects in all five separate cases. In the end, we will join the separate models that correspond to different investigations into a single expression as in

$$\alpha_{12,ct} = \alpha_{\phi_1 \to a_{12}} + \alpha_{\phi_2 \to a_{12}} + \alpha_{y_1 \to a_{12}} + \alpha_{y_2 \to a_{12}} + \alpha_{\Phi \to a_{12}}, \tag{5.17}$$

that is capable of explaining the complete data segment of the particular simulated cross-talk experiments. Here, each $\alpha_{injection \to a_{12}}$ represents the analytical model derived from the separate analysis of each injection.

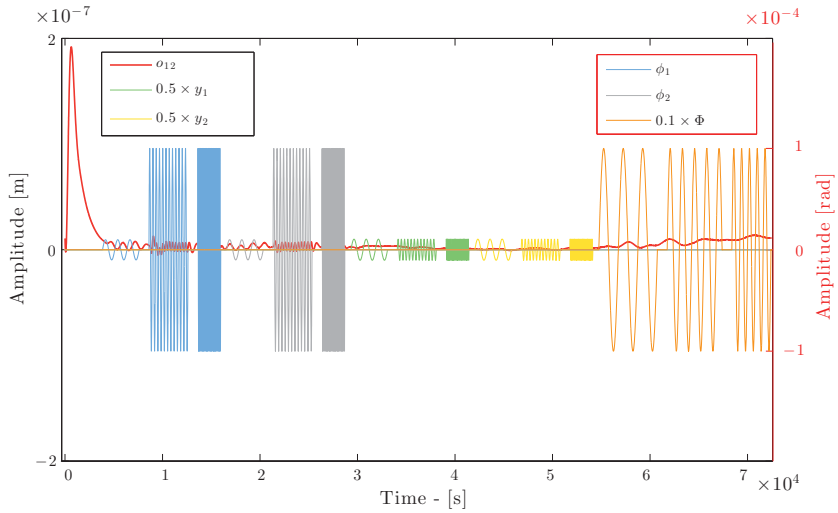

Figure 5.4: The cross-talk experiment injection signals, together with the output of the differential interferometer o_{12}.

5.3 THE ϕ_1 INJECTION

As a first example application, we shall examine now the case of the ϕ_1 injection investigation. To properly analyse it, we start from adding the cross-coupling terms described previously in this chapter, and consider only the terms relevant to this experiment. At this first approximation, we can safely assume that all the other crosstalk contributions to $\ddot{o}_{12}$, are negligible in comparison to the high SNR terms linked to the ϕ_1 injection. Then, we split the data segment to focus on the investigation of the particular experiment, and we can write the following equation

$$\begin{aligned}\alpha_{\phi_1 \to a_{12}} &= -\delta_{\ddot{\phi}_1}\ddot{\phi}_1(t) + \delta_{\phi_1}\phi_1(t) - \delta_{N_{cmd,\phi 1}} N_{\phi_1}(t-\tau) \\ &\quad -\omega_2^2\left(o_{12}(t)+o_1(t)\right) + \omega_1^2 o_1(t) - A_{sus} f_{cmd,x_2}(t-\tau).\end{aligned} \tag{5.18}$$

A time delay has been added to the applied forces or torques (assumed to be the same for applied forces and torques), and it is introduced as a free parameter. This is due to a known feature of OBC implemented in the OSE simulator that takes into account the time from the command of a signal and its actual application. In (5.18), the free parameters are with red colour for clarity, and N_{ϕ_1} is the applied torque along the ϕ angle of TM1. A brief description of all the parameters in this new notation and their expected values is shown in the Table 5.1.

parameter	expected value / first guess	units	mechanism
$\delta_{\ddot{\phi}_1}$	50×10^{-6}	m/rad	Linear Piston
δ_{ϕ_1}	RMS of $f_{cmd,y}$	$m/s^2 rad$	Cross-stiffness $\omega^2_{\phi x}$
$\delta_{\ddot{\phi}_1^2}$	0.023	m/rad^2	Non-linear piston
$\delta_{N_{cmd,\phi 1}}$	16.4×10^{-4}	m	Torque imbalance
ω_2^2	$\simeq -2 \times 10^{-6}$	$1/s^2$	Stiffness TM2
ω_1^2	$\simeq -2 \times 10^{-6}$	$1/s^2$	Stiffness TM1
A_{sus}	1.05	no units	Gain of the suspension
$\delta_{\ddot{\delta}y}$	0.0001	rad	non-orthogonality of TM faces

Table 5.1: The expected terms of crosstalk for the ϕ_1 injection investigation and the initial guess of the parameters, as presented in equation 5.19.

The particular model of eq. (5.18) proved to be insufficient, as most of the signal was not removed, in addition to the very bad parameters estimates. This could be attributed to the large amplitude of the injection excited the non-linear coupling of ϕ_1 to o_{12}. The non-linear piston effect term, that we can write as $\delta_{\ddot{\phi}_1^2}\ddot{\phi}_1^2$, must to be added into the equation as

$$\begin{aligned}\alpha_{\phi_1 \to a_{12}} &= -\delta_{\ddot{\phi}_1}\ddot{\phi}_1 + \delta_{\phi_1}\phi_1 + \delta_{\ddot{\phi}_1^2}\ddot{\phi}_1^2 \\ &\quad -\delta_{N_{cmd,\phi 1}} N_{\phi_1} - \omega_2^2(o_{12}+o_1) + \omega_1^2 o_1 - A_{sus} f_{cmd,x_2}(t-\tau),\end{aligned} \tag{5.19}$$

where we have excluded the (t) dependance of time for the sake of intelligibility. Again, despite the obvious improvement, we discovered a clearly visible "bump" (see figure

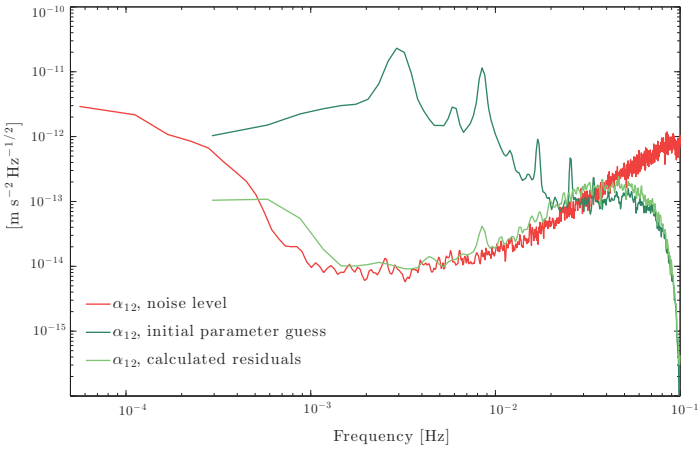

Figure 5.5: The comparison of the acceleration noise PSD (red curve) estimated in a previous noise run with the PSD of the residual acceleration (light green curve) estimated by subtracting from $\ddot{o}_{12}$, $\alpha_{\phi_1 \to \alpha_{12}}$ in the equation 5.18 with the estimated parameters. The dark green curve is the PSD of $\ddot{o}_{12}$. A high frequency peak at around 8×10^{-3} Hz and a bump between 10 and 50 mHz are clearly visible. Credit [1].

5.5), between 10 mHz and 50 mHz, giving hints for the possible improvement of the model. A very rough argument shows that a high frequency feature can be related to a coupling of the acceleration along x with the second derivative of some parameter. In the $x-y$ plane, we can imagine this effect as coming through a piston that convert y into x. A simple way to explain this phenomenon is by assuming non-perpendicular faces of the TM faces with respect the IS walls. The effect is foreseen and apportioned in the Experimental Performance Budget (EPB) to about 10^{-4}rad. Now, we can rewrite the model including $(\ddot{y}_1 - \ddot{y}_2)$ as

$$\begin{aligned} \alpha_{\phi_1 \to a_{12}} \quad = \quad & -\delta_{\ddot{\phi}_1}\ddot{\phi}_1 + \delta_{\phi_1}\phi_1 + \delta_{\ddot{\phi}_1^2}\ddot{\phi}_1^2 - \delta_{N_{cmd,\phi_1}} N_{\phi_1} \\ & -\omega_2^2(o_{12} + o_1) + \omega_1^2 x_1 - A_{sus} f_{cmd,x_2} + \delta_{\ddot{\delta}_y}(\ddot{y}_1 - \ddot{y}_2) \end{aligned} \tag{5.20}$$

The MCMC chains sampled efficiently the unimodal posterior distribution (figure 5.7), and the fit results in a better PSD of the residual acceleration.

Figure 5.6 shows that the first approximation of the model, can describe the data in a satisfactory way. But, a closer look at the results, reveals a small mismatch between the residuals and the acceleration noise level. In particular, a small feature (a bump) around 8×10^{-3} Hz, and a bump at lower frequencies, are visible in the spectrum. The peak feature disappears if we include the η and θ commanded torques in the analysis, something that will be discussed in more detail in chapter 6. There, we will see that different combinations of the parameters in eq. 5.19 together with these extra new terms could produce a PSD of residuals comparable to the noise level.

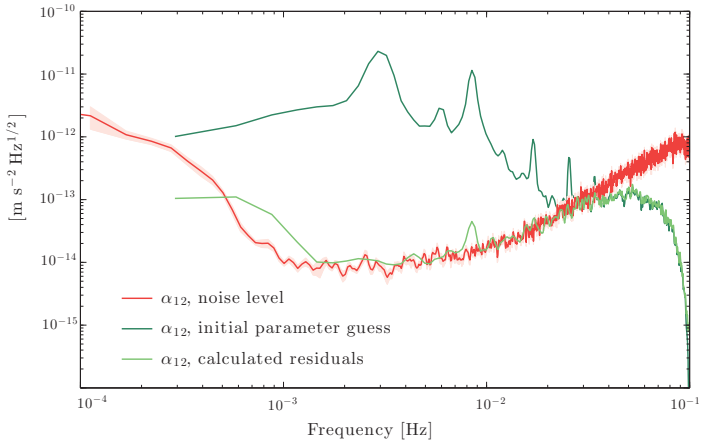

Figure 5.6: The comparison of the acceleration noise PSD (red curve) estimated in a previous noise run with the PSD of the residual acceleration (light green curve) we estimated subtracting from $\ddot{o}_{12}$, $\ddot{o}_{12}, \mathtt{ct}$ in the equation 5.19 with the estimated parameters for the ϕ_1 injection. The dark green curve is the PSD of $\ddot{o}_{12}$. The bump between frequencies 10 and 50 mHz from figure 5.5 has been eliminated, but the peak feature at 8×10^{-3} Hz remains.

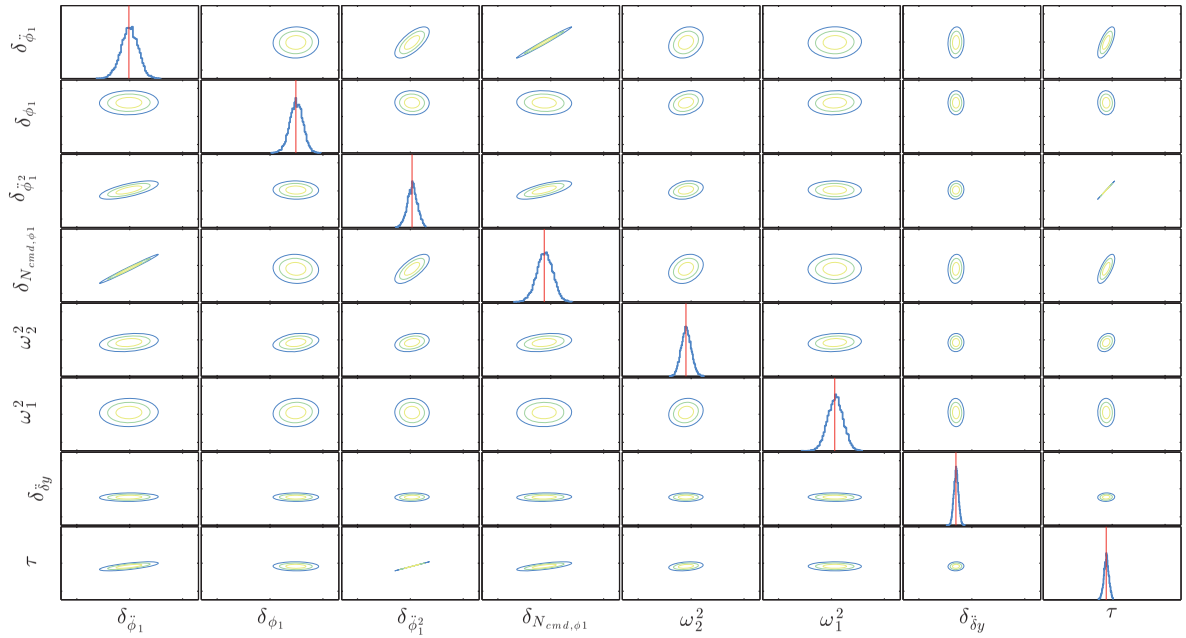

Figure 5.7: The covariance matrix for the ϕ_1 experiment, as sampled with the MCMC algorithm.

Parameter	Initial guess	χ^2 $\hat{\mu} \pm \sigma$	Logarithmic $\hat{\mu} \pm \sigma$	Noise fit $\hat{\mu} \pm \sigma$
$\delta_{\ddot{\phi}_1}$	50×10^{-6}	$(-1.379 \pm 0.004) \times 10^{-4}$	$(-1.35 \pm 0.05) \times 10^{-4}$	$(-1.377 \pm 0.003) \times 10^{-4}$
δ_{ϕ_1}	5×10^{-10}	$(-6.5 \pm 0.2) \times 10^{-10}$	$(-6 \pm 2) \times 10^{-10}$	$(-6.3 \pm 0.2) \times 10^{-10}$
$\delta_{\ddot{\phi}_1^2}$	0.19	-0.1896 ± 0.0005	-0.192 ± 0.007	-0.1898 ± 0.003
$\delta_{N_{cmd,\phi 1}}$	18×10^{-6}	$(-1.4 \pm 3) \times 10^{-7}$	$(-2 \pm 4) \times 10^{-6}$	$(-3.4 \pm 3) \times 10^{-6}$
ω_2^2	-2×10^{-6}	$-(2.05 \pm 0.08) \times 10^{-6}$	$-1 \times 10^{-6} \pm 1) \times 10^{-6}$	$-1.9 \times 10^{-6} \pm 0.1) \times 10^{-6}$
ω_1^2	-2×10^{-6}	$-(1.5 \pm 0.4) \times 10^{-6}$	$-1 \times 10^{-6} \pm 3) \times 10^{-6}$	$-1.2 \times 10^{-6} \pm 0.3) \times 10^{-6}$
τ	1 ms	0.00035 ± 0.00002	0.0009 ± 0.0001	0.00035 ± 0.00001
$\delta_{\ddot{\delta y}}$	-	-0.012 ± 0.007	0.002 ± 0.1	-0.011 ± 0.005

Table 5.2: The estimated parameters for the ϕ_1 investigation compared with the initial guess values and the different approaches of the likelihood (see section 4.4).

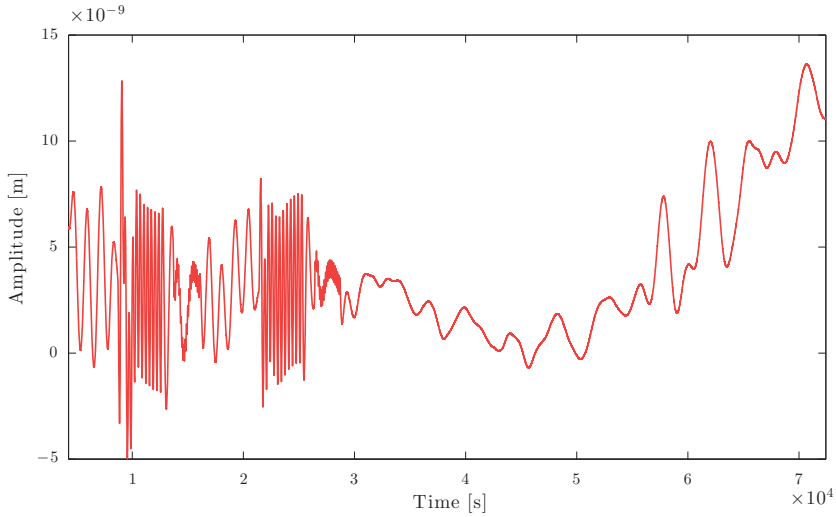

Figure 5.8: The o_{12} interferometer reading during the cross-talk experiments.

5.4 FITTING THE COMPLETE DATA-STRETCH

The analysis strategy applied to the previous section on investigating the ϕ_1 injection, can be followed with the rest of the cross-talk experiments. For each one, we can define an analytical model and perform MCMC searches on the likelihood surfaces. In the end, we can try to fit the complete cross-talk experiments data-set by combining all the previously defined models. This method allows us to perform the complete analysis by also studying the correlations of the cross-coupling parameters. Having already investigated the ϕ_1 injection, we can now write down the equation for the ϕ_2, assuming that the instrument is symmetric concerning the two TMs housing and controllers. Naturally, from eq. (5.20)

$$\begin{aligned}\alpha_{\phi_2\to a_{12}} \quad = \quad & -\delta_{\ddot{\phi}_2}\ddot{\Phi}_2 + \delta_{\phi_2}\phi_2 + \delta_{\ddot{\phi}_2^2}\ddot{\phi}_2^2 - \delta_{N_{cmd,\phi_2}} N_{\phi_2} \\ & -\omega_2^2(o_{12}+o_1) + \omega_1^2 x_1 - A_{sus} f_{cmd,x_2} + \delta_{\ddot{\delta}_y}(\ddot{y}_1 - \ddot{y}_2).\end{aligned} \tag{5.21}$$

Then, following the same procedure analysis for the rest of the injections, we can claim that [1]

$$\begin{aligned}\alpha_{y_1\to a_{12}} = & -\delta_{\ddot{y}_1}\ddot{y}_1 + \delta_{y_1} y_1 - \delta_{y_1} F_{cmd,y_1} - \omega_2^2(o_{12}-o_1) \\ & -\omega_1^2 o_1 - A_{sus} f_{cmd,x_2} + \delta_{\ddot{\phi}_1}\ddot{\Phi}_1 \qquad (5.22a)\\ \alpha_{y_2\to a_{12}} = & -\delta_{\ddot{y}_2}\ddot{y}_2 + \delta_{y_2} y_2 - \delta_{y_2} F_{cmd,y_2} - \omega_2^2(o_{12}-o_1) \\ & -\omega_1^2 o_1 - A_{sus} f_{cmd,x_2} + \delta_{\ddot{\phi}_2}\ddot{\Phi}_2 \qquad (5.22b)\\ \alpha_{\Phi\to a_{12}} = & \delta_{y_1} y_1 - \delta_{y_2} y_2 - \delta_{y_2} F_{cmd,y_2} - \omega_2^2(o_{12}-o_1) \\ & -\omega_1^2 o_1 - A_{sus} f_{cmd,x_2}. \qquad (5.22c)\end{aligned}$$

At the time of the simulation, the Φ experiment was not understood completely, but there was the speculation that it coupled with the TMs through channels already appearing in previous experiments like the (5.22a) and (5.22b). A more detailed analysis

falls in the category of model selection, where one tries to include or exclude physical effects that contribute to the overall acceleration measured. More details for the best model that fits the observation will be presented in Section 6.3 of the following chapter 6. Taking into account eq. (5.20), but also the models for the ϕ_2, y_1, y_2 and Φ injections, an initial guess for the model would be

$$\alpha_{12,ct} = \alpha_{\phi_1 \to a_{12}} + \alpha_{\phi_2 \to a_{12}} + \alpha_{y_1 \to a_{12}} + \alpha_{y_2 \to a_{12}} + \alpha_{\Phi \to a_{12}}. \tag{5.17}$$

where the terms $\alpha_{injection \to a_{12}}$ denote the corresponding cross-talk investigations, and their contribution to the overall differential acceleration. Now, we can start investigating a first approximation of eq. (5.17). If we write down each $\alpha_{injection \to a_{12}}$, and eliminate the terms appearing multiple times, eq. (5.17) can be written as

$$\begin{aligned}
\alpha_{12,ct} = &- \delta_{\ddot{\phi}_1} \ddot{\phi}_1 - \delta_{\phi_1} \phi_1 \\
&+ \delta_{\ddot{\phi}_1^2} \ddot{\phi}_1^2 + \delta_{N_{cmd,\phi_1}} N_{\phi_1}(t-\tau) \\
&+ \omega_2^2 (o_1 - o_{12}) - \omega_1^2 o_1 + A_{sus} f_{cmd,x_2}(t-\tau) \\
&- \delta_{\ddot{\phi}_2} \ddot{\phi}_2 - \delta_{\phi_2} \phi_2 + \delta_{\ddot{\phi}_1^2} \ddot{\phi}_2^2 + \delta_{N_{cmd,\phi 2}} N_{\phi_2}(t-\tau) \\
&- \delta_{\ddot{y}_1} \ddot{y}_1(t-\tau) - \delta_{y_1} y_1(t-\tau) - \delta_{\ddot{y}_2} \ddot{y}_2(t-\tau) - \delta_{y_2} y_2(t-\tau),
\end{aligned} \tag{5.23}$$

where the red coloured terms are the cross-talk amplitudes, ω_i the stiffnesses and τ is a delay. The model time-series in comparison with the measured acceleration time-series, can be seen in figure 5.9. Here we have assumed that $A_{sus} = 1.05$, a direct piece of

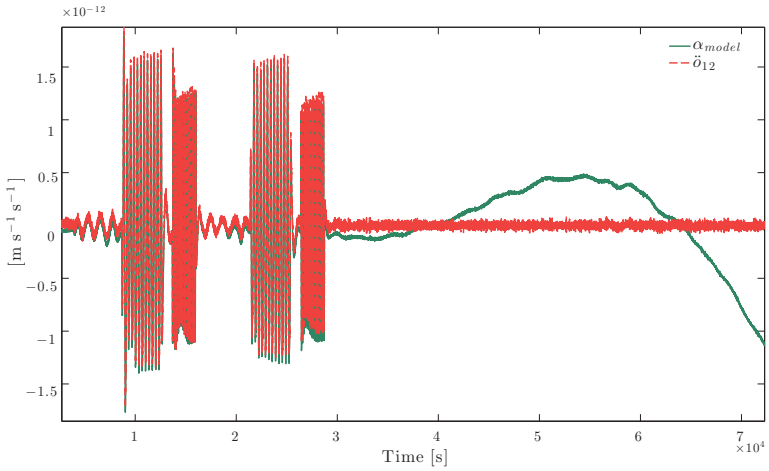

Figure 5.9: Acceleration time series for the complete cross-talk experiments. The model (green) is evaluated at the estimated parameters $\vec{\theta}$, after a run with the MCMC on eq. (5.23) over the data-set.

information from the x-axis system identification experiments analysed in section 4.3. The analysis results for the estimated parameters can be seen in table 5.3, and 5.4, and the residuals in figure 5.10.

Parameter	Initial guess value	Estimated σ
$\delta_{\ddot{\phi}_1}$	50×10^{-6}	$(1.38 \pm 0.003) \times 10^{-4}$
δ_{ϕ_1}	5×10^{-10}	$(-7.3 \pm 0.8) \times 10^{-10}$
$\delta_{\ddot{\phi}_1^2}$	0.19	-0.188 ± 0.005
$\delta_{N_{cmd,\phi 1}}$	18×10^{-6}	$(4 \pm 2) \times 10^{-7}$
ω_2^2	-2.42×10^{-6}	$-(1.88 \pm 0.06) \times 10^{-6}$
ω_1^2	-2.42×10^{-6}	$-(1.59 \pm 0.2) \times 10^{-6}$
τ	0.001	-0.09 ± 0.01
$\delta_{\ddot{\phi}_2}$	0.19	$-(1.301 \pm 0.001) \times 10^{-4}$
δ_{ϕ_2}	-5×10^{-7}	$-(4.91 \pm 0.07) \times 10^{-10}$
$\delta_{\ddot{\phi}_2^2}$	0.1	-0.2293 ± 0.0005
$\delta_{N_{cmd,\phi 2}}$	10^{-4}	$-(4.7 \pm 3) \times 10^{-7}$
$\delta_{\ddot{y}_1}$	10^{-4}	$-(4.3 \pm 21) \times 10^{-7}$
δ_{y_1}	5×10^{-5}	$(1.25 \pm 0.09) \times 10^{-7}$
$\delta_{\ddot{y}_2}$	10^{-4}	$(-7.7 \pm 1.4) \times 10^{-6}$
δ_{y_2}	10^{-6}	$(2.9 \pm 0.5) \times 10^{-7}$

Table 5.3: First parameter estimation results for the cross-talk experiment. The analysis was performed to the down-sampled 0.2 Hz data, employing a standard χ^2 log-likelihood function as in eq. (3.25).

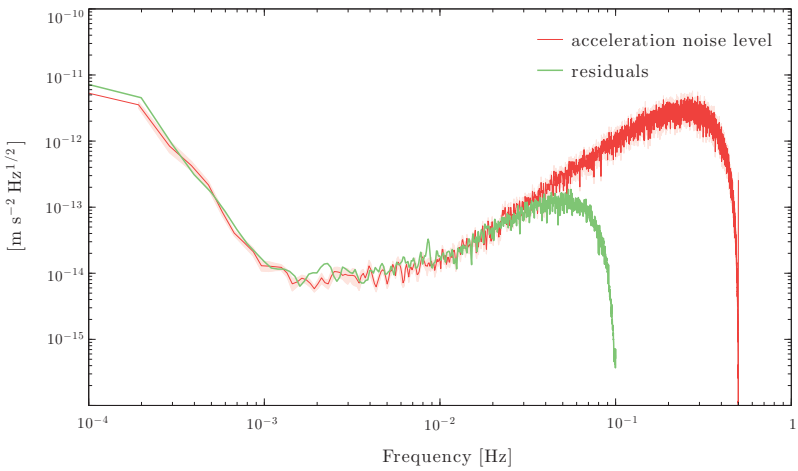

Figure 5.10: The calculated residuals for the complete cross-talk experiment data-stretch in comparison to the acceleration noise measured the first day of the simulation. The PSD of the residuals is comparable within the errors to the PSD of the noise (here visualised as the red shadow), with the exception of a visible feature in the spectrum at around 8×10^{-3} Hz, like for the case of the analysis of the ϕ_1 injection. The analysis here is performed on the down-sampled to 0.2 Hz data.

Table 5.4: The correlation of the parameters taking into account the complete set of cross-talk data for a first version of the model.

	$\delta_{\ddot{\phi}_1}$	δ_{ϕ_1}	$\delta_{\ddot{\phi}_1^2}$	$\delta_{N_{cmd,\phi 1}}$	ω_2^2	ω_1^2	τ	$\delta_{\ddot{\phi}_2}$	δ_{ϕ_2}	$\delta_{\ddot{\phi}_2^2}$	$\delta_{N_{cmd,\phi 2}}$	$\delta_{\ddot{y}_1}$	δ_{y_1}	δ_{y_2}	$\delta_{\ddot{y}_2}$
$\delta_{\ddot{\phi}_1}$	1	0.06	0.3	0.99	-0.38	-0.12	-0.02	0.1	0.5	-0.07	0.09	−0.7	-0.02	0.03	-0.2
δ_{ϕ_1}	0.06	1	-0.05	0.007	0.08	0.05	-0.03	-0.1	-0.04	0.07	-0.1	-0.06	-0.01	-0.03	-0.02
$\delta_{\ddot{\phi}_1^2}$	0.3	-0.05	1	0.32	-0.1	-0.04	-0.04	0.01	0.19	0.0	0.0	-0.24	-0.01	-0.04	-0.09
$\delta_{N_{cmd,\phi 1}}$	0.99	0.01	0.32	1	-0.38	-0.1	-0.02	0.1	0.5	-0.07	0.09	−0.7	-0.02	0.02	-0.25
ω_2^2	-0.38	0.08	-0.12	-0.38	1	0.44	0.16	-0.06	−0.6	0.12	-0.08	0.25	0.02	0.17	0.14
ω_1^2	-0.12	0.05	-0.04	-0.12	0.44	1	0.06	-0.08	-0.26	0.11	-0.09	0.04	-0.01	0.06	0.06
τ	-0.02	-0.02	-0.04	-0.02	0.16	0.06	1	0.22	-0.37	-0.1	0.22	0.01	0.01	0.24	0.05
$\delta_{\ddot{\phi}_2}$	0.1	-0.1	0.01	0.1	-0.06	-0.08	0.2	1	-0.06	−0.64	0.99	0.002	0.04	0.22	0.01
δ_{ϕ_2}	0.5	-0.04	0.19	0.5	−0.68	-0.26	-0.37	-0.06	1	0.04	-0.1	-0.36	-0.03	-0.3	-0.22
$\delta_{\ddot{\phi}_2^2}$	-0.07	0.07	0.0	-0.07	0.12	0.11	-0.1	−0.64	0.04	1	−0.66	-0.0	-0.02	-0.15	0.01
$\delta_{N_{cmd,\phi 2}}$	0.09	-0.11	0.0	0.09	-0.08	-0.09	0.22	0.99	-0.1	−0.66	1	0.01	0.04	0.23	0.01
$\delta_{\ddot{y}_1}$	−0.74	-0.06	-0.24	−0.74	0.25	0.04	0.02	0.0	-0.36	-0.0	0.01	1	0.13	-0.16	0.25
δ_{y_1}	-0.02	-0.01	-0.01	-0.02	0.02	-0.01	0.01	0.04	-0.03	-0.02	0.04	0.12	1	-0.01	-0.05
δ_{y_2}	0.03	-0.03	-0.04	0.02	0.17	0.06	0.24	0.22	-0.32	-0.15	0.23	-0.16	-0.01	1	0.24
$\delta_{\ddot{y}_2}$	-0.25	-0.02	-0.09	-0.25	0.14	0.06	0.05	0.0	-0.22	0.01	0.01	0.25	-0.05	0.24	1

The residuals of figure 5.10 show a good performance of the model at this first stage of the analysis. However, a peak at around 8×10^{-3} Hz shows that a component of the dynamics of the system contributing to this frequency, is not taken into account. This suggests, that there may be a cross-coupling effect from a degree of freedom that is left out of the equation, a speculation that will be further investigated in more depth in section 6.3.

Discussion

In this chapter, we have introduced the cross-talk experiments to be performed onboard the LPF satellite. Similarly to the x-axis system identification experiments, we defined the analysis strategy based on modelling the dynamics in the acceleration domain. This allowed to focus directly on the cross-talk coefficients, without taking into account the controller transfer functions.

We analysed data-sets generated from the last operational training (4^{th} STOC end-to-end simulation), where the cross-talk experiments were analysed for the first time. The planned experiments were designed to stimulate the system along various degrees of freedom, in particular

1. Around the the z-axis of the first TM, or along the ϕ_1 angle equivalently.
2. Around the the z-axis of the second TM, or along the ϕ_2 angle equivalently.
3. Along the y-axis of the first TM, or y_1 for short.
4. Along the y-axis of the second TM, or y_2.
5. Around the the z-axis of the SC, or along the Φ angle equivalently.

The excitation of the system was accomplished via sinusoidal injection forces and torques, acting on the three test bodies. A search in literature, revealed the possible cross-talk terms to be considered in an analytical model. We first split the data-set and analysed each one of the injections, to identify the underlying dynamical model. During this process, we discovered new possible cross-coupling terms, like the non-linear term of the piston effect, or possible pollution of the readings due to actuation of a degree of freedom not taken into account. The parameters estimated, with few exceptions, were in agreement with the expected values, although more detailed analysis is planned for the near future. For the analysis of the ϕ_1, we presented the results using three different approximations of the likelihood function, as described in section 4.4. All methods are in agreement within their error margin, although the logarithmic likelihood, estimated almost an order of magnitude larger errors.

With the residuals level being comparable to the noise level, we then attempted to fit the complete segment of data including all the performed cross-talk experiments. A first high-dimensional model was employed yielding good results, with the exception of the same features on the PSD of the residuals, as in the ϕ_1 investigation, indicating that the model was lacking cross-coupling effects. This problem can be solved with model selection techniques that will be introduced in chapter 6. There, a more suitable model will be proposed that produces residual acceleration equivalent to the noise level.

This work was a collaboration with D. Vetrugno from the University of Trento, that resulted into the Technical Report of [1].

BIBLIOGRAPHY

[1] N Karnesis and D Vetrugno. The Cross-Talk Experiment. Technical Report S2-UTN-TN-3102, 2014. 106, 107, 113, 116, 120

[2] N Brandt et al. Experimental Performance Budget. Technical Report S2-ASD-RP-3036_v24, 2011. 108, 110

[3] S. Vitale. Measurement of cross-talk between the y-axis and the x-axis on the LTP. Technical report. 110

6 BAYESIAN MODEL SELECTION

In the previous chapter about the cross-talk experiment, as well as when analysing the x-axis investigations, we came across some model selection issues. In particular, for the x-axis case, we discovered that a model of a linear combination of the data and delay filters on the applied forces on the three bodies of the system, was insufficient to produce good residuals level. The same applies to the investigations where the injections are forces commanded out of the control loop. There, we found that different pre-processing of the data-streams, caused additional time delay differences on the controlled and out of the loop forces. This problem was more relevant for the cross-talk experiments, specially because of the much higher dimensionality, and the presence of physical effects that contribute with very low SNR to the overall acceleration measured. Examples of this are the non-linear term of the piston effect, or even cross-coupling effects with degrees of freedom not taken into account in the model. Also, acquiring the best model prevents over-fitting issues, since higher dimensionality is penalised.

In this chapter, we will first set the theoretical grounds for model selection techniques, from the Bayesian point of view. Different approximations to the solution of such problems will be discussed, as well as their implications. We discuss the reversible jump MCMC, which is a generalisation of the MH algorithm, that allows trans-dimensional jumps between models. Other methods, such as the Laplace approximations of the posterior around its maximum, are also examined, mostly as cross-check for the heavier in computation MC methods. Then, we apply the techniques to relevant LPF experiments, where we search for the best model that describes the observations. The application on LPF data is wide, and although here we study the system identification cases, the developed model selection techniques were used for the analysis of the magnetic experiments [1].

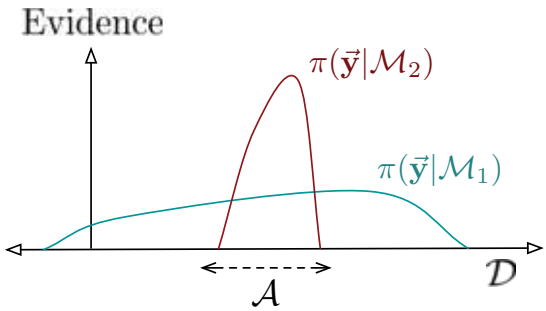

Figure 6.1: Cartoon showing the predictability of two models with different complexity. Here, $\mathcal{D}$ represents the data-sets space. The evidences express this predictability of the models, and are quantified by a normalised probability distribution on $\mathcal{D}$. A higher dimensional and/or more complex model $\mathcal{M}_1$ is able to predict a greater variety of data sets. This means, however, that $\mathcal{M}_1$ does not predict the data sets in region $\mathcal{A}$ as strongly as $\mathcal{M}_2$. Suppose that equal prior probabilities have been assigned to the two models. Then, if the data set falls in region $\mathcal{A}$, the less powerful model $\mathcal{M}_2$ will be the more probable model.

Working in a Bayesian framework, the way to perform model selection to the measured data-sets, is to simply compute the *Odds ratio* between the competing models. The Odds ratio between model X and Y, is defined as

$$\mathcal{O}_{XY} \equiv \frac{\pi(\mathcal{M}_X|y)}{\pi(\mathcal{M}_Y|y)} = \frac{p(\mathcal{M}_X)\pi(y|\mathcal{M}_X)}{p(\mathcal{M}_Y)\pi(y|\mathcal{M}_Y)} = \frac{p(\mathcal{M}_X)}{p(\mathcal{M}_Y)} B_{XY}, \tag{6.1}$$

with B_{XY} being the *Bayes Factor (BF)*, defined as the ratio of the evidences of the models, and $p(\mathcal{M})$ any prior bias for the models, if applicable. We recall that the evidence of a model appears in the denominator of the Bayes rule as

$$\pi(\vec{\theta}|y) = \frac{\pi(y|\vec{\theta},\mathcal{M})p(\vec{\theta})}{\pi(y|\mathcal{M})}. \tag{3.14}$$

In essence, the evidence of a hypothesis X given the data-set $\vec{y}$, $\pi(\vec{y}|\mathcal{M}_X)$, states how much the measured data favours a given hypothesis. Or more accurately, the Bayes theorem rewards models in proportion to how much they predicted the data that occurred. And in general, *"simple models tend to make precise predictions. Complex models, by their nature, are capable of making a greater variety of predictions"* [2]. This means that complicated models will always be able to predict more realisations of measured data-sets than simpler models. But an accurate with respect to the data simple model, will explain the observations in a more satisfactory way.

We give emphasis to the level of complication[1] of a given model for one empirical reason. It is the *Occam's razor*, a rule of thumb that suggests that the simpler model model that explains the data, is the most favourable[2]. This idea is promoted for three reasons. The first one invokes aesthetical reasoning, and the second one is historical, due to the past empirical successes of the theorem. The third and most important one, was stated by David J.C. MacKay as [2, p. 344]

> *"Coherent inference (as embodied by Bayesian probability) automatically embodies Occam's razor, quantitatively".*

It is true, that working with the Bayes rule, we assume the evidence of a model, which encapsulates the Occam's razor automatically into the problem to be solved. A graphical representation that supports the previous statements, is shown in figure 6.1. A counterargument to the Bayesian treatment of selecting the models' complexity, is that the subjectivity of our assumptions (the choice of prior probabilities for example) greatly affects the outcome of the calculations. This might hold for very simple toy problems, but for more realistic applications where the number of data points is large, the importance of the Occam factor greatly surpasses the one of the subjectivity of our assumptions.

In this chapter, we shall use the above ideas and implement several model selection techniques, and finally apply them to LPF simulated data sets. Through the different investigations, an analysis protocol to identify the most probable dynamical model of the LTP will be developed, while the possible challenges at each case are going to be highlighted. But before jumping into the analysis itself, we present the various methods of calculating the heavy integrals of the marginal likelihood.

1 Or the dimensionality of a model, which is the number of free parameters.

2 "Everything should be made as simple as possible, but not simpler" – A quote attributed to A. Einstein, although this current popular state may be a paraphrasing of one of his lectures [3].

6.1 CALCULATING THE BAYES FACTOR

From eq. (6.1), to calculate the Odds Ratio between two models, one has to compute first the marginal likelihood of each model. We can recall that the evidence, can be calculated as

$$\pi(y|\mathcal{M}) = \int_{\Theta} \pi(\vec{\theta}, y|\mathcal{M}) d\vec{\theta}, \tag{3.15}$$

which is the integral on the complete parameter space. Eq. 3.15 can be extremely costly to evaluate, specially when the model becomes complicated with higher dimensionality. For that reason, a number of techniques have been developed to follow to approximate the evidence of a model or directly evaluate the BF [4, 5, 6]. Here, we are going to elaborate on a subset of them, the ones that we are going to use for LPF data analysis.

1. The *Laplace approximations*: The first way of computing (3.15) is by asymptotic approximation[3]. In the beginning, we recall the logarithm of the likelihood as

$$\Lambda(\vec{\theta}) = \log\left(\pi(\vec{\theta}|\vec{y})\right), \tag{3.25}$$

and then we apply Laplace's method: We Taylor expand the (3.25), around $\vec{\theta}_{MAP}$ as

$$\Lambda(\vec{\theta}) \simeq \Lambda(\vec{\theta}_{MAP}) - \frac{1}{2}\left(\vec{\theta} - \vec{\theta}_{MAP}\right)^{T} \mathbf{H} \left(\vec{\theta} - \vec{\theta}_{MAP}\right) + \cdots \tag{6.2}$$

with $\mathbf{H}$ being the matrix with elements

$$H_{ij} = -\frac{\partial^2}{\partial\theta_i \partial\theta_j} \Lambda(\vec{\theta})\bigg|_{\vec{\theta}=\vec{\theta}_{MAP}}. \tag{6.3}$$

Then $\Lambda(\vec{\theta})$ is approximated by an unormalised Gaussian as

$$Q(\vec{\theta}) \simeq \pi(\vec{\theta}_{MAP}|\vec{y}) \exp\left[-\tfrac{1}{2}\left(\vec{\theta} - \vec{\theta}_{MAP}\right)^{T} \mathbf{H} \left(\vec{\theta} - \vec{\theta}_{MAP}\right)\right]. \tag{6.4}$$

In the end, the integral/evidence is approximated as the normalising constant of the Gaussian of eq. (6.4) as

$$\pi(y|\mathcal{M}) \simeq \pi(\vec{\theta}_{MAP}|\vec{y}) \sqrt{\frac{(2\pi)^{D_{\mathcal{M}}}}{|\mathbf{H}|}}, \tag{6.5}$$

where $D_{\mathcal{M}}$ is the dimensions of the model. Indeed, if we assume that we work within a high SNR regime, then the posterior PDF is Gaussian and highly peaked near the maximum likelihood parameters. This can be true for cases of large data samples. In essence, the Laplace approximations perform a comparison between the volume of the models in the parameter space and the volume of the uncertainty ellipsoid of the parameters [5]. Then, we can rewrite eq. (6.5) for the case of model X, as:

$$\pi(\vec{y}|\mathcal{M}_X) \simeq (2\pi)^{D_X/2} |\mathbf{H}|^{-1/2} \pi(\vec{\theta}_{MAP,X}, |\vec{y}), \tag{6.6}$$

3 Often referred as the saddle point approximation.

where $\mathbf{H}$ can be recognised as the Hessian matrix of the posterior distribution. Now, depending on how we calculate, or approximate the Hessian matrix, we can divide the Laplace approximation into two main variations. In the first one we make use of the Fisher Information Matrix $\mathbf{F}$ (see section 3.3), calculated at $\vec{\theta}_{MAP}$, as an approximation to the expected covariance matrix [7, 8]. Then, the evidence of the model becomes:

$$\pi(\vec{y}|\mathcal{M}_X) \simeq (2\pi)^{D_X/2} |\mathbf{F}|^{-1/2} \pi(\vec{\theta}_{MAP,X}, |\vec{y}) \tag{6.7}$$

Of course, the main limitations of this method are associated with the confidence we have on the calculation of the FIM. Furthermore, as expected, the results appear to be poorer in comparison with the other methods as we move towards lower SNR areas. We can follow the notation of [7] and call this particular approximation the Laplace-Fisher (LF) approximation. The second well-known variation is the Laplace-Metropolis (LM) estimator of the marginal likelihood [5]. In this case, we use all necessary components for the calculation of the evidence from previous MCMC estimates. The parameters $\vec{\theta}_{MAP}$ are extracted from the chains of a MCMC parameter estimation run for the particular model, while we use the weighted covariance matrix of the chains Σ, using a Minimum Volume Ellipsoid (MVE) or a Minimum Covariance Determinant (MCD) estimator [9]. The MVE will be discussed in section 6.2. In this case, the evidence of model X can be written as

$$\pi(\vec{y}|\mathcal{M}_X) \simeq (2\pi)^{D_X/2} |\Sigma|^{1/2} \pi(\vec{\theta}_{MAP,X}, |\vec{y}). \tag{6.8}$$

The LM method is considered to be a very reliable tool for the computation of the evidence of a model, since the MCMC can map the posterior surface accurately.

2. The *Schwarz-Bayes Information Criterion (SBIC)*: The SBIC is based on the assumption that the priors for each model follow a multivariate Gaussian PDF and is defined as:

$$\begin{aligned} S \simeq \ln(\pi(\vec{\theta}_{MAP,X}, |\vec{y})) - \ln(\pi(\vec{\theta}_{MAP,Y}, |\vec{y})) \\ -1/2(D_X - D_Y)\ln(n), \end{aligned} \tag{6.9}$$

where D_X and D_Y are the dimensions of each model and n is the number of samples in the data. It can be proven [5] that if $n \to \infty$, then

$$\frac{S - \log B_{XY}}{\log B_{XY}} \to 0, \tag{6.10}$$

and the Schwarz criterion can be a rough approximation to the logarithm of the Bayes factor. In fact, n must be chosen carefully so that $n = N_{eff}$, where N_{eff} is the number of effective samples in the data that represent the growth of the Hessian matrix of the log-likelihood [5].

3. The *Reversible Jump Markov Chain Monte Carlo (RJMCMC)*: An algorithm that automatically penalises higher-dimensional models is the RJMCMC algorithm. The RJMCMC method [4, 10, 11, 12, 13] is widely used when dealing with nested models, meaning that we need to compare a set of models, where simpler models are a subset of a more complicated one. In fact, the RJMCMC algorithm is the generalised case of MCMC methods that is capable of sampling the parameter space and at the same time jumping between models with different dimensionality (see figure 6.2). In essence, it proposes to include or discard extra parameters, which

can be translated to complex and simpler models. The acceptance ratio of this generalised MH algorithm becomes

$$\alpha' = 1 \wedge \left\{ \frac{\pi(\vec{y}|\vec{\theta}_Y)p(\vec{\theta}_Y)g(u_Y)}{\pi(\vec{y}|\vec{\theta}_X)p(\vec{\theta}_X)g(u_X)} |\mathbf{J}| \right\}, \tag{6.11}$$

where $|\mathbf{J}|$ the Jacobian

$$|\mathbf{J}| = \left| \frac{\partial(\vec{\theta}_Y, u_Y)}{\partial(\vec{\theta}_X, u_X)} \right|, \tag{6.12}$$

and $g(u)$ is the proposal distribution from where the "dimension matching" parameters u are drawn [14]. A variation of this method is used in for the LPF data analysis [6, 15] and its details are discussed in the Appendix C.

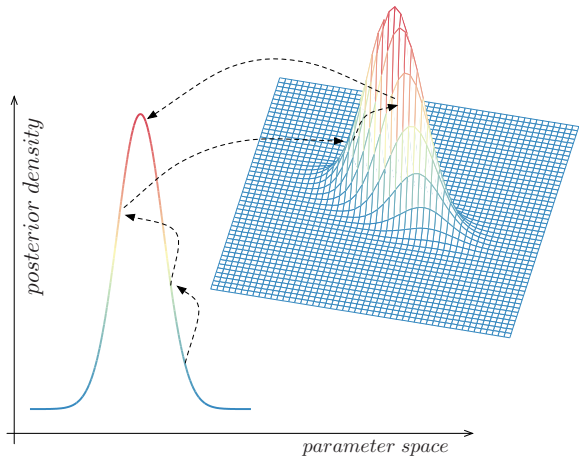

Figure 6.2: Cartoon of the working principle of the RJMCMC algorithm. Being a generalised version of the MH algorithm, it is capable of sampling multiple parameter spaces.

4. *Other techniques*: With the recent progress in cluster computing, many new and more computationally demanding methods were developed. The more popular being the *Thermodynamic Integration* [16, 17] and the *Nested Sampling* algorithm [18, 19].

After computing the evidences, the Odds ratio is straightforward to calculate. If $B_{XY} < 1$, the evidence of model X is negative and the observations support model Y. If $B_{XY} > 1$, the evidence is positive and model X is more favourable than model Y. Many discussions have taken place about the "confidence level" for the preference of a model. In the simplest cases, the comparison yields a Bayes factor that is usually $\gg 1$, but in more ambiguous situations people refer to table 6.1.

6.2 MINIMUM VOLUME ELLIPSOID

One common problem faced in data analysis, is the detection of the best outlier that encapsulates the measured data set. The motive of calculation such an outlier is to

Table 6.1: The Bayes factor confidence levels, taken from [7, 20]. Another interpretation can be found in [21]. The double logarithm of the Bayes factor is often used for the sake of simplicity.

BF_{XY}	$2\log BF_{XY}$	Evidence for model X
< 1	< 0	Negative
1 to 3	0 to 2	Not worth more than a bare mention
3 to 12	2 to 5	Positive
12 to 150	5 to 10	Strong
> 150	> 10	Very strong

find the centre of a point cloud and study the dispersion around this centre. There is a plethora of approximations, one of them being the MVE estimator. The following procedure follows closely the one introduced by P. J. Rousseeuw in[9]. We first assume a data set

$$D = \{d_1, \cdots, d_n\}. \tag{6.13}$$

which we divide it in $p+1$ number of subsets, indexed as $J = \{i_1, \cdots, i_{p+1}\}$. For each subset we calculate the mean and variance

$$\hat{d}_j = \frac{1}{p+1} \sum_{i \in J} d_i \quad \text{and} \quad \Sigma_j = \frac{1}{p} \sum_{i \in j} (d_i - \hat{d}_j)^T (d_i - \hat{d}_j). \tag{6.14}$$

The ellipsoid containing this sub-set of points is inflated or deflated by adding or removing data points according to

$$m_J^2 = \underset{i=1,\cdots,n}{\text{med}} (d_i - \hat{d}_J)^T \Sigma_J^2 (d_i - \hat{d}_J). \tag{6.15}$$

This results to an ellipsoid with volume

$$\left| m_J^2 \Sigma_J \right|^{1/2} = \left| \Sigma_J \right|^{1/2} m_J^p. \tag{6.16}$$

The steps of eq. (6.15) and (6.17) is repeated for all J until we reach convergence to a minimum value of the volume. The computing loop can be extremely long for large data sets, but this can be tackled if one performs the analysis on a sufficient amount of k random sub-sets of data points. Then the new mean and covariance of the data are computed as

$$T(D) = \hat{d}_J \quad \text{and} \quad \Sigma(D) = \left(\chi^2_{p,0.5} \right)^{-1} m_J^2 \Sigma_J, \tag{6.17}$$

with T being a regression estimator, and $\chi^2_{p,0.5}$ is the median of the chi-squared distribution with p DOF. The problem with this procedure is that it is vulnerable to leverage points. To avoid biased results we can use weights w_i applied to the observations as

$$w_i = \begin{cases} 1 & \text{if} \quad \left(x_i - T(D)\right) \Sigma^{-1}(D) \left(x_i - T(D)\right)^T \leqslant c \\ 0 & \text{otherwise} \end{cases}, \tag{6.18}$$

with $c = \chi^2_{p,0.975}$. Then the weighted estimators of the mean and covariance are

$$T_w(D) = \frac{\sum_{i=1}^{n} w_i x_i}{\sum_{i=1}^{n} w_i}, \tag{6.19}$$

and

$$\Sigma_w(D) = \frac{\sum_{i=1}^{n} w_i \left(x_i - T(D)\right)^T \left(x_i - T(D)\right)}{\sum_{i=1}^{n} w_i - 1}. \tag{6.20}$$

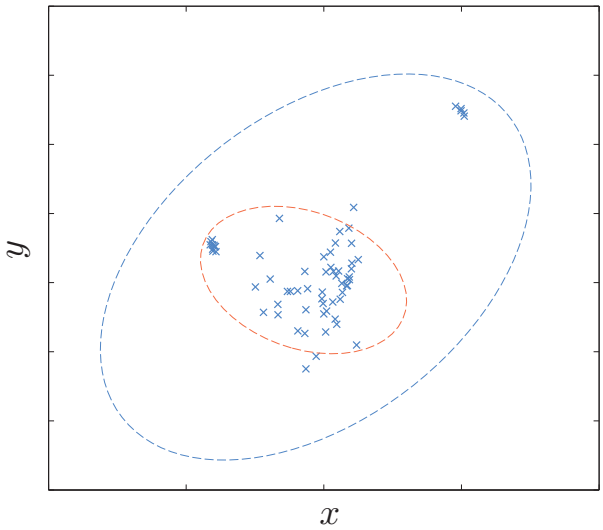

Figure 6.3: Example of the MVE calculation on a small simulated data-set. The blue x marks represent the data points, while the blue dashed line a first estimation of the minimum volume ellipsoid. The orange dashed line is the minimum volume ellipsoid estimated with the reweighed data set and the procedure introduced in this section.

In section 6.1, we introduced the LM approximation to the marginal likelihood. In that case we use the MCMC chains to get an estimation of spread of the posterior distribution. But to get a reliable calculation of the covariance matrix from the MCMC chains, we need a high breakdown point robust estimator [5], and the MVE described is proven to be suitable for our needs [7, 6]. It will be used thereafter in the computation of the LM estimator of the evidence of a model. A toy example of the MVE calculation is presented in figure 6.3.

A TOY MODEL EXAMPLE

Toy models have been used for testing and validating the RJMCMC algorithm implemented for LTPDA, before apply it to more complex LTP. The toy systems employed are the harmonic oscillator SSMs. The simulated data-set was first generated, with a harmonic oscillator with mass $m = 1$ kg, damping coefficient $\beta = 0.1$ kg $\times$ s^{-1} and a

spring constant $k = 0.1\ kg \times s^{-2}$. A sinusoidal signal was again injected to the system, while the output is the measurement of the oscillation movement. Then, the models to compare were defined, as in table 6.2. With the above configurations we expect for

Table 6.2: The harmonic oscillator models to be compared.

model #	Known parameters	Parameters to fit
A	$m = 1\ kg$	k and β
B	$m = 1\ kg$, $k = 0.1\ kg \times s^{-2}$	β
C	$m = 1.05\ kg$, $k = 0.1\ kg \times s^{-2}$	β

the algorithm to “favour" model A and B than model C. The results can be viewed in figure 6.4 and they seem to agree with our expectations. The algorithm output was:

- “positive" when comparing model B and C.
- also positive when comparing model A and C (remember, model C has the wrong mass value).
- “negative" when comparing model A and B. Model number B supports better our data set.
- we can also see that model B is the most favoured of all three. It is an expected outcome, since the algorithm automatically applies an “Occam Razor" to the higher dimension models. At this simple investigation, no prior bias for the models was assumed.

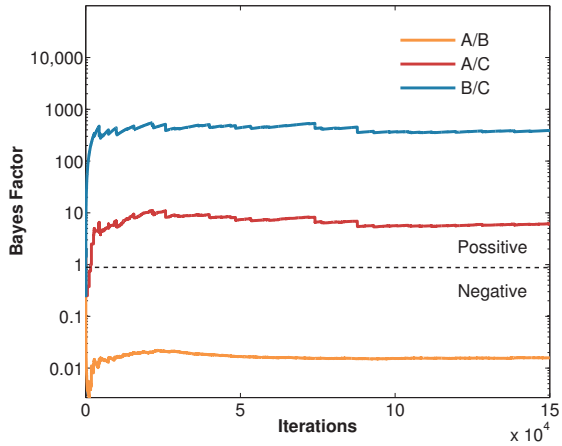

Figure 6.4: In this figure the output of RJMCMC for this first example is presented. Each line represents the evolution of Bayes factor (comparing two models) against the iterations of the algorithm. For example, the blue line is the B_{XY} where X is model B and Y is model C. By recalling eq. (6.1) and looking at this plot we can say that the model B is approximately ten times more probable than model C.

6.3 BAYESIAN MODEL SELECTION FOR LPF

In the previous chapters 4 and 5, we introduced the modelling approaches of the LPF, and begun to analyse the system identification experiments. There, we constructed the models of the dynamics without discussing any reasoning behind the choice of the dimensionality of these models. Here, we will attempt to justify quantitatively the best model, that embodies all the physical processes appearing in the data stream. First, the x-axis case is going to be examined, and then the more complicated case of cross-talk experiments.

6.3.1 *Model selection for the x-axis system identification experiments*

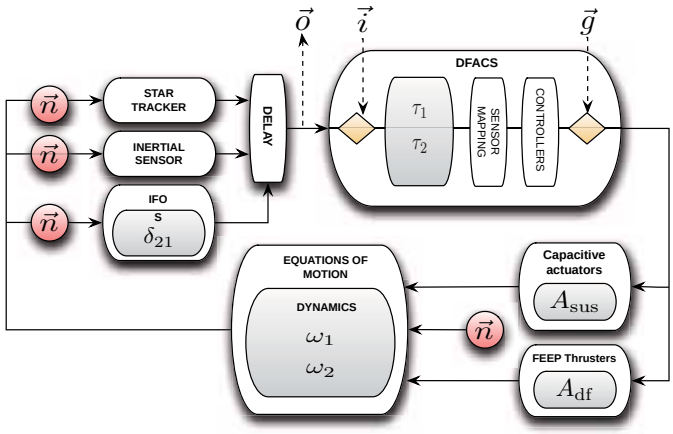

Figure 6.5: Schematics of a simplified LTP SSM (A more complete scheme is found in figure 4.6). It is composed by smaller SSMs of the various subsystems, each one a standalone SSM, here represented with white boxes. The rhombi represent the main injection inputs to the system. We use mainly the first injection port, which represents the interferometric inputs to the system, while the second rhombus stands for the capacitance actuators injection ports. The $\vec{n}$ represents noise contributions from various sources and finally, the parameters to fit, for the sake of convenience, are located in the grey boxes inside of the respective SSMs. The interferometer signals $\vec{i}$ are injected to the controllers (DFACS), where the commanded forces are generated and applied through the capacitance actuators and the thrusters of the space-craft. In the last two of experiments of [22] "out of loop" forces $\vec{g}$ are applied to the three bodies (TMs and SC) of the system. Here, the interferometer output is denoted as $\vec{o}$. Credit: [6].

In order to demonstrate a first model selection application to the LTP analysis, we can investigate the case of a LPF mock data challenge [23, 24], the STOC exercise 6 that we first encountered in chapter 4. The experiment analysed in this mock data challenge was the guidance injections on both interferometer channels, and the "true" values of the parameters of the system were assumed unknown. The first version of the model was proven insufficient to fit the data, but then it was noted that the fit was improved when two extra parameters were introduced. These parameters are the guidance delays, τ_1 and τ_2 already taken into account in chapters 4 and 5. These delays to the application of the guidance signals (see figure 6.5), are caused from operations and data procesing of the DMU. The final robustness of the fit indicates that the new parameters substantially improve the fit. The estimated parameters of the particular

mock data challenge are gathered in table 4.3 in chapter 4.

This problem can be better studied by reducing it to a model selection problem and can be tested with synthetic data-sets. The simulated data source is a LTP SSM system with these delays set to: $\tau_1 = \tau_2 = 0$. With this configuration, we assume a true system where the application signals are applied instantaneously. For our first try-out we injected "fake" interferometric displacements, while for the second investigation we used the same structure of injections but with much lower Signal to Noise Ratio (SNR ~ 5).

In order to determine the importance of the two extra parameters, we have to verify which model describes better the particular data-set: The seven parameter model X with parameters $\vec{\theta}_X = \{\omega_1, \omega_2, \tau_1, \tau_2, A_{df}, A_{sus}, \delta_{21}\}$, or the five parameter model Y with parameters $\vec{\theta}_Y = \{\omega_1, \omega_2, A_{df}, A_{sus}, \delta_{21}\}$. While both models, X and Y, are capable of explaining the observations, we expect the simpler model Y to be more favourable from a RJMCMC output, since the extra parameters τ_1 and τ_2 are not significant for the data. The evolution of the Bayes factor for such an investigation for two different levels of SNR is shown in figure. 6.6.

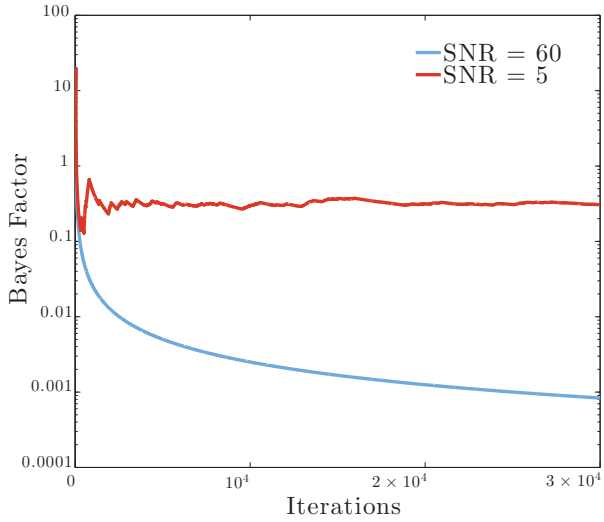

Figure 6.6: First 3×10^4 iteration of the RJMCMC output when comparing a seven and a five-dimensional LTP model (models X and Y respectively). Since the models are not competitive when the SNR = 60, the blue line tends asymptotically to zero. Credit: [6].

The results we obtain for all the approximations verify that the simpler model Y is much more probable than the more complicated model X. For the particular experiments proposed in [22] where the SNR is high, the Bayes factor computed tends to zero. In fact, for the case of the RJMCMC method, there is no single iteration "inside" the more complex model. This changes dramatically depending on the nature of the problem and, of course, as we show in section 6.4, on the SNR. In Table 6.3 we present only the low-SNR experiment, for the sake of comparison between the methods. Each method seems to favour the simpler model but they are not in total agreement between them. This is to be expected, as the SNR of this investigation is very low and the approximations of the evidence become more sensitive. For this particular case of the injections, the models are not competitive and therefore, the resulting estimated Bayes

Table 6.3: Results for the Guidance delay investigation with the low SNR experiment. See text for details.

Method	B_{XY}
RJMCMC	0.309
LF	0.124
LM	0.078
SBIC	0.768

Factor is extremely small. For a direct comparison, the RJMCMC algorithm requires more than 10^8-10^9 iterations.

Sticking to the one-dimensional case, it is also possible to examine interferometric cross-couplings between the injection channels for experiments. We shall examine another toy case of model selection, this time investigating the δ_{21} previously mentioned in chapter 4. The final aim is to explore whether we are able to discover cross-couplings by computing the Bayes factor between simpler and more complex models. The sensor matrix S in figure 6.5 (or eq. (4.8) from chapter 4) contains calibration factors of the interferometric readouts. We recall, that the off-diagonal terms represent the possible cross-talks contributions between the two measurements. In a simplified analytical form, and for the particular set of experiments that are defined with two injections and two readout channels (as in eq. (4.2)), the sensor matrix can be written as:

$$S = \begin{pmatrix} 1 & 0 \\ \delta_{21} & 1 \end{pmatrix}, \tag{6.21}$$

which is just a reformat of eq. 4.8, if we assume modelling in the displacement domain. The cross-term under investigation is the component δ_{21} in eq. (6.21). The LTPDA SSM simulator is again used to produce data for a double investigation. The first data-set is generated with a LTP that is is equipped with a "perfect" interferometer ($\delta_{21} = 0$), while for the second there is a cross-coupling between the two channels given by $\delta_{21} = 10^{-5}$. For both investigations we compare two models X and Y with $\vec{\theta}_X = \{\omega_1, \omega_2, A_{df}, A_{sus}, \delta_{21}\}$ and $\vec{\theta}_Y = \{\omega_1, \omega_2, A_{df}, A_{sus}\}$ respectively, or in other words, for both cases we try to recover the model with the dimensionality that supports the observations. The injection signals this time are in the form of single frequency sinusoidals with $f = 0.01$ Hz. This choice of simplified injections is justified by the fact that our aim is to demonstrate the performance of the algorithms and methods, and a multi-frequency signal yields to extremely large numerical values of the Bayes factor, making the comparison between the methods practically unfeasible with the RJMCMC algorithm. The results of this investigation are summarised in Table 6.4. In both cases we were able to obtain conclusive results for the cross-coupling of the system: for the first experiment, the Bayes Factor is below unity, thus favouring the simpler model Y which does not contain the parameter δ_{21}, while for the second experiment the favoured model is X, that can describe a LTP with $\delta_{21} > 0$. Indeed, this result shows possible application of this methodology during flight operations. The Bayes factor could be used to quantitatively discriminate competing interpretations of the data by the science team.

Table 6.4: Results for the two experiments of the interferometric cross-coupling investigation. For the first experiment the true value of the cross-coupling is $\delta_{21} = 0$, while for the second $\delta_{21} = 10^{-5}$.

	B_{XY}	
Method	Experiment 1	Experiment 2
RJMCMC	0.00036	35.1
LF	0.00032	35.3
LM	0.00032	35.7
SBIC	0.00016	37.1

After demonstrating the model selection procedure, we can now apply the techniques in more sophisticated problems. We recall that the dynamics in the acceleration domain of eq. (4.12), could be written in a simplified form as [6]

$$\alpha_{12} = \left[\frac{d^2}{dt^2} + \omega_2^2\right] x_{12} + (\omega_2^2 - \omega_1^2)x_1 - AF_2 + AF_1 \tag{6.22}$$

where we have considered only the differential acceleration α_{12}, and F_i is the real applied forces on the first and second test-masses. The true motion $\vec{x}$ of the TMs can be approximated by the delayed interferometer read-outs

$$\begin{aligned} x_1 &= o_1(t-\tau), \\ x_{12} &= o_{12}(t-\tau), \end{aligned} \tag{??}$$

As in chapter 4, section 4.2, the parameters appearing in eq. (6.22) and (4.13) are the stiffnesses of the two test-masses ω_1 and ω_2, the interferometer read-out delay τ, and the gains of the capacitance actuators A_{sus} (here represented as A for simplicity). Note that for this first approximation we have assumed identical actuators A for both test-masses. The commanded forces[4] g_1 and g_2 are available as telemetry, but the *real* applied forces on the three bodies are to be determined by the measurements and the analysis itself. For example, in the real data-stream there might be additional delays or even filtering of the applied forces coming from the controllers, so in reality a gain A might be proven to be frequency dependent: $A(f)$. This situation will appear in the received telemetry and we need the means to disentangle those two physical effects in a quantitative way.

For the particular simulated data-set, the model was not able to remove all the injected signals and even for the simple case of eq. (6.22), this led to a biased estimate for the parameters. Apart from a simple time delay on the commanded signals, there might be another process that causes a difference between the commanded g_1 and g_2 and the actual applied forces F_1 and F_2. For a first approximation of such a process, we assume a single real pole filter, filtering the time-series of the applied force on the second test-mass. For this investigation we can propose two models where $AF_i(t) = Ag_i(t-\tau_C)$ and $AF_i = A(\frac{f_o}{f-jf_o})g_i$ respectively. Here τ_C denotes the actuators time delay. In the end we can apply the model selection methods to these two models: the first one, X, where the applied forces are time delayed, and the second one, Y, where

4 Here the forces are normalised to the mass of the body that they are applied to.

the forces are frequency dependent (filtered by a single real pole filter). The calculated Bayes Factor between those two models is:

$$BF_{XY} = \frac{\pi_X(\vec{y})}{\pi_Y(\vec{y})} = 9.9478 \times 10^{-11}, \tag{6.23}$$

clearly indicating that the most probable process on the forces is the one described by model Y. The real pole was estimated to be $f_o = 1.963 \pm 0.001$ Hz and was confirmed for the complete set of system identification experiments in section 4.3.2. The estimated acceleration residuals for both models can be seen in figure 6.7.

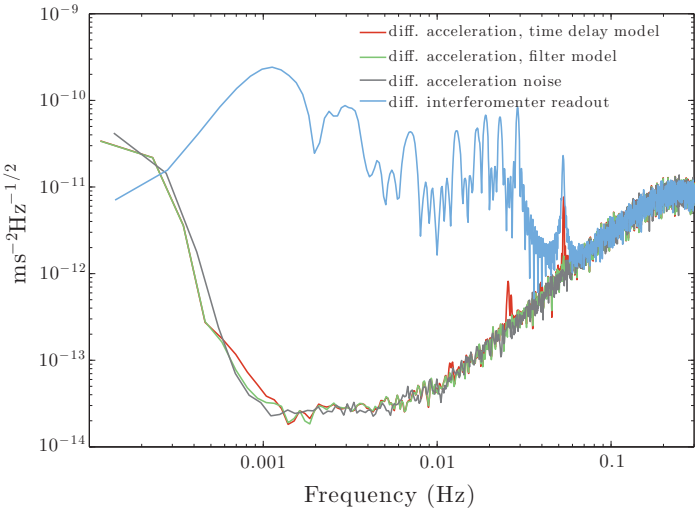

Figure 6.7: Power spectra of simulated differential acceleration between the two test-masses. The grey curve represents the reference noise measurement, while the light blue curve is the differential interferometer read-out. The value of the computed Bayes Factor can be confirmed with the comparison of the equivalent estimated residual acceleration for each model. The differential interferometer read-out is also plotted for comparison. Credit: [6].

The same analysis strategy applies of course to more complicated versions of the analytical models, where the number of parameter increases with the more terms of the equation are added, as happens in the following more realistic case. As already described in chapter 4, the two TMs are controlled with identical actuators. In reality, a small misbalance between the electrostatic actuators surrounding each test mass might be present. If we introduce this "asymmetry" to the system, immediately for the simple case of eq. (6.22), we can increase the dimensionality of the model by four parameters:

$$\begin{aligned} a_{12} = &\left[\frac{d^2}{dt^2} + \omega_2^2\right] x_{12} + (\omega_2^2 - \omega_1^2) x_1 \\ &- A_2\left(\frac{f_{o2}}{f - j f_{o2}}\right) g_2(t - \tau_{C2}) \\ &+ A_1\left(\frac{f_{o1}}{f - j f_{o1}}\right) g_1(t - \tau_{C1}). \end{aligned} \tag{6.24}$$

These parameters are gains, delays and filters that are different for the actuator of each test mass. Theoretically the highest in dimensions model of eq. (6.24) can describe the observations, but the problem to solve appears to be over-parametrized. A solution is to generate a set of nested models under the highest in dimensions of eq. (6.24) and apply the RJMCMC algorithm. The result of such a run is shown in figure 6.8 and it reveals the most favourable model and consequently the underlying procedure that describe best the physical system. For the particular simulation we can verify that the five-dimensional model is the best, concluding that no "asymmetry" in the hardware of the LTP is present. This changed in the following Data Challenge, where the Bayes factor between the simple model of eq. (6.22) and a six-parameter asymmetric one, is greater than 10^6, clearly supporting the correct higher dimension model where $A_1 \neq A_2$.

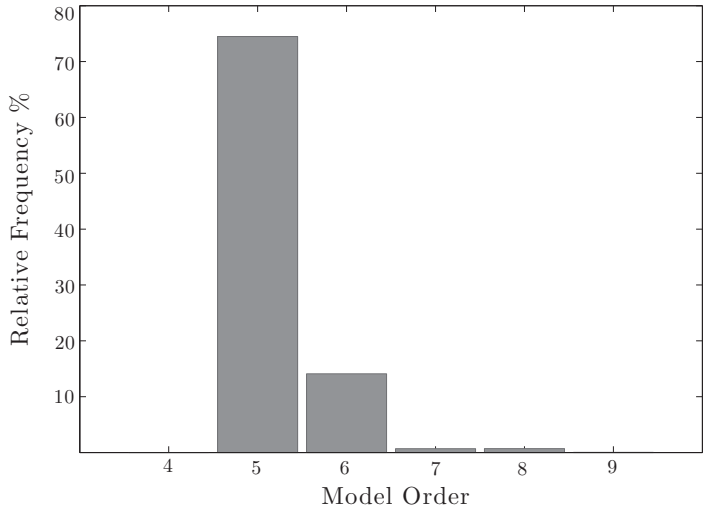

Figure 6.8: A RJMCMC run on a set of nested LTP models. There is a clear preference for the five-dimensional model for the given data-set. The data were produced with a "perfect" model where the two respective actuators were identical. Credit: [6].

6.3.2 *Model selection for the cross-talk experiments*

In the previous chapter, 5 devoted to the cross-talk experiments, we did a first base analysis on the simulated data-sets. We generated models that described the dynamics and managed to compute the residuals almost at the noise level that was measured a previous day of the experiments. By almost, we refer to the peak around 0.02 Hz of the spectrum residuals of figure 5.10, embedded here again for convenience.

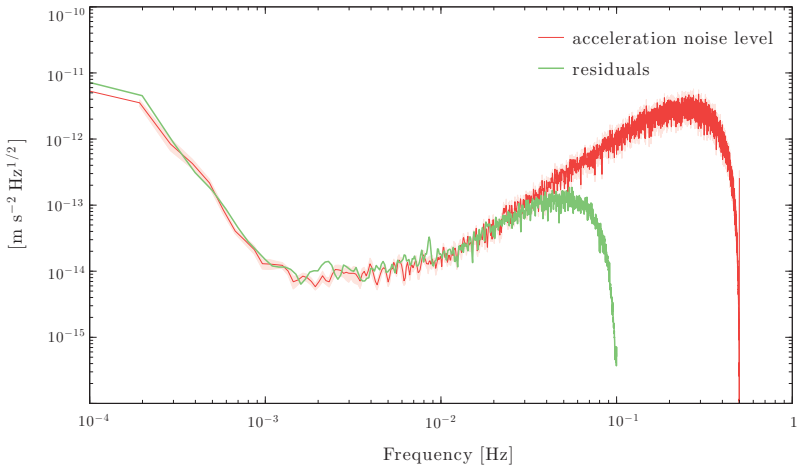

Figure 6.9: The calculated residuals for the complete cross-talk experiment data-stretch in comparison to the acceleration noise measured the first day of the simulation. The PSD of the residuals is comparable within the errors to the PSD of the noise, with the exception of a visible feature in the spectrum at around 8×10^{-3} Hz.

The feature of this spectrum indicates that the model of eq. (5.23) can be improved. Our first guess is that there is some cross-coupling coefficient not considered. This might originate from various sources, either some imperfection of the mechanical parts of the IS, or to the imperfectly aligned TMs on the centre of the IS at the moment of the experiment. By inspection of the telemetry time-series, we noticed that the controllers are actuating along the θ angle of the second test-mass (see figure 6.10). To be on the safe side, we will include the actuation over the η angle as well, and let the analysis decide the best approximation to the model.

Naturally, the model of the following equation used in the previous chapter

$$\begin{aligned}
\alpha_{12,model1} = &-\delta_{\ddot{\phi}_1}\ddot{\phi}_1 - \delta_{\phi_1}\phi_1 \\
&+ \delta_{\ddot{\phi}_1^2}\ddot{\phi}_1^2 + \delta_{N_{cmd,\phi_1}} N_{\phi_1}(t-\tau) \\
&+ \omega_2^2(o_1 - o_{12}) - \omega_1^2 o_1 + A_{sus} f_{cmd,x_2}(t-\tau) \\
&- \delta_{\ddot{\phi}_2}\ddot{\phi}_2 - \delta_{\phi_2}\phi_2 + \delta_{\ddot{\phi}_1^2}\ddot{\phi}_2^2 + \delta_{N_{cmd,\phi 2}} N_{\phi_2}(t-\tau) \\
&- \delta_{\ddot{y}_1}\ddot{y}_1(t-\tau) - \delta_{y_1} y_1(t-\tau) - \delta_{\ddot{y}_2}\ddot{y}_2(t-\tau) - \delta_{y_2} y_2(t-\tau),
\end{aligned} \tag{5.23}$$

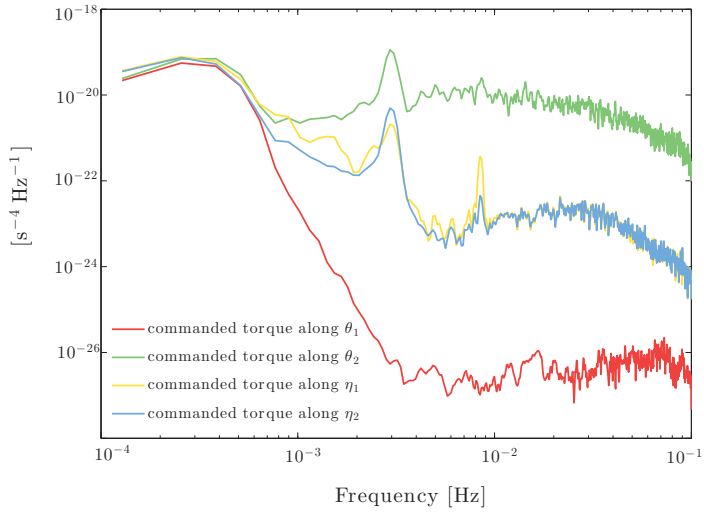

Figure 6.10: The actuation along θ during the cross-talk experiments.

becomes

$$\begin{aligned} a_{12,model2} = &- \delta_{\ddot{\phi}_1}\ddot{\phi}_1 - \delta_{\phi_1}\phi_1 + \delta_{\ddot{\phi}_1^2}\ddot{\phi}_1^2 \\ &+ \delta_{\Delta N\phi}\left(N_{cmd,\phi_1}(t-\tau) - N_{cmd,\phi_2}(t-\tau)\right) \\ &- \delta_{\ddot{\phi}_2}\ddot{\phi}_2 - \delta_{\phi_2}\phi_2 + \delta_{\ddot{\phi}_2^2}\ddot{\phi}_2^2 \\ &- \delta_{\ddot{y}_1}\ddot{y}_1 - \delta_{y_1}y_1 - \delta_{\ddot{y}_2}\ddot{y}_2 - \delta_{y_2}y_2. \\ &+ \delta_{\Delta N\theta}\left(N_{cmd,\theta_1}(t-\tau) - N_{cmd,\theta_2}(t-\tau)\right) \\ &+ \delta_{\Delta N\eta}\left(N_{cmd,\eta_1}(t-\tau) - N_{cmd,\eta_2}(t-\tau)\right) \\ &- \omega_2^2(o_{12}+o_1) + \omega_1^2 o_1 + A_{sus}f_{cmd,x_2}(t-\tau). \end{aligned} \tag{6.25}$$

In eq. (6.25), we have introduced a couple of tricks to reduce the dimensionality of the model. In (5.23) we estimate the imperfection of the commanded torques along the ϕ angles, as $\delta_{N_{cmd,\phi_1}} N_{\phi_1}(t-\tau)$ and $\delta_{N_{cmd,\phi 2}} N_{\phi_2}(t-\tau)$. Instead, we included the $\delta_{\Delta N\phi}$, $\delta_{\Delta N\theta}$, and $\delta_{\Delta N\eta}$ parameters that correspond to the difference of the cross-coupling coefficients. This allows us to reduce the problem dimensions and also avoid ill-conditioned covariance matrices. While it was expected that commanded torques around η and ϕ would leak through cross-talk mechanisms in the differential interferometer readings, the commanded torques along θ would appear through the y_1 and y_2 electrodes if the TMs were not perfectly positioned in the geometrical centre of the IS.

With this at hand we fed the two competing models into the RJMCMC machinery. The priors were defined as Gaussian distributions centered around our first guess of the parameter values, with very large spread, since our knowledge of the cross-coupling terms is very limited before fitting. After 10^6 iterations, the RJMCMC chains were not converging to a single value, and iterating mostly inside model Y, indicating that model Y is a better model for the particular data-set. For this case where there is a clear

Parameter	Initial guess value	Estimated $\pm\sigma$
$\delta_{\ddot{\phi}_1}$	50×10^{-6}	$(1.369 \pm 0.001) \times 10^{-4}$
δ_{ϕ_1}	5×10^{-10}	$(-6.8 \pm 0.2) \times 10^{-10}$
$\delta_{\ddot{\phi}_1^2}$	0.19	$-0.190369 \pm 2 \times 10^{-6}$
$\delta_{\Delta N\phi}$	10^{-7}	$(-4.4 \pm 0.7) \times 10^{-7}$
ω_2^2	-2×10^{-6}	$-(2.2 \pm 0.1) \times 10^{-6}$
ω_1^2	-2×10^{-6}	$-(2.0 \pm 0.3) \times 10^{-6}$
τ	0.4	0.455 ± 0.002
$\delta_{\ddot{\phi}_2}$	0.19	$-(1.290 \pm 0.001) \times 10^{-4}$
δ_{ϕ_2}	-5×10^{-7}	$-(5.2 \pm 0.2) \times 10^{-10}$
$\delta_{\ddot{\phi}_2^2}$	0.1	-0.2303 ± 10^{-4}
$\delta_{\ddot{y}_1}$	10^{-4}	$-(1.0 \pm 0.5) \times 10^{-5}$
δ_{y_1}	10^{-4}	$-(1.32 \pm 0.01) \times 10^{-7}$
$\delta_{\ddot{y}_2}$	5×10^{-5}	$(1.6 \pm 1.5) \times 10^{-5}$
δ_{y_2}	10^{-4}	$-(1.23 \pm 0.1) \times 10^{-7}$
$\delta_{\Delta N\theta}$	10^{-6}	$-(7.8 \pm 0.6) \times 10^{-5}$
$\delta_{\Delta N\eta}$	10^{-6}	$-(0.5 \pm 0.7) \times 10^{-5}$
$\delta_{\Delta f_{y,cmd}}$	10^{-4}	-0.0010 ± 0.0005

Table 6.5: Estimated parameters of the best case model decided from the model selection procedure.

preference for a model, we can use the LM estimator of the marginal likelihood. The logarithm of the Bayes factor is then estimated as

$$\log BF_{12} = \log\left(\frac{\pi_X(\vec{y})}{\pi_Y(\vec{y})}\right) = -85.0, \tag{6.26}$$

where we have named *model 1* the first approximation to the model, and *model 2* the improved version discussed here in eq (6.25). From this result, it is safe to conclude that we have to take into account the cross-coupling originating from the rotation along the θ angles of both TMs. This can be more obvious from figure 6.11, where the residuals now do not show any peak features, and they are comparable to the acceleration noise levels.

A MCMC estimation over the most probable model will result to the parameter estimates of table 6.5, and figure 6.13, that shows the sampled covariance matrix of the parameters.

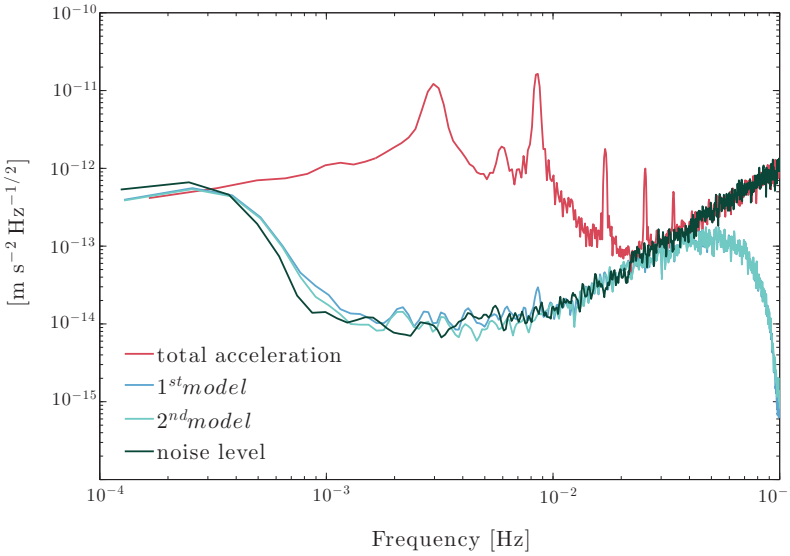

Figure 6.11: The residuals of the different models in comparison with the acceleration noise level. See text for details.

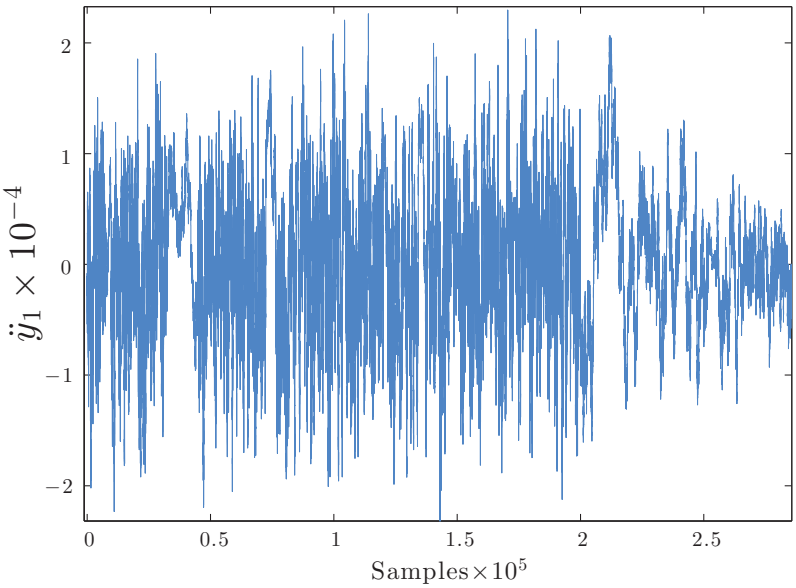

Figure 6.12: A chain of the $\ddot{y}_1$ parameter, taken from a RJMCMC run. The sampling of different parameter spaces is visible from the trace plot of the chain.

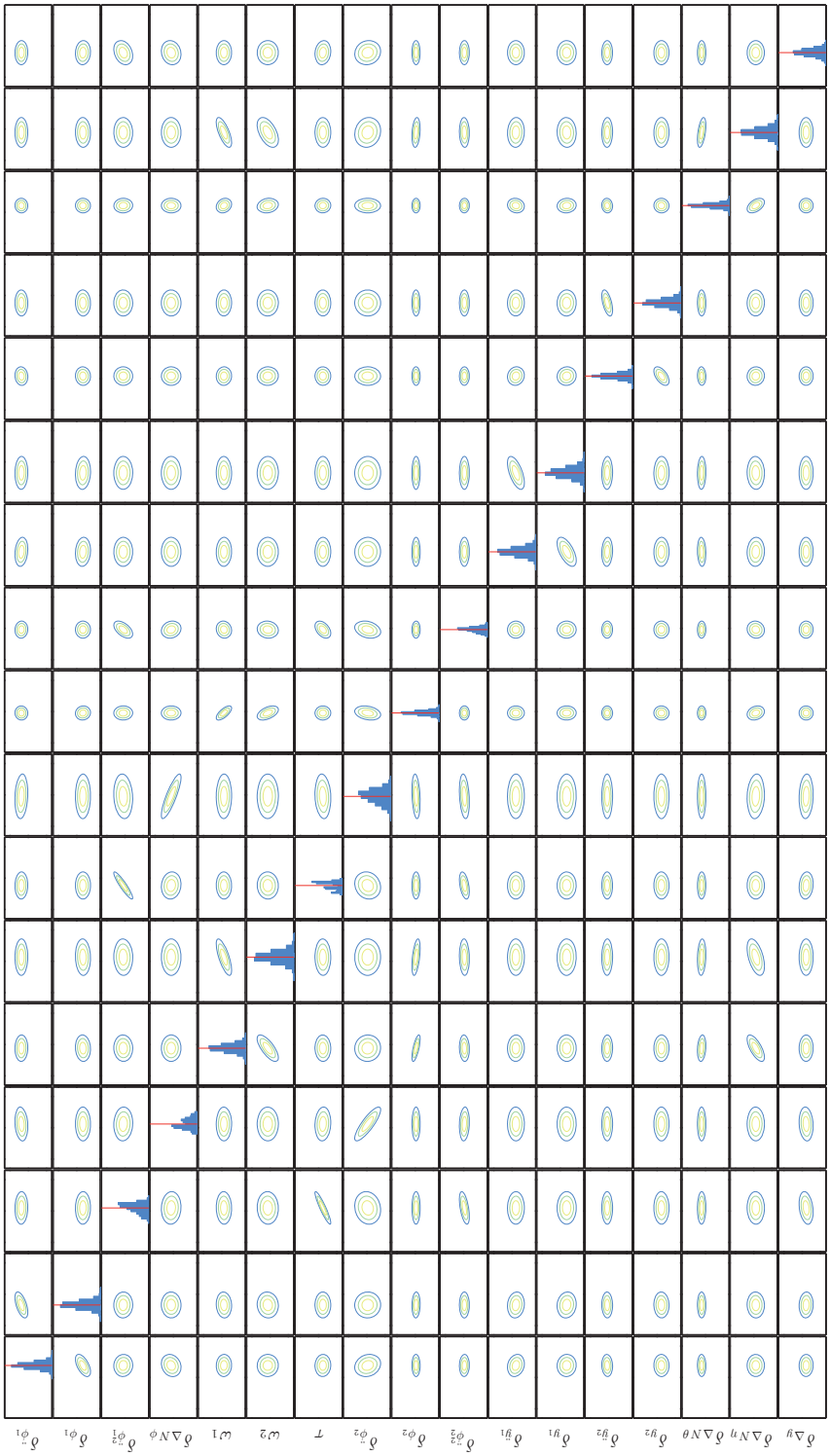

Figure 6.13: The covariance matrix as sampled with the MCMC algorithm for the best car model of the cross-talk analysis.

6.4 ASSOCIATION WITH THE EXPERIMENT DESIGN

In this last section we explore the capability of the implemented model selection framework, not only as a set of tools for data analysis purposes, but also as a way to evaluate the efficiency of the experiments we are planning to run in the satellite. As we are going to show, by comparing different models under different input signal conditions, we can safely determine the best range of parameters that define our experiments, or verify the injection frequencies that maximise the information extracted from the system.

It has been shown [7, 25] that there is a dependence of the Bayes Factor output on the SNR regime of the investigations. This, of course, holds true in the case of the LTP as it can be seen in figure. 6.14. This figure was created by simulating the guidance injections LTP experiments for each value of the SNR, while the injection signals were single frequency ($f = 0.01\text{Hz}$) sinusoidal inputs into the system. The LTP models under comparison were quite similar versions of SSMs, with the exception of a different realisation of the response model of the thrusters. We made this choice of similar models and single injection frequencies, to produce more intelligible results, because the large amplitude planned injections result to very large values of the Bayes factor. It is clear that above the critical value of the SNR $= 21$ the results obtained with the different techniques are consistent and in good agreement. Below that value of the SNR we cannot make clear decisions about the competing models, as the wrong model is showing preference, or we poorly approximate the Bayes Factor.

Although this SNR limit varies, as expected, depending on the type of investigation and model, the current result is already providing an estimation of the required power of the injection signals that we need to consider in the LTP experiment. This information and the method used here will be of particular interest for the design of in-flight experiments for the LPF mission.

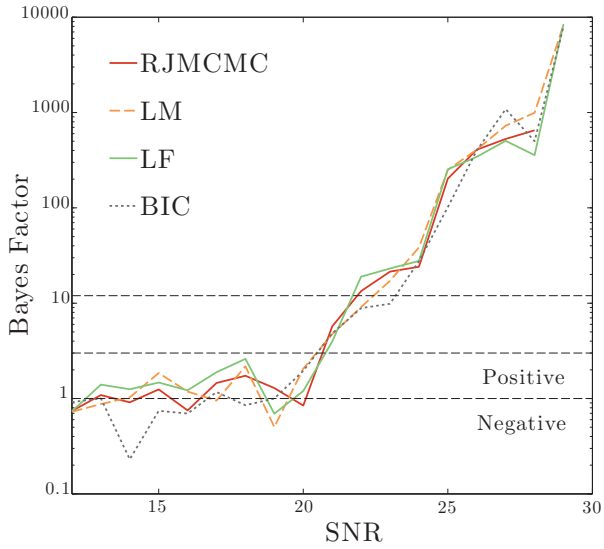

Figure 6.14: The Bayes Factor as a function of SNR computed using different methods.

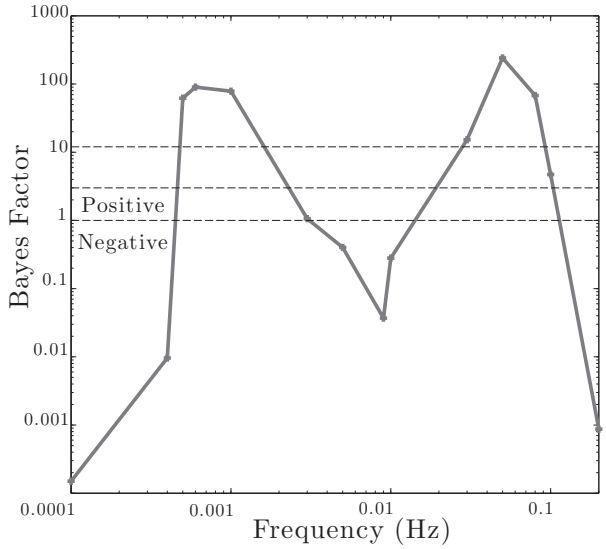

Figure 6.15: The Bayes Factor as a function of the injection frequencies in the first interferometric channel. The computed evidence of model X is stronger when the sinusoidal injection signals have a frequencies around $f_{i_{x_1}} \simeq 0.0006$ Hz and $f_{i_{x_1}} \simeq 0.05$ Hz respectively.

Furthermore, for system identification experiments, as in the case of the LTP, the computed evidence of a model depends on the design of the experiment itself. The information obtained from the system differs depending on the injection frequencies. An interesting study is to explore in detail this relation. A four- (X) and a five-dimensional (Y) models are examined, given different injection frequencies. More precisely, since the difference between the models is the cross-coupling δ_{21} as shown in figure 6.5, which describes the signal leakage from the first to the differential interferometric channel, we examine the Bayes Factor given different injection frequencies to the first channel, while keeping constant the injection to the differential channel ($f_{i_{x12}} = 0.2$ Hz). The SNR of this experiment is kept at the "low" value of 28.

The data generation model is mounted with a "perfect" interferometer ($\delta_{21} = 0$) and model X is the same as the one used to produce the data, while model Y is the one with the extra parameter δ_{21}. The expected outcome of this exploration is that if the system is more sensitive to the δ_{21} parameter at some particular frequencies, we must detect an increase in the Bayes Factor which underlines a more clear decision towards the correct model.

In figure 6.15 we can see the corresponding Bayes Factor versus the injected frequencies to the first channel. Given the low SNR of the investigation, while model X should be more favourable, a preference for the more complex model Y is shown for a certain set of frequencies. This result is a clear indicator of the set of preferred frequencies that can be injected to the system for its characterisation given the current configuration and SNR. Indeed, injections around $f \simeq 0.0006$ Hz and $f \simeq 0.05$ Hz promote the identification of the correct model, while injections at both the high and low frequency limit, together with $f \simeq 0.01$ Hz, may induce the analysis into an error. This frequency de-

pendence must be associated to the sensitivity of the experiment to a given parameter, the parameter δ_{21} in this particular case. This observed dependency, when considering a more realistic model, will be of particular interest in the selection of injection signals for the experiments to be run in-flight.

Discussion

We have implemented three different methods to compare competing models of the LTP experiment on-board the LPF mission: The RJMCMC algorithm, the Laplace approximations, and the Bayes Information Criterion. The results from each method seem to be in agreement, but the output strongly depends on the expected SNR and of course on the models under investigation. Considering the LPF mission planned experiments, the SNR is high enough to safely use any of all the available techniques, but probably the most computationally demanding methods will be used for off-line analysis to confirm our first computations.

The RJMCMC algorithm (together with the Laplace methods and the Bayes Information Criterion) employed in this work has been integrated in the LTPDA toolbox as part of the LPF data analysis software. The RJMCMC algorithm is by far the most computationally costly, but at the same time it is the more suitable one when we compare more than two nested models or we work with inputs with low SNR. The Laplace-Metropolis and the Laplace-Fisher methods are reliable when we work in the high SNR regime, but they also require significant computing time, specially when one has to use outlier detection methods to estimate the weighted covariance matrix. On the other hand, the Laplace-Fisher approximation is limited by the use of the Fisher Information Matrix, which for the case of LTP SSMs is computed numerically.

Moreover, an attempt to associate the output of the aforementioned methods with the actual system identification experiment has been made. We have used different experiment setups to demonstrate that the Bayes Factor depends not only on the SNR, but also on the injection frequencies to the system.

The developed algorithms were successfully applied to model selection problems for the LPF data analysis. Different cases of LTP model selection problems have been investigated over data-sets that were produced by both the LTPDA and the ESA OSE simulator. For the first case, we have considered an easy case of five- and seven-dimensional state-space models, where the importance of the extra two parameters was examined. These two extra parameters are time delays caused by the LPF hardware and they can be characterised as essential parameters of the model. For the second case, we examined if we are able to recover the dimensionality of the correct model used for the generation of the data, by examining the interferometer cross-coupling coefficient.

Then, we explored the most suitable dimensionality of analytic models. There, the simplest model that described efficiently the observations was recovered, excluding the more complicated ones that caused over-fitting issues. Finally, we applied the developed techniques to the more complicated cross-talk experiments, were the dimensionality of the models can be much higher. From data-sets generated with the OSE simulator, we discovered cross-coupling effects originating from a DOF not taken into account in section 5.4. This type of analysis is expected to be performed during operations due to the broad spectrum of possible applications, like identifying external disturbances that result into forces applied to the three-body system.

[1] Juan Pedro Lópes Zaragoza. Magnetic fields analysis in the LISA PathFinder mission. Master's thesis. 123

[2] David J. C. MacKay. *Information Theory, Inference, and Learning Algorithms*. Cambridge University Press, 2003. 124

[3] Everything should be made as simple as possible, but not simpler, Albert Einstein? Louis Zukofsky? Roger Sessions? William of Ockham? Anonymous? http://quoteinvestigator.com/2011/05/13/einstein-simple/. Accessed: 03-10-2014. 124

[4] P J Green. Reversible jump Markov chain Monte Carlo computation and Bayesian model determination. *Biometrica*, (82):711–32, 1995. 125, 126

[5] Robert Kass and Adrian Raferty. Bayes factors. *Journal of American Statistical Assosiation*, 90(430), 1995. 125, 126, 129

[6] Nikolaos Karnesis, Miquel Nofrarias, Carlos F. Sopuerta, et al. Bayesian model selection for LISA pathfinder. *Phys. Rev. D*, 89:062001, Mar 2014. URL: http://link.aps.org/doi/10.1103/PhysRevD.89.062001, doi:10.1103/PhysRevD.89.062001. 125, 127, 129, 131, 132, 134, 135, 136

[7] N Cornish and T Littenberg. Tests of Bayesian model selection techniques for gravitational wave astronomy. *Physical Review D*, 76(8):1–11, October 2007. URL: http://link.aps.org/doi/10.1103/PhysRevD.76.083006, doi:10.1103/PhysRevD.76.083006. 126, 128, 129, 142

[8] Michele Vallisneri. Use and abuse of the Fisher information matrix in the assessment of gravitational-wave parameter-estimation prospects. *Physical Review D*, 77(4):1–20, February 2008. URL: http://link.aps.org/doi/10.1103/PhysRevD.77.042001, doi:10.1103/PhysRevD.77.042001. 126

[9] Peter J. Rousseeuw and M. Leroy Annick. *Robust Regression and outlier detection*. john Wiley and Sons, 1987. 126, 128

[10] Hedibert Freitas Lopes and Mike West. Bayesian model assessment in factor analysis. *Statistica Sinica*, 14:41–67, 2004. 126

[11] P Dellaportas, J J Forster, and I Ntzoufras. On Bayesian model and variable selection using MCMC. *Statistics and Computing*, pages 27–36, 2002. 126

[12] Alexander Stroeer and John Veitch. Bayesian approach to the study of white dwarf binaries in lisa data: The application of a reversible jump markov chain monte carlo method. *Phys. Rev. D*, 80:064032, Sep 2009. URL: http://link.aps.org/doi/10.1103/PhysRevD.80.064032, doi:10.1103/PhysRevD.80.064032. 126

[13] Richard Umstätter, Nelson Christensen, Martin Hendry, et al. Bayesian modeling of source confusion in lisa data. *Phys. Rev. D*, 72:022001, Jul 2005. URL: http://link.aps.org/doi/10.1103/PhysRevD.72.022001, doi:10.1103/PhysRevD.72.022001. 126

[14] Simon J. Godsill. On the relationship between markov chain monte carlo methods for model uncertainty. *Journal of Computational and Graphical Statistics*, 10:230–248, 2001. 127

[15] N Karnesis. Model selection for LISA Pathfinder. Technical Report S2-IEC-TN-3094, 2012. 127

[16] Tyson B. Littenberg and Neil J. Cornish. Bayesian approach to the detection problem in gravitational wave astronomy. *Phys. Rev. D*, 80:063007, Sep 2009. URL: http://link.aps.org/doi/10.1103/PhysRevD.80.063007, doi:10.1103/PhysRevD.80.063007. 127

[17] B. Calderhead and M. Girolami. Estimating bayes factors via thermodynamic integration and population mcmc. *Computational Statistics and Data Analysis*, 53(12):4028–4045, October 2009. URL: http://eprints.gla.ac.uk/34589/. 127

[18] J. Skilling. Nested sampling for general Bayesian computation. *Bayesian Analysis*, 1(4):833–860, 2006. 127

[19] Pia Mukherjee, David Parkinson, and Andrew R. Liddle. A nested sampling algorithm for cosmological model selection. *Astrophys.J.*, 638:L51–L54, 2006. arXiv:astro-ph/0508461, doi:10.1086/501068. 127

[20] W.R. Gilks, S. Richardson, and D. Spiegelhalter. *Markov Chain Monte Carlo in Practice*. Chapman & Hall/CRC Interdisciplinary Statistics. Taylor & Francis, 1995. URL: http://books.google.gr/books?id=TRXrMWY_i2IC. 128

[21] Sir Harold Jeffreys. *Theory of Probability*. Oxford, 3 edition, 1961. 128

[22] S Vitale. Measurement of LTP dynamical coefficients by system identification. Technical Report S2-UTN-TN-3045, 2007. 131, 132

[23] M. Nofrarias, L. Ferraioli, G. Congedo, et al. Parameter estimation in LISA Pathfinder operational exercises. *J.Phys.Conf.Ser.*, 363:012053, 2012. arXiv:1111.4916, doi:10.1088/1742-6596/363/1/012053. 131

[24] M Nofrarias, L Ferraioli, and G Congedo. Comparison of parameter estimates results in STOC Exercise 6. Technical Report S2-AEI-TN-3070, 2011. 131

[25] J Veitch and A Vecchio. A Bayesian approach to the follow-up of candidate gravitational wave signals. pages 1–10, 2008. arXiv:arXiv:0801.4313v3. 142

7 CONCLUSIONS

The LISA Pathfinder (LPF), is a technology demonstrator mission, that is pioneering the field of Gravitational-Waves (GW) detection in space. It will pave the way for GW detectors operating with the same principles as eLISA. The eLISA concept consists of three SCs forming a triangle with arm lengths of 10^6 km. The mother SC, hosts two TMs, while the two daughter SCs one. The distances between the TMs will be constantly monitored via laser interferometers, in order to discover oscillations in these distances, that signify propagation of GWs. But these oscillations will have to be disentangled out of the dynamics of the local system. This problem is going to be investigated by LPF, since one of its main goals is to characterise the joint dynamics of TMs and SC and construct an accurate noise model to be directly inherited by eLISA.

The LPF is in essence, a single arm of the eLISA squeezed down from one million km to 30 cm. It will prove geodesic motion between two TMs by monitoring their relative distance with laser interferometers. The in-flight operations will consist of a sequence of experiments to characterise different aspects of the instrument. One of them will be the system identification experiments, that can be divided into two categories. The first category of experiments is performed over the sensitive x-axis, which is defined by the line joining the two TMs. The TMs and SC are set in motion along x, while their position is being recorded. In the second category, the three bodies are commanded along different DOF in order to determine the cross-coupling effects and estimate the signal leakage on the differential interferometer channel.

The analysis of the aforementioned experiments can be challenging, due to several factors. The first one being the dimensionality of the models, that can be very high, and the second one is the unknown effects that might be contributing to the overall measured acceleration. For that reason, we have developed a Bayesian analysis framework to tackle the non-linearity and the high dimensionality of the models. The Bayesian framework allows us to use prior densities for the parameters, a feature very relevant to the LTP. This because the level of the knowledge of the system is constantly being updated, not only by the analysis if the system identification experiments, but also from others, like the TM charging measurements, or the drift mode. The results from each experiment can then be integrated as prior knowledge in the analysis.

As a tool, we have developed a Markov Chain Monte Carlo (MCMC) algorithm, that is proven to able to sample efficiently the parameter space. The MCMC scheme was developed based on the work of [1], and was further enhanced and evolved into robust DA tool to be used during operations. The developed MCMC method is fulfilling the requirements for a fitting algorithm to be integrated to the dedicated data analysis toolbox (LTPDA). In particular, the deployed algorithm comes with the necessary help for the user, while keeping the analysis history. Furthermore, at the end of each run, diagnostics on the chains are being conducted for more robust statistical results (see section 3.4). The fitting algorithm was then integrated to a pipeline analysis framework to be used for on-line analysis during operations. The pipeline consists of pre-defined analysis steps, the first one being the data acquisition from repositories. Then given investigation is defined, and the data are pre-processed to be finally fed into the MCMC

machinery. The results, together with the produced figures are then uploaded to dedicated analysis repositories automatically.

The robustness of the aforementioned pipeline, has been demonstrated in the training simulations over the last three years, where the different modelling techniques were put to test (see chapter 4). More specifically we analysed data-sets generated for the 2^{nd}, 3^{rd} and 4^{th} STOC simulations. The x-axis system identification experiments simulated are defined in [2], and are split in to two main categories; the interferometer injection signals, were the controllers respond to fake displacements of the TMs, and the application of open-loop forces on both TMs and SC. Different LTP modelling approximations were considered for the analysis, but in the end, the analytical models in the acceleration domain were proven to be the more reliable ones. This was justified by the fact that modelling in the displacement domain requires near-perfect knowledge of the controllers transfer functions, whereas in the acceleration domain, the controllers vanish from the equations. The free parameters $\vec{\theta}$ to be estimated, in all simulation cases cases were very close to the true values of the simulator within their expected error.

The cross-talk experiments were analysed for the first time during the 4^{th} training simulation (see chapter 5). The underlying dynamical model was formed in the acceleration domain, and each injection into various DOF was analysed separately[1]. After successfully recovering a reliable model for each injection investigation, we joined all the models to attempt to fit the complete data-stretch of the cross-talk experiments. The result at a first approximation is quite satisfying, because it revealed that possible cross-coupling mechanisms that were not taken into account at the first place, might be causing signal leakage into the differential acceleration measured. This was further studied in chapter 6, where we perform model selection techniques to the particular data-set. There, the cause of the signal excess was identified and quantitatively assessed. A more suitable model was then used to estimate the parameters of the system and estimate residuals equivalent to the noise level.

In addition, we implemented different approximations to the treatment of the curve of the PSD of the acceleration noise. The acceleration noise level is nominally estimated from the frequent quiet measurements of the instrument. But its level is not constant with time, and one has to make assumptions on the level of knowledge over this curve. We can assume that the changes of the noise are negligible from the time of its measurement to the time of the experiment we analyse, and use the χ^2 likelihood function of eq. (3.25), were the PSD curve is considered known. The relaxed assumption that the noise might have changed slightly, leads to a likelihood function of eq. (4.24), where the noise level is parametrised with a set of η coefficients [3], to be estimated along with the dynamical parameters. Both approaches were tested with the guidance injection system identification experiments yielding equivalent results, with negligible smaller variance for the second approximation (see figure 4.21). The insignificant differences of the two approaches was expected, due to the high SNR nature of the experiments. The final approach was the one of [4], where the DFT coefficients of the noise (after assuming zero-mean and Gaussian properties), are marginalised out of the posterior distribution to form the final equation (4.30). All of the techniques were implemented for LTPDA and tested with a three-parameter toy model investigation (see sub-section 4.4). A Monte Carlo study with different realisations of the data-set, proved that for

1 We recall that the TMs and SC were commanded to oscillate along ϕ_1, ϕ_2, y_1, y_2, and Φ.

this simple case, the different methods agree within their respective errors.

The nature of the system identification experiments, suggests that during operations, model selection problems may appear. For example, the high dimensionality of the cross-talk models, in combination with physical effects contributing in low SNR verified that we needed model selection routines and protocols in the toolbox. For that reason, we have implemented a Reversible Jump Markov Chain Monte Carlo (RJMCMC) algorithm, which can be seen as a generalised version of a standard MCMC method (see chapter 6). The RJMCMC automatically penalises higher dimensional models by embodying the Occams' Razor in the process. Furthermore, additional approximations to the marginal likelihood were employed; the Laplace-Metropolis (LM) and the Laplace-Fisher (LF) approximations. They differ on the way the Hessian matrix of the posterior distribution is computed. The LF uses a Gaussian approximation and takes the inverse of the FIM, while the LM takes the covariance matrix as sampled from a MCMC simulation over the posterior. When using the LM criterion, one must carefully compute the covariance matrix with a high breakdown point robust estimator [5]. The Minimum Volume Ellipsoid (MVE) outlier detection method was chosen [6], and adapted into the LTPDA toolbox. Finally, the Schwarz-Bayes Information Criterion (SBIC) was also considered as an alternative to the logarithm of the Bayes factor .

The above techniques were applied to the x-axis experiments [7], first to toy models, and then to more realistic applications, where we were able to recover the correct model for all the simulated data-sets. The dependence of the Bayes factor to the SNR and possible links to the design of the experiment itself was also shown. The RJMCMC was also applied to the cross-talk experiments analysis, with the aim to improve the results from chapter 5, where there were hinds that there might be physical effects not taken into account in the model of the dynamics. The cross-coupling of the η DOF was proven to be causing the peak issues in the acceleration residuals, and the corresponding model was proven to be more preferable than the one used in chapter 5. It is worth to mention that the RJMCMC was also applied to the magnetic diagnostics analysis for the LTP [8]. In this study, the possibility of detecting the various sources of the magnetic filed in the SC was explored. The RJMCMC algorithm was then used to select the most probable number of sources and their location around the LTP.

Future work includes the further enhancement of the analysis pipeline, and implement various improvements to our MCMC parameter estimation algorithm. Among the tasks of the team is also to establish a fitting protocol procedure for online operations. This means that for every experiment performed during flight, a protocol of the minimum actions, and the preferred technique and fitting tool have to be defined. To achieve this, one has to take into account the number of data points, the sampling frequency, the model dimensionality, and make assumptions about the noise levels. An outcome of this study will be several technical documents with theoretical justifications for each experiments, but also small handbook documents describing these procedures in a brief manner. More advanced methods of sampling the posterior distribution have also been considered, like for example the Nested Sampling family of algorithms [9]. Such a method will allow more robust searches on the surface of the posterior distribution for the case of the more complicated problems.

[1] M. Nofrarias, C. Röver, M. Hewitson, et al. Bayesian parameter estimation in the second LISA Pathfinder mock data challenge. *Physical Review D*, 82(12):1–14, December 2010. URL: http://link.aps.org/doi/10.1103/PhysRevD.82.122002, doi:10.1103/PhysRevD.82.122002. 149

[2] S Vitale. Measurement of LTP dynamical coefficients by system identification. Technical Report S2-UTN-TN-3045, 2007. 150

[3] Tyson B. Littenberg and Neil J. Cornish. Bayesian approach to the detection problem in gravitational wave astronomy. *Phys. Rev. D*, 80:063007, Sep 2009. URL: http://link.aps.org/doi/10.1103/PhysRevD.80.063007, doi:10.1103/PhysRevD.80.063007. 150

[4] Stefano Vitale, Giuseppe Congedo, Rita Dolesi, et al. Data series subtraction with unknown and unmodeled background noise. *Phys. Rev. D*, 90:042003, Aug 2014. URL: http://link.aps.org/doi/10.1103/PhysRevD.90.042003, doi:10.1103/PhysRevD.90.042003. 150

[5] Robert Kass and Adrian Raferty. Bayes factors. *Journal of American Statistical Assosiation*, 90(430), 1995. 151

[6] Peter J. Rousseeuw and M. Leroy Annick. *Robust Regression and outlier detection*. john Wiley and Sons, 1987. 151

[7] Nikolaos Karnesis, Miquel Nofrarias, Carlos F. Sopuerta, et al. Bayesian model selection for lisa pathfinder. *Phys. Rev. D*, 89:062001, Mar 2014. URL: http://link.aps.org/doi/10.1103/PhysRevD.89.062001, doi:10.1103/PhysRevD.89.062001. 151

[8] Juan Pedro Lópes Zaragoza. Magnetic fields analysis in the LISA PathFinder mission. Master's thesis. 151

[9] John Skilling. Nested sampling. *AIP Conference Proceedings*, 735(1), 2004. 151

Part III

APPENDIX

A

MCMC ALGORITHM CLASS

In this first part of the appendix, the MCMC algorithm class developed for the LTPDA isa going to be explained. The class was developed by taking into account all the requirements for the parameter estimation needs for LPF [1], and a technical report was generated that describes the technical aspects of the algorithm [2]. In particular, a parameter estimation algorithm must show a minimum of requirements, to be characterised as suitable and be integrated into the LTPDA toolbox:

- The history of the analysis must be stored in the resulting `pest` object[1].
- The results must be reproducible. Directly associated with the previous point, each member of the DA team should be able to reproduce the analysis only with the final product at hand.
- The code must be accompanied with the necessary comments and `HTML` help, for the convenience of the user.
- A parameter estimation algorithm should be applicable to any kind of fitting problems linked with the LPF experiments.

The new design of the MCMC class was fulfilling the above prerequisites after the introduction of new elements, and the re-organisation of the code. Figure A.1 shows the data flow diagram of the MCMC class, each of its modules is explained bellow.

- `MCMC.preprocess`: This is the first block of data handling. The time-series are split into the desirable time spans, and later resampled, if necessary. The input model is also pre-processed here[2], depending on its format. Then, they are transferred to the frequency domain, to be passed to the function that defines the likelihood. The `MCMC.buildLogLikelihood` function builds the given likelihood, depending on the inputs from the user. All of the discussed formats explained in sections 3.2 and 4.4, can be generated here. Finally, the expected covariance matrix of the parameters is estimated through the `<class>/fisher` function.
- `MCMC.simplex`: A non-linear minimisation of the likelihood can be performed before sampling with the MH algorithm, to get to a better starting point. The method used, is the one of [3].
- `MCMC.mhsample`: The sampling of the parameter space is performed. The likelihood is calculated at each step, with the MH described in section 3.4. At the end of the sampling, the statistics of the MCMC chains are computed and stored in the output.

1 A `pest` object is an LTPDA instance, where the results of the parameter estimation procedures are stored.
2 The MCMC class accepts `matrix`, `ssm`, or `mfh` type of models.

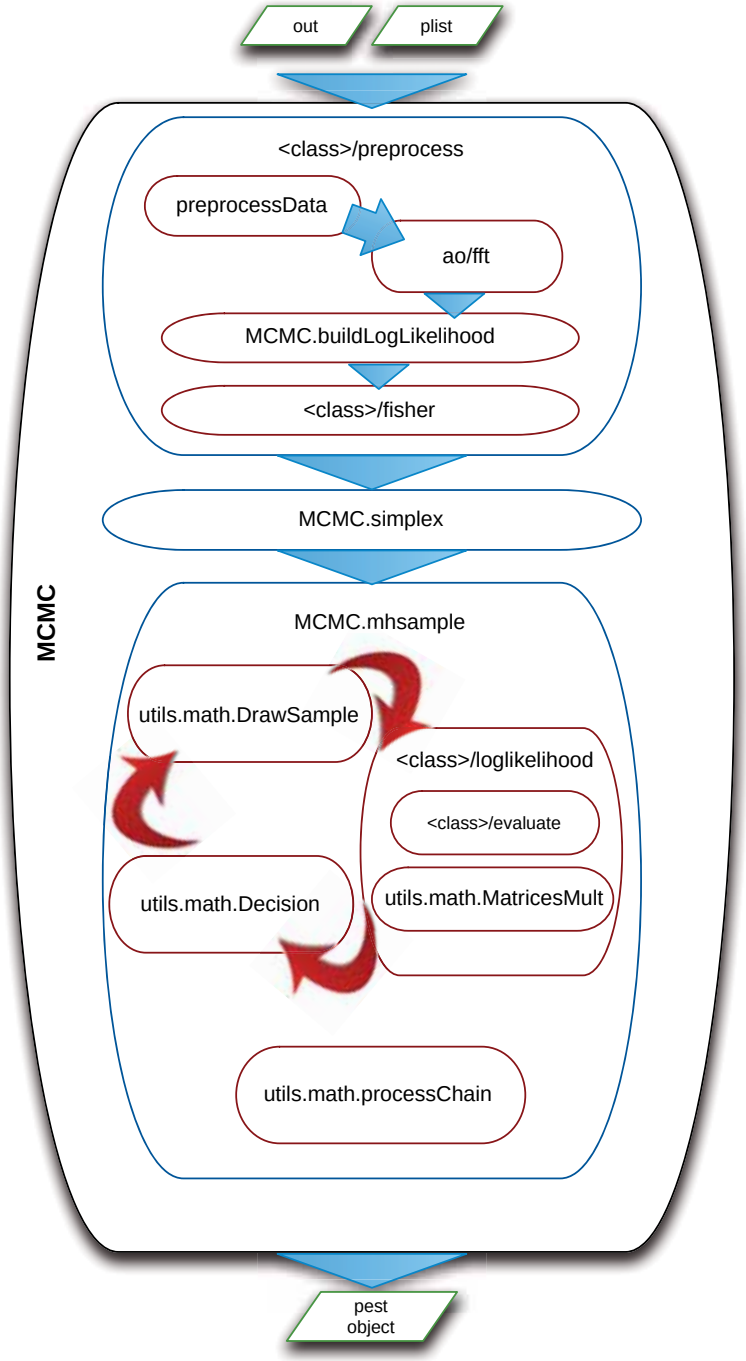

Figure A.1: The MCMC class flow diagram. See text for details. Credit: [2]

Figure A.2: `Git` history tree. The development of the LTPDA toolbox is controlled with the `git` version control, and source code management software. Credit: `http://xkcd.com/1296/`.

B

THE EQUATIONS OF MOTION

In this small section, the equations of motion for the x-y plane are introduced [4]. They are derived theoretically from the dynamics of the system and the recognised cross-coupling mechanisms explained in chapter 5. The different DOF controlled can be seen in figure B.1. At this point we should introduce some of the constants of that are going to be used in the equations to follow:

- $m_1 = m_2 = 1.96$ kg are the masses of the TMs and $m_{SC} = 422.7$ kg that of the SC.
- $I_x = I_y = I_z = 0.0006912$ kg m^2 are momenta of inertia of the TMs with respect to the relative axis.
- $I_{x,SC} = 202.5$ kg m^2, $I_{y,SC} = 209.7$ kg m^2 and $I_{z,SC} = 191.7$ kg m^2 are the momenta of inertia of the SC with respect to the relative axis.
- $\ell = 46$ mm is the size of the TMs.
- r_1 and r_2 are the distances between TM1 and TM2 from the optical bench (in principle, $r_1 = r_2$ ad $r_1 + r_2 = L = 38$ cm, where L is the distance between the two TMs).

All forces and torques in the equations are normalised to the relative mass and momentum of inertia respectively. The parameters and various terms that will appear in the equations are listed as follows, assuming that each generic readout signal o is the sum of the readout signal itself plus the injected signal, $o + o_i$.

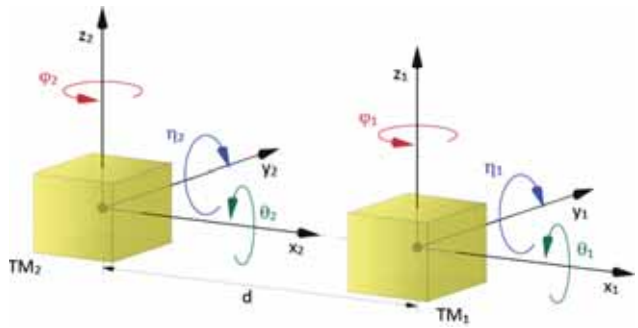

Figure B.1: Schematics of the degrees-of-freedom and their notation for both TMs.

- ω^2_{x1}, ω^2_{x2}, ω^2_{y1}, ω^2_{y2}, $\omega^2_{\phi 1}$, $\omega^2_{\phi 2}$ are the parasitic stiffnesses that couple the different DOF to the SC.
- $\delta_{N_{cmd,\phi 1}}$ and $\delta_{N_{cmd,\phi 2}}$ are the crosstalk coefficients related to the imperfection of the two electrodes. When a rotation by applying a torque is commanded, non-perfectly aligned electrodes will also apply a leakage force along x (see section 5.1).

- δ_{xy1}, δ_{xy2}, $\delta_{x\phi1}$, $\delta_{x\phi2}$ are the so called cross-stiffness terms that link y_1, y_2, ϕ_1, ϕ_2 to $\ddot{o}_{12}$ that originate from the distortion of the electric field lines. Actually, here these dimensionless terms transform the stiffness of the proper DOF into a cross-stiffness term with the x-axis.
- $\delta_{f_{y1,cmd}}$ and $\delta_{f_{y2,cmd}}$ convert the commanded force, respectively, on y_1 and y_2 into a force along x.
- δ_{Hy} and $\delta_{H\Phi}$ convert respectively the commanded force along y and the commanded torque around z on the SC into a force along x.
- $h_{\phi1}$ and $h_{\phi2}$ are the gains of the electrostatic suspension that controls the TMs, respectively, around z_1 and z_2.
- A_{sus} is the gain of the suspension control loop acting on the TM2 along x.
- H_{y1} and H_{y2} are the gain of the drag-free loops along y_1 and y_2.
- H_x is the gain of the drag-free loop along x.
- $h_{\Phi A}$ is the gain of the attitude control loop around z.
- o_{x1}, o_{y1}, o_{ϕ_1}, o_{x2}, o_{y2}, o_{ϕ_2}, o_Δ are the readouts associated to the coordinates of the two TMs and o_Φ the readout associated with the SC rotation around z.
- A_x and A_y are the linear acceleration of the SC along x and y directions.
- $o_{i\phi_1}$, $o_{i\phi_2}$, $o_{i\Phi}$, o_{iy1}, o_{iy2} are the guidance signals that we can inject into the control loop as a bias to the original signal.
- $f_{y1,cmd}$ and $f_{y2,cmd}$ are the forces per unit mass applied respectively on TM1 and TM2 along y_1 and y_2.

The dynamics along x

TM1:

$$\begin{aligned} x_1\left(s^2+\omega_{px1}^2\right) = &-A_x+ \\ &+\left[f_{y1,cmd}+h_{\Phi A}\left(o_{i\Phi}+o_\Phi\right)r_1\right]\delta_{hy1} \\ &-\frac{1}{2}\ell h_{\phi1}\left(o_{i\phi1}+o_{\phi1}\right)\delta_{h\phi1} \\ &+o_{y1}\delta_{xy1}\omega_{py1}^2+\frac{1}{2}\ell o_{\phi1}\delta_{x\phi1}\omega_{p\phi1}^2 \end{aligned} \tag{B.1}$$

TM2:

$$\begin{aligned}(\Delta x + x_1)\left(s^2 + \omega_{px2}^2\right) = &- A_x + \\ &- h_x o_\Delta \\ &+ [f_{y2,cmd} - h_{\Phi A}\left(o_{i\Phi} + o_\Phi\right) r_2]\delta_{hy2} \\ &- \frac{1}{2}\ell h_{\phi 2}\left(o_{i\phi 2} + o_{\phi 2}\right)\delta_{h\phi 2} \\ &+ o_{y2}\delta_{xy2}\omega_{py2}^2 + \frac{1}{2}\ell o_{\phi 2}\delta_{x\phi 2}\omega_{p\phi 2}^2\end{aligned} \tag{B.2}$$

SC:

$$\begin{aligned}A_x = &H_x o_1 + \\ &+ \frac{\left(H_{y2}\left(o_{iy2} + o_{y2}\right) r_1 + H_{y1}\left(o_{iy1} + o_{y1}\right) r_2\right)\delta_{Hy}}{r_1 + r_2} \\ &+ \frac{1}{2}\left(-H_{y1}\left(o_{iy1} + o_{y1}\right) + H_{y2}\left(o_{iy2} + o_{y2}\right)\right)\delta_{H\Phi}\end{aligned} \tag{B.3}$$

The dynamics along y

TM1:

$$y_1\left(s^2 + \omega_{py1}^2\right) = -A_y + s^2\Phi r_1 + h_{\Phi A}\left(o_{i\Phi} + o_\Phi\right) r_1 + f_{y1,cmd} \tag{B.4}$$

TM2:

$$y_2\left(s^2 + \omega_{py2}^2\right) = -A_y - h_{\Phi A}\left(o_{i\Phi} + o_\Phi\right) r_2 - s^2\Phi r_2 + f_{y2,cmd} \tag{B.5}$$

SC:

$$A_y = \frac{\left(H_{y2}\left(o_{iy2} + o_{y2}\right)\right) r_1 + \left(H_{y1}\left(o_{iy1} + o_{y1}\right)\right) r_2}{r_1 + r_2} \tag{B.6}$$

The dynamics around z

TM1:

$$\phi_1 \left(s^2 + \omega_{p\phi 1}^2 \right) = -s^2 \Phi - h_{\phi 1} \left(o_{i\phi 1} + o_{\phi 1} \right) \tag{B.7}$$

TM2:

$$\phi_2 \left(s^2 + \omega_{p\phi 2}^2 \right) = -s^2 \Phi - h_{\phi 2} \left(o_{i\phi 2} + o_{\phi 2} \right) \tag{B.8}$$

SC:

$$s^2 \Phi = -\frac{H_{y1} \left(o_{iy1} + o_{y1} \right) - H_{y2} \left(o_{iy2} + o_{y2} \right)}{r_1 + r_2} \tag{B.9}$$

C

THE REVERSIBLE JUMP MCMC ALGORITHM

The RJMCMC algorithm is a robust and efficient tool to estimate the Bayes Factor. It can be shown [5, 6] that after a large number of iterations it will converge to the true value of the Bayes Factor. The only drawback is the computational cost of the algorithm. When more than three models are being compared, meaning that many transdimensional moves have to be performed, a considerable amount of time is required for convergence. The algorithm implemented in this work is a special case of the *Metropolized Carlin and Chib* method [7, 8].

More specifically, let us suppose that we have a total number K of models to compare given a data set $\vec{y}$. Then, the recipe for our RJMCMC method can be summarised in the following steps [7]:

1. Initialization: Choose an initial model k and the corresponding parameters $\vec{\theta}_k$.
2. Apply the Metropolis algorithm for model k. This step is also called the "in model step".
3. Generate new $\vec{\theta_{k'}}$ from a multivariate Gaussian PDF and a random number $\rho \in [0, 1]$ from a uniform distribution. This is the step where we propose a new model k'.
4. Calculate the acceptance ratio α':

$$\alpha' = \min\left[\frac{\pi(\vec{y}|\vec{\theta}_{k'})p(\vec{\theta}_{k'})g(u_{k'})}{\pi(\vec{y}|\vec{\theta}_k)p(\vec{\theta}_k)g(u_k)}|\mathbf{J}|, 1\right], \tag{C.1}$$

   where $g(u)$ is the proposal distribution from where the "dimension matching" parameters u are drawn [9], and $|\mathbf{J}|$ is the Jacobian:

$$|\mathbf{J}| = \left|\frac{\partial(\vec{\theta}_{k'}, u_{k'})}{\partial(\vec{\theta}_k, u_k)}\right|. \tag{C.2}$$

5. If $\rho < \alpha'$ we accept the new model k' with parameters $\vec{\theta_{k'}}$ and set $\vec{\theta_k} = \vec{\theta_{k'}}$.
6. Iterate from step 2 until convergence is achieved.

The old set of parameters is connected to the new one by a well defined function $\vec{\theta_k} = q(\vec{\theta_{k'}}, u)$ (and of course $\vec{\theta_{k'}} = q'(\vec{\theta_k}, u')$). We use *independent* proposals, so $\vec{\theta_k} = q(\vec{\theta_{k'}}, u) = u$ and $\vec{\theta_{k'}} = q'(\vec{\theta_k}, u') = u'$, thus, the Jacobian term in equation (C.1) is unity. The algorithm spends most of the time iterating "inside" the model that best describes the data. The RJMCMC method auto-penalizes high dimension models, also by taking into account the priors $p(\vec{\theta}_k)$ of each model k. They serve as an Occam Factor integrated within the algorithm.

Convergence is achieved if two main conditions are satisfied. First, the condition of *reversibility*, which is stated in a simple way: The proposal function must be invertible, meaning that we can jump from the proposed parameters back to the current parameters. And second, we must satisfy the *dimension matching* condition which in our case is always true since we use independent proposals in the acceptance ratio. After convergence has been achieved, a good approximation to the Bayes Factor is given by [10, 11, 6, 12]

$$B_{XY} = \frac{\#\text{ of iterations in model X}}{\#\text{ of iterations in model Y}}. \tag{C.3}$$

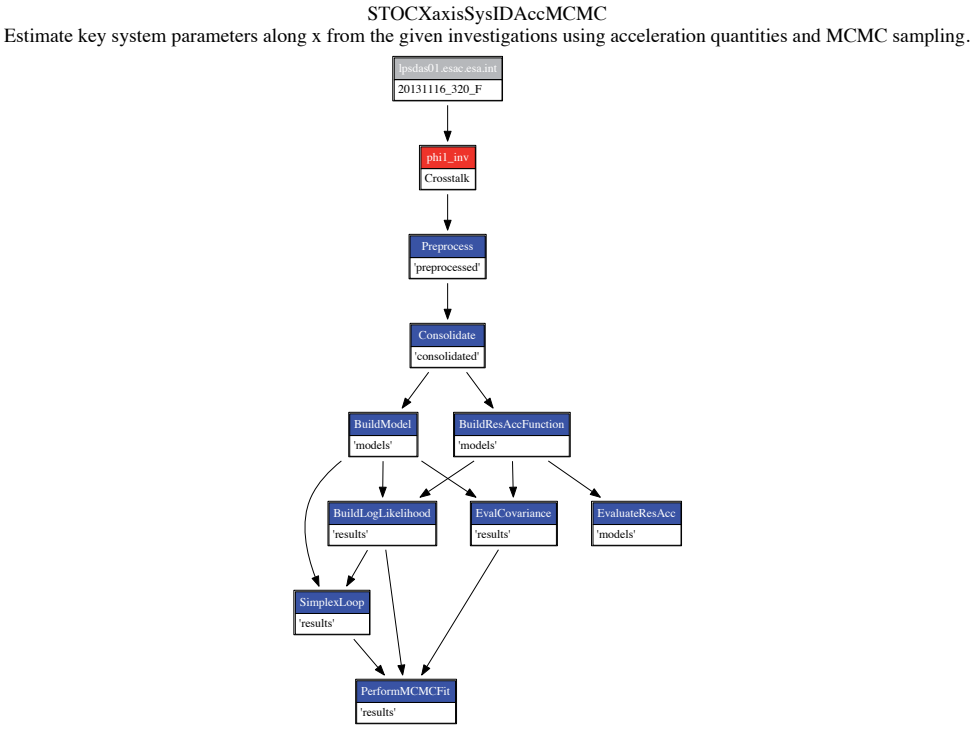

Figure D.1: The Bayesian parameter estimation pipeline flow diagram. This figure is automatically produced in Matlab, with the command `pipeline_obj.flowDiagram`.

A pipeline analysis, must include a series of analysis steps to be sequentially performed during operation of the LPF experiment [13, 14]. These steps refer to data retrieving up to submitting the results to dedicated repositories. In reality, the pipelines designed are generalised scripts that can be applied in most in-flight situations. The particular one showed in figure D.1 is organised as follows:

- Pipeline definition: The first action is the definition of the pipeline, by calling its constructor with the appropriate inputs. The inputs fields are the name, type, time-span of the analysis, and repository information. It captures all the details of the investigation being analysed and can handle multiple experiments. This is the red box of figure D.1, while the first grey one refers to the data repository.

- `Preprocess`: After the definition of the pipeline, the data are downloaded and stored to the disk locally. The pre-process step then resamples and splits the data in the desired sampling frequency and time-span of the analysis.

- `Consolidate`: Resamples all input AOs onto the same time grid and truncates all time-series to start at the maximum start time of the inputs and end at the minimum stop time of the inputs.
- `BuildResAccFunction`: It automatically loads the pre-processed times-series and constructs two models in the acceleration domain and stores then into disk. The pre-defined models are a set of α_1 and the differential acceleration α_{12}, from equations 4.12. This step was developed for the x-axis system identification analysis.
- `BuildModel`: With the same working principle as the `BuildResAccFunction`, it constructs a model given the equation provided by the user. This step basically covers the needs for any given investigation that requires fitting.
- `EvaluateResAcc`: Here the model is evaluated at a given set of parameters.
- `BuildLogLikelihood`: The log-likelihood function is build according the the definitions provided by the user. All the available techniques discussed in this thesis (see section 4.4), are available here. The unction is then saved into disk locally.
- `EvalCovariance`: The expected covariance matrix of the parameters is estimated via the inversion of the FIM (see section 3.3). The resulting matrix is then used for the proposal distribution[1] of the MH algorithm.
- `SimplexLoop`: The iterative χ^2 scheme described in section 4.3.2 is performed here by sequential minimisations of the log-likelihood with the algorithm described in [3].
- `PerformMCMCFit`: The sampling of the posterior distribution is performed. The final analysis results are stored locally and also submitted to dedicated repositories defined at the beginning of this pipeline analysis.

1 We recall that the proposal used here is a multivariate normal distribution with $\Sigma = \mathsf{F}^{-1}$, with F being the Fisher matrix. It is all possible to set another porpoal distribution that may be more suitable for the given problem.

[1] S Vitale. Measurement of LTP dynamical coefficients by system identification. Technical Report S2-UTN-TN-3045, 2007. 157

[2] N. Karnesis, Nofrarias M., and M. Hewitson. MCMC Parameter Estimation for LPF: Design & Code Review. Technical report. 157, 158

[3] Jeffrey C. Lagarias, James A. Reeds, Margaret H. Wright, and Paul E. Wright. Convergence properties of the nelder-mead simplex method in low dimensions. *SIAM Journal of Optimization*, 9:112–147, 1998. 157, 168

[4] S. Vitale. Measurement of cross-talk between the y-axis and the x-axis on the LTP. Technical report. 161

[5] P J Green. Reversible jump Markov chain Monte Carlo computation and Bayesian model determination. *Biometrica*, (82):711–32, 1995. 165

[6] P Dellaportas, J J Forster, and I Ntzoufras. On Bayesian model and variable selection using MCMC. *Statistics and Computing*, pages 27–36, 2002. 165, 166

[7] Nikolaos Karnesis, Miquel Nofrarias, Carlos F. Sopuerta, et al. Bayesian model selection for lisa pathfinder. *Phys. Rev. D*, 89:062001, Mar 2014. URL: http://link.aps.org/doi/10.1103/PhysRevD.89.062001, doi:10.1103/PhysRevD.89.062001. 165

[8] Hedibert Freitas Lopes and Mike West. Bayesian model assessment in factor analysis. *Statistica Sinica*, 14:41–67, 2004. 165

[9] Simon J. Godsill. On the relationship between markov chain monte carlo methods for model uncertainty. *JOURNAL OF COMPUTATIONAL AND GRAPHICAL STATISTICS*, 10:230–248, 2001. 165

[10] Tyson B. Littenberg and Neil J. Cornish. Bayesian approach to the detection problem in gravitational wave astronomy. *Phys. Rev. D*, 80:063007, Sep 2009. URL: http://link.aps.org/doi/10.1103/PhysRevD.80.063007, doi:10.1103/PhysRevD.80.063007. 166

[11] Francesco Bartolucci, Luisa Scaccia, and Antonietta Mira. Efficient bayes factor estimation from the reversible jump output. *Biometrika*, 93(1):41–52, 2006. doi:10.1093/biomet/93.1.41. 166

[12] N Cornish and T Littenberg. Tests of Bayesian model selection techniques for gravitational wave astronomy. *Physical Review D*, 76(8):1–11, October 2007. URL: http://link.aps.org/doi/10.1103/PhysRevD.76.083006, doi:10.1103/PhysRevD.76.083006. 166

[13] M. Hewitson. Data Analysis Handbook for the 2nd STOC Simulation. Technical report. 167

[14] M. Hewitson. The LTPDA Pipeline Handbook. Technical report. 167

COLOPHON

This document was typeset using the typographical look-and-feel `classicthesis` developed by André Miede.

http://code.google.com/p/classicthesis/

Final Version as of October 30, 2014 (`classicthesis` version 1.0).